73-9171

ROLAND, Jay Roy, 1937-
TIME ASYMPTOTIC DETERMINATION OF THE EFFECTS OF ABLATION-PRODUCT ABSORPTION-COEFFICIENT ENHANCEMENT ON THE MASS LOSS RATE FROM THE STAGNATION POINT OF A BLUNT BODY IN THE MASSIVE BLOWING REGIME.

The University of Oklahoma, Ph.D., 1972
Engineering, aeronautical

University Microfilms, A XEROX Company, Ann Arbor, Michigan

THE UNIVERSITY OF OKLAHOMA

GRADUATE COLLEGE

TIME ASYMPTOTIC DETERMINATION OF THE EFFECTS OF ABLATION-PRODUCT ABSORPTION-COEFFICIENT ENHANCEMENT ON THE MASS LOSS RATE FROM THE STAGNATION POINT OF A BLUNT BODY IN THE MASSIVE BLOWING REGIME

A DISSERTATION

SUBMITTED TO THE GRADUATE FACULTY

in partial fulfillment of the requirements for the

degree of

DOCTOR OF PHILOSOPHY

BY

JAY ROY ROLAND

Norman, Oklahoma

1972

TIME ASYMPTOTIC DETERMINATION OF THE EFFECTS OF ABLATION-PRODUCT ABSORPTION-COEFFICIENT ENHANCEMENT ON THE MASS LOSS RATE FROM THE STAGNATION POINT OF A BLUNT BODY IN THE MASSIVE BLOWING REGIME

APPROVED BY:

Martin C. Jischke

Raymond Kaser

Edward A. Blick

M. Rasmussen

[illegible]

DISSERTATION COMMITTEE

ACKNOWLEDGMENTS

This work was initiated because of a question posed by Dr. Martin Jischke who has served as my major professor and without whose encouragement and patience during two years of work in absentia this effort could not have been completed. At the time of initiation I was on an Air Force assignment through the Air Force Institute of Technology Civilian Institutions program at the University of Oklahoma.

After a reassignment to the Air Force Weapons Laboratory, my supervisor, LtCol Carl Hilland, was very accommodating and allowed me to pursue on a part time basis my independent research. The discussions from time to time with Maj William Whitaker were invaluable and I owe a debt of appreciation to Capt Charles Walters for his help with mathematical algorithms and Capt Gregory Canavan for discussions of time dependent techniques. Capt Frank Cassisa was extremely helpful in code modifications and production runs and Tommy Perea's work on the calculations for Appendix E was excellent. My secretary Esther Caster has done an outstanding job of typing and editing my drafts into a finished manuscript and Frank White deserves commendation for his timely and accurate work with the figures. I would like to apologize to my wife Bettye and our children Jayme, Lisa, Ludie and Randy for the many evenings and weekends they sacrificed in order for me to pursue this research.

Because of their continual encouragement and everlasting inspiration this work is dedicated to my beloved parents, Ludie and Artie Roland.

ABSTRACT

For a blunt body undergoing massive ablation, the stagnation region is treated as two inviscid regions separated by a slip-layer. The momentum equation for each region is solved in quadrature form and then for purposes of calculating the stream function the density of each layer is assumed constant. This leads to an analytical solution of the momentum equation and yields the entire stagnation-point geometry. The energy equation is then developed including nongrey absorption and emission of radiation in both the shock and ablation layers. An energy balance at the body surface gives the ablation mass loss rate through an effective heat of ablation and thus provides the coupling between the momentum and energy equations.

The effects of increasing the ablation layer absorption coefficient are then examined for both a grey and a two-energy group absorption coefficient model. The energy equation is solved by a time asymptotic technique which remains stable with large discontinuities in fluid properties. This allows investigation of ablation layer absorption coefficient enhancement by factors greater than 10^7. The result is an ablation layer that becomes optically thick owing to a programmed increase in absorption coefficient rather than through an a priori Rosseland approximation. In all cases of absorption coefficient enhancement (grey, vacuum ultraviolet and visible, and vacuum ultraviolet) a point is reached beyond which increases in enhancement cause an increase in the mass loss rate rather than the generally observed decrease.

TABLE OF CONTENTS

LIST OF TABLES

LIST OF FIGURES

LIST OF FIGURES (continued)

LIST OF FIGURES (continued)

LIST OF FIGURES (continued)

LIST OF FIGURES (continued)

NOMENCLATURE

The following nomenclature is used throughout this work.

a	coefficient of exponential integral approximation, see Eq. E.5
A	geometry factor (1+Ky)
$A^j(z)$	dummy parameter, see Appendix C
b	coefficient of exponential integral approximation, see Eq. E.5
$B^j(z)$	dummy parameter, see Appendix C
B_ν	Planck function
c	speed of light
C(x)	dummy variable
Di	diffusive enhancement factor
$E_n(x)$	exponential integral defined by Eq. 3.15
$f(\zeta)$	density function [$2\varepsilon(1-\varepsilon)\rho_s/\rho$ - shock layer, ρ/ρ_w - ablation layer]
F	stream function, see Eqs. A.8 and A.14
G	dummy variable in momentum integrals
h	specific enthalpy of the gas
H	dummy variable in momentum integrals
H(x)	Heaviside function defined in Chapter II
H^*_{eff}	effective heat of ablation without wall enthalpy (See Eq. 3.23)
H_{eff}	effective heat of ablation with wall enthalpy (See Eq. 3.23)
I_j	partial integral of the Planck function between ν_{j-1} and ν_j
I_ν	specific intensity at frequency ν
JS	number of steps in an absorption coefficient model

NOMENCLATURE (continued)

k	thermal conductivity
K	body curvature factor, approximately $1/R_N$ at stagnation point
M	total number of mesh points
N_{Bo}	Boltzmann number
N_{Bu}	Bouguer number
N_{CR}	conduction-radiation number
N_{Pe}	Péclet number
P	static pressure
q_b	aerodynamic blockage heat flux
q_{cond}	conductive heat flux
q_ν	heat flux at frequency ν
q^r	radiative heat flux
q^{rr}	reradiative heat flux from wall or body
Re	Reynolds number
t	time in Chapter III, artificial independent variable in Chapter IV
T	temperature
Th	absorption coefficient enhancement factor
$T_{\nu,br}$	brightness temperature, see Eq. 5.11
u	general velocity or velocity along x-physical coordinate
v	velocity component normal to body
V_w	velocity of wall injectant
x	general coordinate or physical coordinate along body originating at stagnation point
X_1^j, X_2^j, X_3^j	auxiliary variables defined by Eqs. C.12, C.13, and C.14
y	physical coordinate originating at body

NOMENCLATURE (continued)

z	physical coordinate originating from shock
α	volumetric absorption coefficient
$\alpha_{a,j}$	ablation layer absorption coefficient for jth step
$\alpha_{s,j}$	shock layer absorption coefficient for jth step
Γ	radiation cooling number
γ	unified boundary condition on stream function derivative (1 - shock, 0 - body)
Δ	shock stand off distance from body in physical coordinate system
Δ_a	interface stand off distance from wall in physical coordiante system
Δ_s	shock stand off distance from interface in physical coordinate system
δ	shock stand off distance from body in stream function coordinate system
δ_a	interface stand off distance from body in stream function coordinate system
δ_s	shock stand off distance from interface in stream function coordinate system
ε	density ratio across shock or surface emissivity
$\varepsilon_{\nu,w}(\mu)$	wall or body spectral and directionally dependent emissivity
ζ	generalized stream function coordinate normal to body
η	stream function coordinate originating at body
θ	parameter that determines type of difference scheme, see Eq. 4.2
$\theta(\ )$	order of ( )
λ	factor $[(1-f)^{-\frac{1}{2}}]$ or wave length
μ	cosine of polar angle or dynamic viscosity
ν	frequency or kinematic viscosity

NOMENCLATURE (continued)

ξ	stream function coordinate originating at shock
ρ	density of gas
σ	geometry factor in Chapter II and Appendix A (1 - planar, ½ - three-dimensional), Sephan Boltzmann constant in Chapter III
τ_Δ	optical depth at body
τ_ν	optical depth at frequency ν defined by Eq. 3.2
$\bar{\tau}$	defined by Eq. 5.14
ϕ	azimuthal angle
$( )_a$	ablation layer
$( )_g$	gas
$( )_i$	interface condition or space discretized variable
$( )^n$	time discretized variable
$( )_o$	reference conditions (sea level standards)
$( )_s$	shock condition
$( )_w$	wall or body condition
$( )_{we}$	wall emission
$( )_{wr}$	wall reflection
$( )_\infty$	free stream conditions
$( )^+$	variable directed in positive coordinate direction
$( )^-$	variable directed in negative coordiante direction
$( )'$	differentiation with respect to independent variable or dummy variable in integration
$\tilde{( )}$	normalized function, see Eq. 3.31
$\rightarrow$	approaches in the limit

TIME ASYMPTOTIC DETERMINATION OF THE EFFECTS OF ABLATION-PRODUCT ABSORPTION COEFFICIENT ENHANCEMENT ON THE MASS LOSS RATE FROM THE STAGNATION POINT OF A BLUNT BODY IN THE MASSIVE BLOWING REGIME

CHAPTER I

INTRODUCTION

Stagnation-point heating to bodies traveling in the earth's atmosphere has been studied extensively for many years. More recently interest in very high speed motion has led to the consideration of very large heating rates and the resulting problem of material decomposition or ablation. The work of Howe and Viegas (1963) indicated that the injection of foreign species into the boundary layer and the resulting absorption of radiation by the injectant would substantially reduce the wall radiative heat flux. After this early work many investigators considered the effects of injected or ablation species on the net surface heat flux, although a complete treatment of the problem has not yet been given. Wilson (1970) accurately characterized the ablation and air species absorption coefficients, but specified, rather than computed from a wall energy balance, the injection rate. Chin (1968) used a surface energy balance but considered only the line transitions of nitrogen atoms in the ablation layer rather than the transitions of nitrogen atoms in the ablation layer rather than the transitions of atoms present in an ablation gas. Bartlett et al. (1969) treated the wall energy balance correctly but superimposed the radiation with a cooling factor.

In the current analysis, the wall energy balance is characterized by a fixed temperature and an effective heat of ablation and the radiation transport is treated with either a grey-gas model or a two-step continuum model. The stagnation region is characterized by a two inviscid layer flow field separated by a slip layer. Although no mass is transported across the slip layer, energy is transported by both radiation and conduction. The incorporation of conduction in the inviscid flow field calculation was necessary to allow equilibration of energy across the discontinuity in optical properties at the slip layer. This discontinuity is a result of the ablation layer absorption coefficient enhancement through a multiplicative factor attached to the ablation layer absorption coefficient. Because this model yields a step function in the absorption coefficient, a discontinuity in the temperature profile would result without thermal diffusion. Additional justification comes from the results which show that owing to the very steep gradient in the temperature profile at the slip layer, conduction can become the dominant mode of heat transfer, and the energy field in some cases is in conductive-radiative equilibrium on the shock side and in conductive-convective equilibrium on the ablation side of the slip layer.

The results of this study demonstrate that time asymptotic techniques can be successfully used on radiative-coupled flow fields which include large discontinuities in fluid properties. Because stability can be maintained through those large discontinuities, it is possible to drive the ablation layer from optically thin to optically thick and investigate the physical phenomena associated with this transition. It was demonstrated that enhanced ablation-layer absorption coefficients will cause a reduction in wall mass loss rate only to a point. Enhancement beyond that point causes the wall mass loss rate to increase with increased enhancement. With a fixed wall mass loss rate a minimum in the wall heat flux was not observed with enhancement through the limit of the current theory. This result should be a caution to investigators who attempt to draw conclusions about ablator performance based on fixed wall mass flux analyses.

CHAPTER II

SOLUTION OF THE MOMENTUM EQUATION

Consider the momentum equation as derived in Appendix A in the form

$$F\,F'' = \sigma[F'^2 - f(\zeta)], \qquad 2.1$$

where σ is 1 for two-dimensional and 1/2 for three-dimensional flow while $f(\zeta)$ is $2\varepsilon(1-\varepsilon)\rho_s/\rho$ for the shock layer and ρ_w/ρ for the ablation layer. The boundary conditions for the shock-layer solution are (see Figs. A.1 and A.2 for geometry and nomenclature):

at $\zeta = 0$ (shock wave)

$$F = -F' = 1$$

at $\zeta = \zeta_i$ (interface)

$$F = 0 \; .$$

For the ablation layer the boundary conditions are:

at $\zeta = 0$ (body)

$$F = 1, \quad F' = 0$$

at $\zeta = \zeta_i$ (interface)

$$F = 0 \ .$$

For the desired general solution, we can pose the following unified boundary conditions:

at $\zeta = 0$

$$F = 1 \ , \quad F' = -\gamma$$

at $\zeta = \zeta_i$

$$F = 0$$

where γ is 1 for the shock layer and 0 for the ablation layer. Although Eq. 2.1 is a second-order ordinary differential equation, the third boundary condition is required in order to determine the location of the interface, symbolized in both coordinate systems by ζ_i.

An analytical solution of Eq. 2.1 can be obtained if we multiply it by F', yielding

$$F\ F'\ F'' = \sigma F'[F'^2 - f(\zeta)]$$

or

$$\frac{1}{2} F \frac{d}{d\zeta}\left(F'^2\right) = \sigma F'[F'^2 - f(\zeta)] \ . \qquad 2.2$$

If we now multiply Eq. 2.2 through by 2/F'F and rearrange, the result is

$$\frac{dF'^2}{dF} - \frac{2\sigma}{F} F'^2 = -\frac{2\sigma}{F} f(\zeta) \ . \qquad 2.3$$

Multiplying Eq. 2.3 by the integrating factor $(F)^{-2\sigma}$ we obtain

$$\frac{d(F'^2/F^{2\sigma})}{dF} = -\frac{2\sigma}{F^{1+2\sigma}} f(\zeta) \qquad 2.4$$

which can be integrated to yield

$$(F')^2 F^{-2\sigma} - \gamma^2 = -2\sigma \int_1^F \frac{f(\zeta)}{H^{1+2\sigma}} dH \ . \qquad 2.5$$

We can now solve Eq. 2.5 for F',

$$F' = -\left(\gamma^2 F^{2\sigma} - 2\sigma F^{2\sigma} \int_1^F \frac{f(\zeta)}{H^{1+2\sigma}} dH\right)^{\frac{1}{2}} . \qquad 2.6$$

The negative square root in Eq. 2.6 was selected by considering the boundary conditions which show that F(0) is 1 while $F(\zeta_1)$ is zero, and since the radical of Eq. 2.6 must always be positive, F must be monatonic and the boundary conditions require it to be monatonically decreasing.

We can now invert Eq. 2.6 to get

$$d\zeta = -\frac{dF}{\left(\gamma^2 F^{2\sigma} - 2\sigma F^{2\sigma}\int_1^F \frac{f(\zeta)}{H^{1+2\sigma}}\, dH\right)^{\frac{1}{2}}}$$

which integrates to

$$\tau = -\int_1^F \frac{dG}{G^{\sigma}\left(\gamma^2 - 2\sigma\int_1^G \frac{f(\zeta)}{H^{1+2\sigma}}\, dH\right)^{\frac{1}{2}}} \; . \qquad 2.7$$

Equation 2.7 is the general solution in quadrature form for the unified stream function. The solution can be carried no farther analytically without prescribing $f(\zeta)$. Because we desire, in order to simplify future computations, to analytically solve the momentum equation we will at this point assume $f(\zeta)$ to be constant.

This assumption implies that for purposes of calculating the stream function, we are considering constant density solutions (the density in the shock layer is that calculated by the Rankine-Hugoniot relations across the shock while the density in the ablation layer is that of the ablation products at the wall). For free stream conditions similar to those of the current analysis, Howe and Viegas (1963) determined through a fully-viscous grey radiation-coupled stagnation region solution that the density in the shock layer was constant except for a very small region near the body. Olstad's analysis (Olstad, 1969) of a nongrey radiation-cooled (including the contribution of atomic lines) flow about a symmetric body shows that near the stagnation point the shock layer density is again relatively constant (the change across the shock layer is less than 10%) except for the small region near the body. For the purposes of evaluating $\zeta(F)$ from Eq. 2.7, the small regions where the density varies makes a negligible contribution to the quadrature. Jischke and Baron (1969) by including the effects of coupling the momentum and energy equations have shown the effect of radiative transfer on the stream function to be quite small for a wide range of parameter values provided the shock layer thickness is normalized to unity. It should be emphasized that the constant density assumption is only made for purposes of calculating the stream function and the justification rests on the fact that the momentum equation is only weakly coupled to the energy equation (Hoshizaki and Lasher, 1968).

This uncoupling of the momentum equation from the energy equation does not simplify the problem into what Anderson (1968b) calls "uncoupled shock layer". The latter refers to the condition of neglecting the influence of radiative energy transport on the shock layer variables, i.e., the divergence of the radiative flux is omitted from the energy equation. The radiative flux to a body due to the resulting temperature profile is then calculated a posteriori. These "uncoupled shock layer" calculations neglect radiative cooling and (for the same absorption coefficient data) can yield up to twice the radiative heat transfer of a coupled solution, i.e., one which includes radiative cooling of the shocked gas. The current analysis includes radiative cooling, self absorption, and conduction for both the shock and ablation layers.

With $f(\zeta)$ constant, the integral in the radical of Eq. 2.7 can be evaluated as

$$2\sigma f\int_1^G \frac{dH}{H^{1+2\sigma}} = f(1 - G^{-2\sigma}), \tag{2.8}$$

where we have taken advantage of σ being either 1 or 1/2. Equation 2.7 can now be expressed as

$$\zeta = \frac{1}{f^{\frac{1}{2}}}\int_F^1 \frac{dG}{\left(\frac{\gamma^2-f}{f}\,G^{2\sigma}+1\right)^{\frac{1}{2}}} \quad . \tag{2.9}$$

Equation 2.9 is the general two or three-dimensional, shock or ablation layer solution for the stream function in quadrature form with the assumption that $f(\zeta)$ is constant. If we consider the four cases one at a time additional analytical results can be obtained. Comparison with previously published results will then be made to indicate the accuracy of the current development.

Let us first consider the two-dimensional case ($\sigma = 1$). For this case Eq. 2.9 becomes

$$\zeta = \frac{1}{f^{\frac{1}{2}}}\int_F^1 \frac{dG}{\left(\frac{\gamma^2-f}{f}\,G^2 + 1\right)^{\frac{1}{2}}} \quad . \tag{2.10}$$

We cannot carry out the integration in Eq. 2.10 without specifying the sign of the G^2 coefficient. For the shock layer with f constant

$$\frac{\gamma^2-f}{f} = \frac{1-2\varepsilon(1-\varepsilon)}{2\varepsilon(1-\varepsilon)} = \frac{(1-\varepsilon)^2+\varepsilon^2}{2\varepsilon(1-\varepsilon)} \qquad 2.11$$

which is positive since $0 \leq \varepsilon \leq 1$. Equation 2.10 can then be integrated for the shock layer to give

$$\zeta = (1-f)^{-\frac{1}{2}}\ell n\left[\frac{\left(\frac{1-f}{f}\right)^{\frac{1}{2}} + \left(\frac{1}{f}\right)^{\frac{1}{2}}}{F\left(\frac{1-f}{f}\right)^{\frac{1}{2}} + \left(\frac{1-f}{f}F^2 + 1\right)^{\frac{1}{2}}}\right] \qquad 2.12$$

which is the solution for the stream function for the two-dimensional shock layer. At the interface, the normal velocity, thus F, must go to zero. This condition imposed in Eq. 2.12 yields the shock stand-off distance as

$$\zeta_s = \zeta(F=0) = (1-f)^{-\frac{1}{2}}\ell n\left[\left(\frac{1-f}{f}\right)^{\frac{1}{2}} + \left(\frac{1}{f}\right)^{\frac{1}{2}}\right]. \qquad 2.13$$

For small ε corresponding to strong shock waves $f \to 2\varepsilon$ and Eq. 2.13 becomes

$$\lim_{\varepsilon\to 0} \zeta_s = \frac{1}{2}\,\ell n\left(\frac{4}{2\varepsilon}\right). \qquad 2.14$$

The transformation from the normalized to the physical coordinate system is, for $f(\zeta)$ constant,

$$z = \varepsilon R_N \zeta \ .$$

Therefore the shock stand-off distance from the interface with small ε is

$$\Delta_s = \frac{1}{2}\, \varepsilon R_N \ell n\left(\frac{4}{2\varepsilon}\right) \tag{2.15}$$

which agrees to lowest order with the constant density solution of Hayes and Probstein (1959, p 152). The constant density solution is only valid for ε very small and then only in a local region in the vicinity of the stagnation stream line. For the nominal flight conditions under considerations (altitude of 200,000 feet and velocity of 50,000 fps), the shock stand-off distance predicted by Eq. 2.15 is within 7% of that predicted by Hayes and Probstein (1959), p 152). In a simplified analysis first given by Hayes (1955) in which the centrifugal correction to the Newtonian pressure distribution is neglected, the shock stand-off distance obtained agrees with Eq. 2.15 to order $\left(\varepsilon \ell n \frac{1}{\varepsilon}\right)$. Although Eq. 2.15 is in error, the order of the error is small enough that it should not appreciably distort trend-type heat-transfer calculations. We can now invert Eq. 2.12 to obtain the momentum function. The result is

$$F(\zeta) = \frac{1}{2(1+\lambda)}\left[(1+\lambda)^2 e^{-\zeta/\lambda} - f\lambda^2 e^{\zeta/\lambda}\right] \tag{2.16}$$

where

$$\lambda = (1-f)^{-\frac{1}{2}}.$$

Let us return now to Eq. 2.10 and consider the two-dimensional ablation layer in which

$$f(\zeta) = \rho_w/\rho .$$

The assumption that $f(\zeta)$ is constant then yields $f = 1$. If we also impose the ablation layer condition that γ is 0, Eq. 2.10 becomes

$$\zeta = \int_F^1 \frac{dG}{(1-G^2)^{\frac{1}{2}}}$$

which after integration yields

$$\zeta = \frac{\pi}{2} - \text{Sin}^{-1}\,(F) . \qquad 2.17$$

We can now determine the thickness of the ablation layer by evaluating Eq. 2.17 at $F = 0$ which gives

$$\delta_a = (F=0) = \frac{\pi}{2} . \qquad 2.18$$

For the current assumptions, the transformation from the normalized to the physical coordinate is

$$y = R_N\left(\frac{\rho_w V_w^2}{2\rho_\infty U_\infty^2}\right).$$

Therefore the ablation layer thickness is

$$\Delta_a = R_N\left(\frac{\rho_w V_w^2}{2\rho_\infty U_\infty^2}\right)^{\frac{1}{2}} \frac{\pi}{2}. \qquad 2.19$$

Equation 2.19 agrees with the result of Wallace and Kemp (1969) if we take their unspecified reference length as $R_N/\sqrt{2}$. Inverting Eq. 2.17, we have the two-dimensional ablation layer momentum function as

$$F = \mathrm{Cos}\ (\zeta)$$

or in dimensional form

$$V = V_w \mathrm{Cos}\left(\frac{\pi}{2}\frac{y}{\Delta_a}\right). \qquad 2.20$$

Equation 2.20 also agrees with the results of Wallace and Kemp.

The two-dimensional shock and ablation layer analyses have been included for completeness and do tend to add credence to the selected mathematical model, but the remainder of the development will be directed toward the three-dimensional stagnation point. Returning to Eq. 2.9 with σ as $\frac{1}{2}$, we have

$$\zeta = \frac{1}{f^{\frac{1}{2}}}\int_F^1 \frac{dG}{\left(\frac{\gamma^2-f}{f}G + 1\right)^{\frac{1}{2}}}.$$

Upon integration this expression becomes

$$\zeta = \frac{2f}{\gamma^2-f}\left[\left(\frac{\gamma^2}{f}\right)^{\frac{1}{2}} - \left(\frac{\gamma^2-f}{f} F + 1\right)^{\frac{1}{2}}\right] . \qquad 2.21$$

Before inverting Eq. 2.21 for the momentum function, we can consider the shock stand-off distance and the ablation layer thickness by letting F go to zero. This yields

$$\delta = \zeta(F=0) = \frac{2}{\gamma^2-f}\left[\left(\gamma^2\right)^{\frac{1}{2}} - f^{\frac{1}{2}}\right] . \qquad 2.22$$

If we now consider the shock layer and transform to the physical coordinate system, the shock stand-off distance is

$$\Delta_s = \frac{\varepsilon R_N}{1-2\varepsilon(1-\varepsilon)}\{1 - [2\varepsilon(1-\varepsilon)]^{\frac{1}{2}}\} = \frac{\varepsilon R_N}{1+[2\varepsilon(1-\varepsilon)]^{\frac{1}{2}}} \qquad 2.23$$

where the three-dimensional coordinate transformation is

$$z = \frac{\varepsilon}{2} R_N \zeta .$$

Hayes and Probstein (1959, p 159) obtain an implicit solution for the three-dimensional shock stand-off distance under the constant density assumption and only in the limit of small ε do they determine Δ_s explicitly. Their result is

$$\Delta_s = \varepsilon R_s\left[1 - \left(\frac{8\varepsilon}{3}\right)^{\frac{1}{2}}\right] + \theta(\varepsilon^2) . \qquad 2.24$$

Equation 2.23 becomes, for small ε

$$\Delta_s = \varepsilon R_s\left[1 - \left(\frac{8\varepsilon}{4}\right)^{\frac{1}{2}}\right] + \theta(\varepsilon^2) \ . \qquad 2.25$$

The agreement between Eqs. 2.24 and 2.25 is sufficiently good to give a sound basis to the heat transfer calculations which follow.

If we now return to Eq. 2.22 and make the appropriate substitutions, the ablation layer thickness is found to be

$$\Delta_a = R_N\left(\frac{\rho_w V_w^2}{2\rho_\infty U_\infty^2}\right)^{\frac{1}{2}} , \qquad 2.26$$

where the coordinate transformation

$$y = \frac{R_N}{2}\left(\frac{\rho_w V_w^2}{2\rho_\infty U_\infty^2}\right)^{\frac{1}{2}}\zeta$$

has been applied. Although there are no existing three-dimensional constant density solutions with which to compare Eq. 2.26, the dependence on the ablation products velocity at the wall is similar to the two-dimensional result and the two expressions, Eq. 2.19 and Eq. 2.26, differ only by a constant factor.

We can invert Eq. 2.21 to obtain the momentum function as a function of ζ. There results

$$F(\zeta) = 1 - \zeta + \frac{\gamma^2 - f}{4}\zeta^2. \qquad 2.27$$

This gives the momentum function for the shock layer in the physical coordinate frame as

$$F(z) = 1 - 2\,\frac{z}{\varepsilon R_N} + [1 - 2\varepsilon(1-\varepsilon)]\,\frac{z^2}{\varepsilon^2 R_N^2}\,, \qquad 2.28$$

and that for the ablation layer as

$$F(y) = 1 - \frac{2\rho_\infty U_\infty^2}{\rho_w V_w^2}\,\frac{y^2}{R_N^2}\;. \qquad 2.29$$

For future computations it is desirable to select one coordinate system. We will use the current z-coordinate system which orginates at the shock and increases toward the body. In order to unify the momentum profile, we can refer to the momentum function definitions which are

$$F(z) = \frac{\rho v}{\rho_\infty U_\infty}$$

and

$$F(y) = \frac{\rho v}{\rho_w V_w}$$

and impose the coordinate transformation

$$y = \Delta - z,$$

where

$$\Delta = \Delta_s + \Delta_a \;.$$

The resulting momentum profile is

$$\rho v(z) = \rho_\infty U_\infty \left\{1 - 2\frac{z}{\varepsilon R_N} + [1-2\varepsilon(1-\varepsilon)]\frac{z^2}{\varepsilon^2 R_N^2}\right\} H(\Delta_s - z) + \rho_w V_w \left\{\frac{2\rho_\infty U_\infty^2}{\rho_w V_w^2}\left(\frac{\Delta - z}{R_N}\right)^2 - 1\right\} H(z - \Delta_s), \tag{2.30}$$

where the appropriate sign change has been made in Eq. 2.29 to account for the ablation layer velocity being in the negative z direction and H(x) is the Heaviside function defined such that

$$H(x) = \begin{matrix} 1, & x > 0 \\ 1, & x = 0 \\ 0, & x < 0 \end{matrix} \;.$$

The symbol V_w is always treated as being positive.

With the assumption that $f(\zeta)$ is constant (for purposes of calculating the stream function), Eqs. 2.23, 2.26, and 2.30 completely define the three-dimensional stagnation point geometry and momentum field. The remainder of the derivation involves the solution of the energy equation for the temperature profile, heat flux to the wall, and the resulting mass loss from the wall. We can see at this point that we must initially assume V_w (ablation velocity at the wall) in order to determine Δ_a from Eq. 2.26 and the momentum profile in the ablation layer from Eq. 2.30. After proceeding through the solution of the energy equation, the computed V_w will be compared with the assumed value and iterations will proceed until the desired convergence is obtained. It is through this up-dating of V_w and thus the ablation layer geometry and momentum field by Eq. 2.26 that the energy-momentum coupling actually takes place.

Before proceeding to the energy equation formulation, it should be pointed out that by developing the momentum profile in the manner of this section rather than by the Hayes and Probstein or Wallace and Kemp constant density techniques, we have allowed for simple extension to a completely general, variable density solution. This could be accomplished by using the current solution as the first iteration. Then with the corrected V_w and a predicted $f(\zeta)$ based on the density being some known function of temperature, Eq. 2.1 is integrated directly yielding a corrected momentum profile. Iterations continue until the desired results are obtained. This suggested procedure without guidance on the initial guess is similar to that proposed by Chin (1968).

CHAPTER III

ENERGY EQUATION CONSIDERATIONS

In the continuum flow regime of gasdynamics, the populations of the various atomic and molecular states important to the emission and absorption of radiation are, for cases of interest to us, given accurately by their equilibrium values. For our present purposes, the continuum flow regime can be defined as a regime where the excitation and deexcitation of the states occur primarily as a result of molecular collisions rather than through radiative emission and absorption. Thus, if the collisional processes are in quasi-equilibrium, the resulting distribution of the molecules among the energy levels is close to the Boltzmann result with the associated temperature being equal to the local gas temperature. The assumption that the energy levels are populated in a Boltzmann distribution is known as the quasi-equilibrium hypothesis or the assumption of local thermodynamic equilibrium (Vincenti and Kruger, 1965, Ch xi).

The general one-dimensional equation of radiative transfer under quasi-equilibrium conditions and ignoring scattering is (Vincenti and Kruger, 1965, Ch xi)

$$\frac{1}{c}\frac{\partial I_\nu}{\partial t} + \mu\frac{\partial I_\nu}{\partial x} = \alpha_\nu[B_\nu(T) - I_\nu] , \qquad 3.1$$

where μ is the cosine of the polar angle and accounts for radiative transfer skew to the coordinate direction, x. We take the one-dimensional radiative transfer equation to be valid in the vicinity of the stagnation point with variations normal to the body being important. This tangent slab approximation has been shown to be very accurate near the stagnation point when the shock stand off distance is small compared to the local radius of curvature (Olstad, 1971; Page, et al, 1968; and Cheng and Vincenti, 1967). The volumetric absorption coefficient α_ν includes the effect of induced emission. A detailed development of Eq. 3.1 based upon the notion of a photon distribution function can be found in Vincenti and Kruger (1965, Ch xi).

If we nondimensionalize Eq. 3.1 and consider the ratio of the time-derivative term to the spatial-derivative term we see that the coefficient is a speed ratio formed by the characteristic distance and time to the speed of light. We can, for the current problem, select the shock stand-off distance as the characteristic length and the time required for a particle to travel from the shock to the interface as the characteristic time. An upper limit on the resulting characteristic velocity would be the velocity just behind the shock which for the current nominal flight conditions is approximately 3,000 feet per second. The resulting speed ratio shows that the time-derivative term of Eq. 3.1 is approximately six orders of magnitude less than the spatial-derivative term and we can safely consider the time-independent form of Eq. 3.1

Before proceeding to the solution for the radiation intensity let us define the optical depth at a particular frequency by

$$\tau_\nu(x) = \int_0^x \alpha_\nu dx'. \tag{3.2}$$

With this definition, the time-independent form of Eq. 3.1 becomes

$$\mu \frac{dI_\nu}{d\tau_\nu} = B_\nu - I_\nu . \tag{3.3}$$

It is convenient to specify I_ν^+ as the intensity in the positive -x direction and I_ν^- as the intensity in the negative -x direction. We can now write equations for each direction of propagation. There results

$$\mu \frac{dI_\nu^+}{d\tau_\nu} = B_\nu - I_\nu^+ \tag{3.4}$$

and

$$- \mu \frac{dI_\nu^-}{d\tau_\nu} = B_\nu - I_\nu^- \tag{3.5}$$

where the minus sign on the left hand side of Eq. 3.5 accounts for propagation opposite to the direction of the positive coordinate. In both Eq. 3.4 and Eq. 3.5, μ is positive.

Let us now integrate Eqs. 3.4 and 3.5 for a parallel slab of gas as shown in Fig. 3.1, with the boundary conditions that at $\tau_\nu = 0$,

$$I_\nu^+ = I_\nu^+(0)$$

and at $\tau_\nu = \tau_{\nu,\Delta} \equiv \int_0^\Delta \alpha_\nu dx$

$$I_\nu^- = I_\nu^-(\tau_{\nu,\Delta}) .$$

In order to determine the intensity at any arbitrary point within the gas slab, we can integrate the differential equations from the point of the specified boundary condition to the arbitrary point. Using appropriate integration factors, we obtain

$$I_\nu^+ = I_\nu^+(0)e^{-\tau_\nu/\mu} + \frac{1}{\mu} e^{-\tau_\nu/\mu} \int_0^{\tau_\nu} e^{\tau_\nu'/\mu} B_\nu d\tau_\nu' \qquad 3.6$$

and

$$I_\nu^- = I_\nu^-(\tau_{\nu,\Delta})e^{(\tau_\nu - \tau_{\nu,\Delta})/\mu} + \frac{1}{\mu} e^{\tau_\nu/\mu} \int_{\tau_\nu}^{\tau_{\nu,\Delta}} e^{-\tau_\nu'/\mu} B_\nu d\tau_\nu' \ . \qquad 3.7$$

In general the boundary conditions on Eqs. 3.6 and 3.7 require simultaneous solution of the equations. This is a result of reflecting boundaries and can be seen by evaluating Eq. 3.6 at the boundary, $\tau_\nu = \tau_{\nu,\Delta}$. The result is

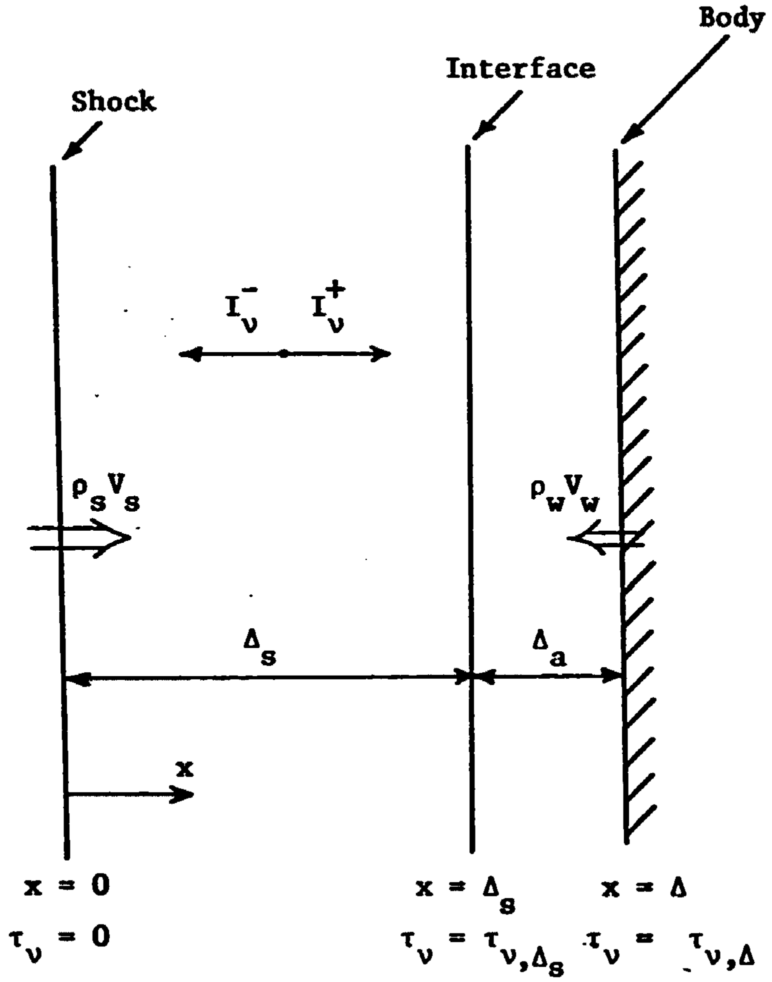

Figure 3.1 Stagnation Point Parallel Slab Geometry

$$I_\nu^+(\tau_{\nu,\Delta}) = I_\nu^+(0)e^{-\tau_{\nu,\Delta}/\mu} + \frac{1}{\mu}\, e^{-\tau_{\nu,\Delta}/\mu}\int_0^{\tau_{\nu,\Delta}} e^{\tau_\nu'/\mu} B_\nu d\tau_\nu' \qquad 3.8$$

which is the intensity incident from the positive direction on the boundary at $\tau_\nu = \tau_{\nu,\Delta}$. If we now assume the body surface at $x = \Delta$ to be opaque, there is no intensity transmitted in the negative direction and the total contribution to $I_\nu^-(\tau_{\nu,\Delta})$ is made-up of the reflected portion of $I_\nu^+(\tau_{\nu,\Delta})$ plus the emission due to surface temperature. By Kirchhoff's law, the portion of incident intensity that is reflected from an opaque surface is related to the incident intensity by $(1-\varepsilon_{\nu,w}(\mu))$, where $\varepsilon_{\nu,w}(\mu)$ is the spectral emissivity of the surface. If we further assume that the surface is diffuse and non-spectral, we can express the boundary conditions at $\tau_{\nu,\Delta}$ as

$$I_\nu^-(\tau_{\nu,\Delta}) = \varepsilon_w B_\nu(T_w) + (1-\varepsilon_w)1/\pi\int_0^{2\pi}\int_0^1 I_\nu^+(\tau_{\nu,\Delta})\mu d\mu d\phi \qquad 3.9$$

where $I_\nu^+(\tau_{\nu,\Delta})$ is given by Eq. 3.8. It is now clear that the boundary condition at $\tau_{\nu,\Delta}$ requires evaluation of the integral of Eq. 3.8 which in-turn requires the temperature profile. In most problems in radiative gasdynamics, the temperature is not known a priori, but is part of the solution.

As $\tau_{\nu,\Delta}$ corresponds to the body, Eq. 3.9 gives the intensity leaving the body and propagating toward the shock. The above characterization of the surface at $\tau_{\nu,\Delta}$ is typical of an ablative body and the assumptions of an opaque, diffuse surface will be maintained.

We can now consider the boundary at $\tau_\nu = 0$ (shock). Let us assume that the shock is transparent and that any incoming radiation due to the precursively heated atmosphere is negligible compared to radiation from the hot gas cap behind the strong shock. The radiation intensity passing through the shock and thus available for precursive heating is given by evaluating Eq. 3.7 at $\tau_\nu = 0$. The result is

$$I_\nu^-(0) = I_\nu^-(\tau_{\nu,\Delta})e^{-\tau_{\nu,\Delta}/\mu} + \frac{1}{\mu}\int_0^{\tau_{\nu,\Delta}/\mu} e^{-\tau_\nu'/\mu} B_\nu d\tau_\nu' \ . \qquad 3.10$$

Because there is no reflection at the shock (i.e., transparent shock assumption), and because we do not have a solid surface to emit, the boundary conditions at $\tau_\nu = 0$ is

$$I_\nu^+ = I_\nu^+(0) = 0 \ .$$

We can now incorporate the specific boundary conditions into Eqs. 3.6 and 3.7 to get

$$I_\nu^+ = \frac{1}{\mu}e^{-\tau_\nu/\mu}\int_0^{\tau_\nu} e^{\tau_\nu'/\mu} B_\nu d\tau_\nu' \qquad 3.11$$

and

$$I_\nu^- = [\varepsilon_w B_\nu(T_w) + (1-\varepsilon_w)2\int_0^1 e^{-\tau_{\nu,\Delta}/\mu}\int_0^{\tau_{\nu,\Delta}} e^{\tau_\nu'/\mu} B_\nu d\tau_\nu' d\mu]e^{(\tau_\nu-\tau_{\nu,\Delta})/\mu}$$
$$+ \frac{1}{\mu}e^{\tau_\nu/\mu}\int_{\tau_\nu}^{\tau_{\nu,\Delta}} e^{-\tau_\nu'/\mu} B_\nu d\tau_\nu' \ . \qquad 3.12$$

In general the net monochromatic radiative heat flux at any optical depth can be expressed as

$$q_\nu = 2\pi \int_0^1 [I_\nu^+ - I_\nu^-]\mu d\mu \ . \qquad 3.13$$

If we now substitute Eqs. 3.11 and 3.12 into Eq. 3.13 and integrate over μ, the resulting radiative flux is

$$q_\nu = 2\pi \left\{ \int_0^{\tau_\nu} B_\nu E_2(\tau_\nu - \tau_\nu')d\tau_\nu' - \int_{\tau_\nu}^{\tau_{\nu,\Delta}} B_\nu E_2(\tau_\nu' - \tau_\nu)d\tau_\nu' \right. \qquad 3.14$$

$$\left. -E_3(\tau_{\nu,\Delta} - \tau_\nu)\left[\varepsilon_w B_\nu(T_w) + 2\ (1-\varepsilon_w) \int_0^{\tau_{\nu,\Delta}} B_\nu E_2(\tau_{\nu,\Delta} - \tau_\nu')d\tau_\nu'\right]\right\}$$

where we have introduced the exponential integral defined by

$$E_n(x) = \int_0^1 \mu^{n-2} e^{-x/\mu} d\mu \ . \qquad 3.15$$

For future use, let us consider the net radiative heat flux incident on the body surface ($\tau_\nu = \tau_{\nu,\Delta}$). This flux is determined by simply evaluating Eq. 3.14 at $\tau_{\nu,\Delta}$ which yields

$$q_\nu(\tau_{\nu,\Delta}) = 2\pi\varepsilon_w \int_0^{\tau_{\nu,\Delta}} B_\nu E_2(\tau_{\nu,\Delta} - \tau_\nu')d\tau_\nu' - \pi\varepsilon_w B_\nu(T_w) \ . \qquad 3.16$$

In addition to the radiative flux, the body surface receives additional heat from conduction due to the gas temperature profile adjacent to the wall, homogeneous combustion of ablative gases and free stream oxygen, and hetrogeneous combustion of the ablative surface and free stream oxygen. The extent of combustion heating is dependent on the ablative material. A detailed discussion of combustion heating for a typical charring ablator (nylon phenolic) can be found in Wakefield and Lundell (1969). The last term in Eq. 3.16 actually represents cooling of the surface due to reradiation. In the general case there are other cooling mechanisms such as the sublimation or decomposition energy, aerodynamic blockage due to the relatively cool ablation products carrying energy by convection away from the wall, and conduction of energy into the virgin structure of ablative material.

For the case of a melting ablator it would be necessary to consider the breaking off and evaporation of liquid droplets. If we restrict our analysis to sublimating ablators, however, the above listed sources and sinks of energy should be complete. Let us also restrict ourselves, as we did in the momentum equation considerations (Chapter II) to the case of massive blowing. Because the boundary layer is blown away from the wall and the interface between the ablative products and the shocked free stream air is considered to be a contact surface with no diffusion, there will be no free stream oxygen available for combustion heating. The remaining source of heat from the gas in addition to radiation is conduction which is given by

$$q_{cond} = \left(k\frac{dT}{dx}\right|_{x = \Delta}. \qquad 3.17$$

The aerodynamic blockage can be expressed as

$$q_b = \rho_w V_w \left(h_w + \frac{V_w^2}{2}\right) \tag{3.18}$$

which is the energy convected away from the wall by the ablative products. The surface heat balance for a sublimating ablator in a massive blowing environment can be written as

$$q_{\substack{\text{conducted} \\ \text{into solid}}} + q_{\substack{\text{absorbed} \\ \text{in sublimation}}} = q^r + q_{cond} - q_b \tag{3.19}$$

where

$$q^r = \int_0^\infty q_\nu(\tau_{\nu,\Delta})d\nu - q^{rr} \tag{3.20}$$

and q^{rr} is the energy reradiated from the surface.

Let us now define an effective heat of ablation which grossly characterizes the solid conduction and surface sublimation. This effective heat of ablation will be a characteristic of the material but could be a function of the surface temperature and pressure (Martin, 1966). It is defined by

$$H^*_{eff}(T_w,P_w) = \frac{q^r + q_{cond} - q_b}{\rho_w V_w} . \tag{3.21}$$

The purpose of defining an effective heat of ablation is to be able to determine the mass flux of ablative products once the heat flux to the wall has been computed. Since q_b is an explicit function of the mass flux, it would be convenient to remove this dependence. This can be done by replacing q_b in Eq. 3.21 by the expression given in Eq. 3.18 yielding

$$H^*_{eff} = \frac{q^r + q_{cond}}{\rho_w V_w} - \left(h_w + \frac{V_w^2}{2}\right) . \qquad 3.22$$

For a nominal surface temperature of 5000°R and an ablation products specific heat at constant pressure of .24 Btu/lbm - °R, h_w is approximately 1200 Btu/lbm. If V_w were to be as high as 775 feet per second, which is extremely large, the ratio of wall enthalpy to kinetic energy would be of the order of 10^4. This clearly shows that $h_w >> V_w^2/2$ for the conditions of current interest and Eq. 3.22 when rearranged becomes

$$\rho_w V_w = \frac{q^r + q_{cond}}{H^*_{eff}(T_w,P_w) + h_w} \equiv \frac{q^r + q_{cond}}{H_{eff}(T_w,P_w)} \qquad 3.23$$

where H_{eff} without the asterisk includes the wall enthalpy.

Consider now the generalized energy equation as developed in Appendix A in the form

$$\rho v \frac{dh}{dz} + \frac{dq}{dz} = 0 \qquad 3.24$$

where

$$q = \int_0^\infty q_\nu d\nu - k \frac{dT}{dz} .$$

and z is the coordinate distance measured from the shock. Note that q contains both the radiative and conductive heat fluxes. Let us now return to Eq. 3.14 to determine the needed derivative of the radiative flux. If we recall the definition of optical depth as given by Eq. 3.2, we can see that

$$\frac{d\tau_\nu}{dz} = \alpha_\nu \, .$$

With this in mind the needed derivative of Eq. 3.14 is

$$\frac{dq_\nu}{dz} = 2\pi\Bigg\{-\alpha_\nu\int_0^{\tau_{\nu,\Delta}} B_\nu E_1(|\tau_\nu-\tau_\nu'|)d\tau_\nu' + 2B_\nu\alpha_\nu - E_2(\tau_{\nu,\Delta}-\tau_\nu)\alpha_\nu[\varepsilon_w B_\nu(T_w) + 2(1-\varepsilon_w)\int_0^{\tau_{\nu,\Delta}} B_\nu E_2(\tau_{\nu,\Delta}-\tau_\nu')d\tau_\nu']\Bigg\}. \qquad 3.25$$

Upon incorporating Eq. 3.25 and the Fourier heat conduction law into Eq. 3.24 the resulting energy equation is

$$\rho v\frac{dh}{dz} + 2\pi\int_0^\infty\Bigg\{-\alpha_\nu\int_0^{\tau_{\nu,\Delta}} B_\nu E_1(|\tau_\nu-\tau_\nu'|)d\tau_\nu' + 2B_\nu\alpha_\nu - E_2(\tau_{\nu,\Delta}-\tau_\nu)\,\alpha_\nu\,[\varepsilon_w B_\nu(T_w) + 2(1-\varepsilon_w)\int_0^{\tau_{\nu,\Delta}} B_\nu E_2(\tau_{\nu,\Delta}-\tau_\nu')d\tau_\nu']\Bigg\}d\nu - \frac{d}{dz}\left(k\frac{dT}{dz}\right) = 0 \, . \qquad 3.26$$

Let us now give the spectral dependent gas absorption coefficient by

$$\alpha_\nu = \sum_{j=1}^{JS} \alpha_j(P,T)\ H\ (\nu-\nu_{j-1})\ H\ (\nu_j-\nu) \tag{3.27}$$

where H(x) is the Heaviside function defined in Chapter II. Equation 3.27 is the classical "step-model" representation of the absorption coefficient. With this representation one can treat the absorption characteristics of a gas from the simple case of a grey model with one step to the exact absorption spectrum with its infinite number of steps. This technique has been used by many authors to accurately describe the detailed spectral output of a nuclear detonation. Typical calculations have been closely compared with experimental data and in general prove to be within experimental error (Private Communication with Maj W.A. Whitaker, Chief Scientist, Air Force Weapons Laboratory, Kirtland AFB, New Mexico 87117). If one is careful to select a step model which preserves energy through the band absorption and equivalent width calculations, the frequency integrated radiative heat flux can be extremely accurate. The particular step models used in this study are discussed in Appendix B.

With the step model of Eq. 3.27, the net heat flux at any point in the field is given by

$$q = 2\pi\sum_{j=1}^{JS}\left\{\int_0^{\tau_j} I_j E_2(\tau_j-\tau_j')d\tau_j' - \int_{\tau_j}^{\tau_{j,\Delta}} I_j E_2(\tau_j'-\tau_j)d\tau_j \right.$$

$$\left. - E_3(\tau_{j,\Delta}-\tau_j)[\varepsilon_w I_j(T_w) + 2(1-\varepsilon_w)\int_0^{\tau_{j,\Delta}} I_j E_2(\tau_{j,\Delta}-\tau_j')d\tau_j']\right\} - k\frac{dT}{dz} \tag{3.28}$$

where

$$I_j \equiv \int_{\nu_{j-1}}^{\nu_j} B_\nu d\nu \ .$$

The net heat flux to the wall is given by

$$q(\tau_\Delta) = 2\pi\varepsilon_w \sum_{j=1}^{JS} \int_0^{\tau_{j,\Delta}} I_j E_2(\tau_{j,\Delta}-\tau_j')d\tau_j' - \varepsilon_w \sigma T_w^4 - \left(k \frac{dT}{dz}\right|_w \qquad 3.29$$

where

$$\frac{\sigma T^4}{\pi} \equiv \int_0^\infty B_\nu d\nu$$

has been used. The energy equation, Eq. 3.26, becomes after interchanging the order of integration

$$\rho v \frac{dh}{dz} + 2\pi \sum_{j=1}^{N} \alpha_j \left\{ - \int_0^{\tau_{j,\Delta}} I_j E_1(|\tau_j-\tau_j'|)d\tau_j' + 2I_j \right.$$

$$- E_2(\tau_{j,\Delta}-\tau_j) \left[\varepsilon_w I_j(T_w)\right. \qquad 3.30$$

$$\left.\left. + 2(1-\varepsilon_w) \int_0^{\tau_{j,\Delta}} I_j E_2(\tau_{j,\Delta}-\tau_j')d\tau_j'\right]\right\} - \frac{d}{dz}\left(k \frac{dT}{dz}\right) = 0 \ .$$

In performing the frequency integration to obtain Eqs. 3.28, 3.29, and 3.30, we assumed that the step cut-off frequencies were constants and were the same for both the shock and ablation layers. Temperature and pressure dependent cut-off frequencies might be more appropriate, but would greatly complicate the analysis. The greater complication isn't really warranted as none of the accepted step models discussed in Appendix B incorporate this sophistication. There is no loss in generality in the absorption coefficient model by using the same cut-off frequencies for both the shock and ablation layers. This is demonstrated in Appendix B.

The final step in the energy equation considerations is to introduce the following set of nondimensional parameters and reduce Eqs. 3.28, 3.29, and 3.30 to nondimensional form. The nondimensional relations are

$$
\begin{aligned}
& z = \Delta_s \tilde{z},\ T(z) = T_s \tilde{T}(\tilde{z}),\ h(z) = h_s \tilde{h}(\tilde{z}) \\
& \rho v(z) = \rho_s v_s\, \tilde{\rho v}(\tilde{z}),\ \alpha_j(z,T) = \alpha_{P,s} \tilde{\alpha}_j(\tilde{z},\tilde{T}) \\
& \tau_j(z) = N_{Bu} \tilde{\tau}_j(\tilde{z}),\ h_{eff} = \tilde{h}_{eff} 2N_{Bu} \sigma T_s^4/\rho_s v_s \\
& I_j(T) = \left(\sigma T_s^4/\pi\right) \tilde{I}_j(\tilde{T}),\ k(T) = k_w \tilde{k}(\tilde{T}) \\
& h_s = h(T_s),\ k_w = k(T_w),\ q(z) = 2N_{Bu} \sigma T_s^4 \tilde{q}(\tilde{z}) \\
& N_{Pe} = \Delta_s \rho_s v_s h_s / k_w T_s \\
& \Gamma = 2\alpha_{p,s} \Delta_s \sigma T_s^4 / \rho_s v_s h_s \\
& N_{Bo} = \rho_s v_s h_s / 2\sigma T_s^4 \\
& N_{Bu} = \alpha_{p,s} \Delta_s = \Gamma N_{Bo} \\
& N_{CR} = k_w T_s / 2\Delta_s \sigma T_s^4 = N_{Bo}/N_{Pe} \quad .
\end{aligned}
\qquad 3.31
$$

In general the shock conditions were chosen as the basis for normalization. This was done because during the process of varying the ablation layer optical properties, conditions such as the ablation layer stand-off distance, Δ_a, and wall mass flux, $\rho_w V_w$, will change. The shock conditions conversely will remain constant because we have fixed the flight conditions and because of the "uncoupling" of the momentum and energy equations. The parameters N_{Pe}, Γ, N_{Bo}, N_{Bu}, and N_{CR} are the Péclet, radiation cooling, Boltzmann, Bouguer, and conduction-radiation numbers, respectively. These parameters, except for the last one, are widely used in the study of radiative gasdynamics and are discussed in detail by Goulard (1964) and Penner (1964). The conduction-radiation number is simply the ratio of the Boltzmann and Pe'clet numbers and is a measure of conduction at the wall for a cold wall and a linear temperature profile compared to the radiation at the shock. It is included in this study because of its convenience when conduction heat transfer is considered.

If we now substitute the nondimensional relations into Eqs. 3.28, 3.29, and 3.30, the resulting nondimensional forms are

$$\tilde{q} = \sum_{j=1}^{JS}\left\{\int_0^{\tilde{\tau}_j} \tilde{I}_j E_2[N_{Bu}(\tilde{\tau}_j-\tilde{\tau}_j')]d\tilde{\tau}_j' - \int_{\tilde{\tau}_j}^{\tilde{\tau}_{j,\tilde{\Delta}}} \tilde{I}_j E_2[N_{Bu}(\tilde{\tau}_j'-\tilde{\tau}_j)]d\tilde{\tau}_j'\right.$$

$$- E_3[N_{Bu}(\tilde{\tau}_{j,\Delta}-\tilde{\tau}_j)]\left[\frac{\varepsilon_w}{N_{Bu}}\,\tilde{I}_j(\tilde{T}_w)\right. \qquad 3.32$$

$$\left.\left. + 2(1-\varepsilon_w)\int_0^{\tilde{\tau}_{j,\tilde{\Delta}}} \tilde{I}_j E_2[N_{Bu}(\tilde{\tau}_{j,\Delta}-\tilde{\tau}_j')]d\tilde{\tau}_j'\right]\right\} - \frac{N_{CR}}{N_{Bu}}\,\tilde{k}\,\frac{d\tilde{T}}{d\tilde{z}} ,$$

$$\tilde{q}(\tilde{\tau}_{\tilde{\Delta}}) = \epsilon_w \sum_{j=1}^{JS} \left\{ \int_0^{\tilde{\tau}_{j,\tilde{\Delta}}} \tilde{I}_j E_2[N_{Bu}(\tilde{\tau}_{j,\tilde{\Delta}} - \tilde{\tau}_j')] d\tilde{\tau}_j' \right\} - \frac{\epsilon_w}{2N_{Bu}} \tilde{T}_w^4 - \frac{N_{CR}}{N_{Bu}} \left(\frac{d\tilde{T}}{d\tilde{z}} \right|_w , \tag{3.33}$$

and

$$\tilde{\rho}v \frac{d\tilde{h}}{d\tilde{z}} + \Gamma N_{Bu} \sum_{j=1}^{JS} \tilde{\alpha}_j \left\{ - \int_0^{\tilde{\tau}_{j,\tilde{\Delta}}} \tilde{I}_j E_1(N_{Bu} \mid \tilde{\tau}_j - \tilde{\tau}_j' \mid) d\tilde{\tau}_j' + \frac{2}{N_{Bu}} \tilde{I}_j \right.$$

$$- E_2[N_{Bu}(\tilde{\tau}_{j,\tilde{\Delta}} - \tilde{\tau}_j)] \left[\frac{\epsilon_w}{N_{Bu}} \tilde{I}_j(\tilde{T}_w) \right. \tag{3.34}$$

$$\left. \left. + 2(1-\epsilon_w) \int_0^{\tilde{\tau}_{j,\tilde{\Delta}}} \tilde{I}_j E_2[N_{Bu}(\tilde{\tau}_{j,\tilde{\Delta}} - \tilde{\tau}_j')] d\tilde{\tau}_j' \right] \right\}$$

$$- N_{Pe}^{-1} \frac{d}{d\tilde{z}} \left(\tilde{k} \frac{d\tilde{T}}{d\tilde{z}} \right) = 0 .$$

For future use it will be convenient to define the divergence of the radiative flux as

$$\frac{d\tilde{q}^r}{d\tilde{z}} = N_{Bu} \sum_{j=1}^{JS} \tilde{\alpha}_j \left\{ - \int_0^{\tilde{\tau}_{j,\tilde{\Delta}}} \tilde{I}_j E_1(N_{Bu} \mid \tilde{\tau}_j - \tilde{\tau}_j' \mid) d\tilde{\tau}_j' + \frac{2}{N_{Bu}} \tilde{I}_j \right.$$

$$- E_2[N_{Bu}(\tilde{\tau}_{j,\tilde{\Delta}} - \tilde{\tau}_j)] \left[\frac{\epsilon_w}{N_{Bu}} \tilde{I}_j(\tilde{T}_w) \right. \tag{3.35}$$

$$\left. \left. + 2(1-\epsilon_w) \int_0^{\tilde{\tau}_{j,\tilde{\Delta}}} \tilde{I}_j E_2[N_{Bu}(\tilde{\tau}_{j,\tilde{\Delta}} - \tilde{\tau}_j')] d\tilde{\tau}_j' \right] \right\} .$$

This then allows the energy equation (Eq. 3.34) to be written in the convenient form

$$N_{Pe}^{-1} \frac{d}{d\tilde{z}}\left(\tilde{k}\,\frac{d\tilde{T}}{d\tilde{z}}\right) - \tilde{\rho v}\,\frac{d\tilde{h}}{d\tilde{z}} - \Gamma\,\frac{d\tilde{q}^{r}}{d\tilde{z}} = 0 \; . \qquad 3.36$$

In the remainder of this paper the tildes will be dropped as all variables, except when clearly specified, will be nondimensional.

CHAPTER IV

SOLUTION APPROACH

The necessary equations are now established and we can proceed toward the desired goal of determining the optimum optical properties of an ablator material. Because the problem is to optimize a function, namely the absorption coefficient of the ablated gases, the use of variational methods might seem appropriate. An attempt along these lines would involve minimizing the total heat flux to the wall as given by Eq. 3.33 with the constraints of the energy equation (Eq. 3.36) and the surface mass-energy balance (Eq. 3.23). An analytical formulation of the variational problem was attempted, but the resulting Euler-Lagrange equations (Hildebrand, 1965, Sec 2.7) were intractable

This result led to the investigation of numerical techniques for solving optimization problems. The Rayleigh-Ritz method (Hildebrand, 1965, Sec 2.19) was formulated, but in order to form a workable system of equations, the assumptions were so restrictive that meaningful results did not seem possible. The most promising and flexible numerical optimization technique appeared to be some form of the method of steepest ascents (Bryson and Denham, 1962). This method was programmed and used to successfully solve numerically a problem posed by Schechter (1967, p 54) for which an analytical solution to the Euler-Lagrange equations was obtained. With this success on the example problem, the grey-gas energy equation, Eq. 3.34 with JS equal 1, was cast in Bryson's optimum control form and the necessary auxiliary and constraint equations were established.

The method of steepest ascents (See Bryson and Denham, 1962; Bryson et al, 1962; Bryson and Ho, 1969; and Gera, 1970 for details) involves solutions to two-point boundary value problems with the optimization of a control variable to render stationary a specified parameter. In the current radiative gasdynamics problem, the control variable is the absorption coefficient of the ablated gases and the parameter to be made stationary is the ablation mass loss rate. The solution procedure is to guess a control variable profile and integrate the energy equation with the known boundary condition and an assumed boundary condition. If we integrate from the shock to the body, the temperature at the shock is the known boundary condition. Since the grey-gas energy equation in optimimum control form is a second order ordinary integro-differential equation, only two boundary conditions are required. However as the problem is posed, the shock and wall temperatures are the two known boundary conditions, whence the two-point boundary value problem is produced. The assumed boundary condition can be taken as the slope of the temperature profile at the shock. In theory, the energy equation is now integrated twice to yield a calculated wall temperature. This temperature is then compared to the specified wall temperature, and the slope at the shock can be adjusted appropriately. The method of steepest ascents is then applied by examining the effect of small perturbations in the control variable profile on the parameter to be made stationary and the specified terminal condition. The result is a new control variable program and a new initial condition guess. The iteration proceeds until we have a stationary parameter and have matched the specified wall temperature.

In applying this technique to the massive blowing problem, considerable difficulty was encountered owing to the unstable nature of the energy equation with respect to this type of direct integration. For example, changes in the guessed temperature slope at the shock of the order of 10^{-5} yielded solutions that tended from plus infinity to minus infinity. Because of this instability and the resulting lack of control over the temperature at the terminal end of the integration, it was concluded that the method of steepest ascents was not appropriate for a solution to the current problem.

At this time the solution approach undertaken was a straight forward technique of optimization by parameter variation. This involves a fully-coupled solution of the equations with a specified temperature dependent ablated-gas absorption coefficient. The next step is to enhance the absorption by some programed factor and obtain another solution. This corresponds to seeding the ablative material with a substance that is highly absorbing in the shocked gas spectral bands. If we continue to enhance the absorption coefficient and obtain solutions, including the wall mass flux, for each degree of enhancement; and if a minimum in the mass flux versus enhancement occurs, we have found the optimum degree of enhancement and thus the optimum characteristics for the absorption coefficient of the ablator.

Because of the stability problems associated with direct integration of the energy equation, it was decided that an iterative scheme beginning with a specified temperature profile would be most appropriate. Callis (1968) adopted a time asymptotic technique, "--------because it seemed to offer a direct solution to the problem at hand (radiation-coupled stagnation-line solutions for hypervelocity blunt bodies) with a minimum number of restrictive assumptions and computational difficulties." He was able to conclude that over a wide range of conditions the time asymptotic technique can be successfully and efficiently applied to the analysis of radiation-coupled flow fields including effects of nongrey emission and absorption. Callis' assumptions were similar to those imposed in the current study but he added the additional restrictions of a nonconducting fluid and a cold and nonablating wall. Moretti and Albbett (1966) have demonstrated that nonradiating flow field calculations can be carried on in the entire flow field of a blunt body using time asymptotic techniques with few of the usual problems of convergence, stability, or sensitivity to the initial guesses. Other authors such as Chin (1968) and Page et al. (1968) have chosen to perform iterative calculations by assuming a temperature profile, computing the divergence of the radiative flux and then after dividing the space-discrete radiative flux by the momentum flux, integrating for a new temperature profile. As can be seen from the energy equation in the form

$$\rho v \frac{dh}{dy} = -\frac{dq^r}{dy},$$

which was used by both Chin and Page, the temperature profile becomes infinite when the mass flux goes to zero if one does not at that point exactly satisfy the condition of radiative equilibrium. The latter is especially difficult to insure as the radiative flux divergence depends upon the entire shock layer temperature profile through the absorption integral. Page avoided this problem by considering only 99% of the shock layer. Also, ablation was not considered. Chin does not discuss the problem, but does point out that in the air layer, integration is performed from the shock to the interface, while in the ablation layer the integration goes from the wall to the interface. Since Chin considers blowing, the mass flux is nonzero at the wall but goes to zero at the interface and this is where one must use some special technique.

This computational difficulty is completely eliminated when one includes the mechanism of thermal conduction as is done in the current analysis. The inclusion of thermal conduction was previously proven successful by Hoshizaki and Wilson (1965) and Nerem (1966). In addition to thermal conduction, both of these analyses included viscous effects from the shock to the body which eliminates the matching of an inviscid shock layer with a viscous boundary layer. The fully viscous treatment or a boundary-layer analysis is extremely important in determining the convective heat flux to the body for a nonablating body, but in the massive blowing problem the large thermal and velocity gradients are far enough removed from the wall that radiation, which isn't strongly effected by these gradients, is usually the dominant mode of heat transfer. As pointed out by Anderson (1968), the incorrect treatment of the region where the mass flux goes to zero does not greatly influence the radiative heat transfer, but it does preclude the calculation of convective heat transfer by usual boundary layer techniques.

With these considerations in mind, we can now proceed to the numerical techniques used in the current analysis. The energy equation (Eq. 3.36) can be expressed as

$$\frac{\partial T}{\partial t} = N_{Pe}^{-1} \frac{\partial}{\partial z}\left(k \frac{\partial T}{\partial z}\right) - \rho v \frac{\partial h}{\partial z} - \Gamma \frac{\partial q^r}{\partial z} \qquad 4.1$$

where $\frac{\partial q^r}{\partial z}$ is given by Eq. 3.35 and the tildes have been dropped as everything is nondimensional. In Eq. 4.1 we have replaced the zero of Eq. 3.36 with the temperature derivative with respect to t thus yielding a partial differential equation. The symbol "t" will be referred to as time, but is clearly seen to be some artificial independent variable. This form of the energy equation was chosen for the iterative solution because it casts the equation as the classical time-dependent one-dimensional diffusion or heat equation with convection and a source term. The advantage of this cast is the extensive treatment in the literature (See for example Richtmyer and Morton, 1967; Carnahan, et al, 1969; and the series *Methods in Computational Physics*, Academic Press) of this equation with the possible convergence difficulties and suggested means of stabilization. For example consider the first term on the right hand side of Eq. 4.1. If we expand this term analytically we get

$$\frac{\partial}{\partial z}\left(k(T)\,\frac{\partial T}{\partial z}\right) = \frac{\partial k}{\partial T}\left(\frac{\partial T}{\partial z}\right)^2 + k(T)\,\frac{\partial^2 T}{\partial z^2}\,.$$

This yields a nonlinear term in $\left(\frac{\partial T}{\partial z}\right)^2$ which can cause stability problems in difference form. An alternative procedure could be to apply the transformation

$$y = \int 1/k\;dz$$

in terms of which

$$\frac{\partial}{\partial z}\left(k\,\frac{\partial T}{\partial z}\right) \to \frac{\partial^2 T}{\partial y^2}$$

(Richtmyer and Morton, 1967, p 194). The difficulty with this new coordinate system is that a fixed step size in z yields a small step size in y where k is large. Since k in general increases with the temperature, this transformation would yield very fine zoning near the shock and coarse zoning around the interface and toward the wall. Near the shock, the temperature slope is near zero and a coarse mesh is acceptable, while near the interface the temperature slope is large and requires a fine mesh. A fixed step size in y would result in correct zoning in z, but it was determined that for the current problem the added complexity due primarily to the flux divergence term in Eq. 4.1 did not warrant the transformation. A third alternative which is suggested by Richtmyer and Morton (1967, p 198) is

$$\frac{\partial}{\partial z}\left(k\,\frac{\partial T}{\partial z}\right) = \frac{\theta[\delta(k\delta T)]_i^{n+1} + (1-\theta)[\delta(k\delta T)]_i^n}{(\Delta z)^2} \qquad 4.2$$

where θ is a positive constant; $\theta = 0$ gives a four-point explicit scheme and all other values of θ give implicit schemes. The symbol δ stands for the centered space difference as defined by

$$\delta F_i = F[(i+\tfrac{1}{2})\Delta z] - F[(i-\tfrac{1}{2})\Delta z]$$

and

$$\delta^2 F_i = F[(i+1)\Delta z] - 2F(i\Delta z) + F[(i-1)\Delta z]$$

which in subscript difference notation becomes

$$\delta F_i = F_{i+\frac{1}{2}} - F_{i-\frac{1}{2}}$$

and

$$\delta^2 F_i = F_{i+1} - 2F_i + F_{i-1} \quad .$$

In the expansion of Eq. 4.2, the thermal conductivity must be evaluated at ½ mesh points. The current analysis defines quantities at whole mesh points and thus

$$k_{i+\frac{1}{2}} = \frac{k_i + k_{i+1}}{2}$$

and

$$k_{i-\frac{1}{2}} = \frac{k_{i-1} + k_i}{2}$$

must be defined. If we base our stability criterion on this conduction term alone, i.e. assume our energy equation is

$$\frac{\partial T}{\partial t} = N_{Pe}^{-1} \frac{\partial}{\partial z}\left(k \frac{\partial T}{\partial z}\right), \qquad 4.3$$

one would expect, as an extension of the case where k is constant (Richtmyer and Morton, 1967, p 205), stability if

$$\frac{2k\Delta t}{(\Delta z)^2 N_{Pe}} < \frac{1}{1 - 2\theta} \quad \text{for } 0 \leq \theta < \tfrac{1}{2}$$

and no restriction for $\frac{1}{2} \leq \theta \leq 1$. One might consider only implicit schemes ($\theta \neq 0$) because of no restriction on stability, but after examination of Richtmyer and Morton (1967, p189, Table 8.1) it is clear that for even the simplest case of constant thermal conductivity other factors such as truncation error, complexity of the difference scheme, and computation time must be considered. For example if one is able to increase the time step by an order of magnitude by going to an implicit scheme, total computation time to arrive at a final problem time could be larger for a particular system of equations.

This is because the implicit scheme requires the solution of a three by the number of space mesh points matrix at each time step.

Before leaving the conduction term it is appropriate to quote Richtmyer and Morton (1967,p 205), "Note that for nonlinear problems stability depends not only on the structure of the finite-difference system but also generally on the solution being obtained; and for a given solution, the system may be stable for some values of t and not for others." Richtmyer and Morton's statement was based on Eq. 4.3 and desiring a solution in only a limited range of t. In the current analysis, we are obtaining a solution to Eq. 4.1 which, in addition to the conduction term, contains a nonlinear lower-order convective term and a radiation term that must be treated explicitly in all cases. We are also considering all values of t since we are seeking the time asymptotic solution.

Consider now the second term on the right hand side of Eq. 4.1. The simplest difference scheme is

$$\rho v \frac{\partial h}{\partial z} = \left(\rho v \frac{\partial h}{\partial T}\right) \frac{\partial T}{\partial z} = \left[\rho v \frac{\partial h}{\partial T}\right]_j \left(\frac{T_{j+1} - T_{j-1}}{2\Delta z}\right),$$

but this scheme is well known to be unstable and to first order is in fact an approximation to

$$-\left(\rho v \frac{\partial h}{\partial T}\right) \frac{\partial T}{\partial z} - \frac{1}{2}\left(\rho v \frac{\partial h}{\partial T}\right)^2 \Delta t \frac{\partial^2 T}{\partial z^2}$$

whose solution grows exponentially with time (Roberts and Weiss, 1966).

Other simple difference schemes that are stable can be obtained if one is only interested in the convective term of Eq. 4.1, i.e. the approximation

$$\frac{\partial T}{\partial t} = - \rho v \frac{\partial T}{\partial z} . \qquad 4.4$$

A scheme suggested by Byers and Killen (1970) is

$$T_i^{n+1} = \frac{1}{2}\left(T_{i+1}^n + T_{i-1}^n\right) - \frac{\Delta t}{2\Delta z}\left(\rho v\right)_i^n\left(T_{i+1}^n - T_{i-1}^n\right). \qquad 4.5$$

The stability criterion is

$$\left| \frac{\rho v \Delta t}{\Delta z} \right| < 1$$

for all values of ρv. The difficulty with Eq. 4.5 is the incompatibility with the other terms of Eq. 4.1 but for the solution to Eq. 4.4 it is acceptable. Another stable scheme (Byers and Killen, 1970) is the "upstream-downstream" difference equation which is

$$T_i^{n+1} = T_i^n - \frac{(\rho v)_i^n \Delta t}{\Delta z}\begin{cases} T_{i+1}^n - T_i^n & \text{if } (\rho v)_i^n < 0, \\ T_i^n - T_{n-1}^n & \text{if } (\rho v)_i^n > 0 \end{cases} \qquad 4.6$$

with the same stability criterion as Eq. 4.5. For the current problem, both the upstream and downstream differences will be needed because ρv changes sign at the interface between the shock layer and ablative layer. Other schemes such as the "leapfrog" difference equation which is higher order accurate but a three time level equation and Taylor Series expansion in time which become extremely complicated because of the variable coefficient are available but not clearly necessary for this current problem.

It should be pointed out that the above discussion of stability for the various difference techniques is based on simple equations like Eqs. 4.3 and 4.4 and even though the stability criterion is met for the convective term and the conductive term individually, the combined difference equation could be unstable. Conversely an "unstable" scheme like the simple centered difference could be stable when in combination with other terms. In the current analysis, the upstream-downstream difference equation (Eq. 4.6) was used for the convective term when Eq. 4.2 was used in the explicit mode ($\theta = 0$) and, the simple centered difference was used for the implicit mode (the only implicit mode exercised was $\theta = 1$ which is a full implicit four-point scheme with backward time differencing).

The last term in Eq. 4.1 is integral and nonlinear as can be seen from Eq. 3.35 and can not be treated implicitly without considerable simplification. If one were to assume an emission dominated gas with cold nonreflecting boundaries, then the nonlinearity of this radiation term would be revealed as $\alpha_p T^4$ which could be linearized by

$$\left(\alpha_p T^4\right)_i^{n+1} \simeq \left(\alpha_p T^4\right)_i^n + 4\left(\alpha_p T^3\right)_i^n \left(T_i^{n+1} - T_i^n\right) ,$$

(Richtmyer and Morton, 1967). Note that the linearization in T_i^{n+1}

allows an implicit solution scheme. Because these assumptions are too restrictive for the current problem, the radiation term was treated including all the physics offered by Eq. 3.35. This requires explicit treatment of the radiation term and when this term becomes dominant there are severe restrictions on the time step.

We can now express the selected explicit difference scheme for Eq. 4.1 as

$$\frac{T_i^{n+1} - T_i^n}{\Delta t} = \frac{1}{2N_{Pe}(\Delta z)^2}\Big[\left(k_i^n + k_{i+1}^n\right)\left(T_{i+1}^n - T_i^n\right) - \left(k_{i-1}^n + k_i^n\right)\left(T_i^n - T_{i-1}^n\right)\Big] - \left(\frac{\partial h}{\partial T}\right)_i^n \frac{(\rho v)_i^n}{\Delta z}\Big\{H\left[(\rho v)_i^n\right]\left(T_i^n - T_{i-1}^n\right) + H\left[-(\rho v)_i^n\right]\left(T_{i+1}^n - T_i^n\right)\Big\} - \Gamma\left(\frac{\partial q}{\partial z}\right)_i^n \qquad 4.7$$

where H(x) is the Heaviside function defined in Chapter II and $\left(\frac{\partial q}{\partial z}\right)_i^n$ is discussed in Appendix C. The stability criterion based on the conduction term yields a time step of approximately 10^{-3} while the convective term yields approximately 5×10^{-3}. With this in mind the explicit code was set up to compute a time step based on the conduction term and then reduce this step if the solution diverged.

The implicit difference scheme is given by

$$\frac{T_i^{n+1} - T_i^n}{\Delta t} = \frac{1}{2N_{Pe}(\Delta z)^2}\Big[\left(k_i^n + k_{i+1}^n\right)\left(T_{i+1}^{n+1} - T_i^{n+1}\right) - \left(k_i^n + k_{i-1}^n\right)\left(T_i^{n+1} - T_{i-1}^{n+1}\right)\Big] - \left(\frac{\partial h}{\partial T}\right)_i^n \frac{(\rho v)_i^n}{2(\Delta z)}\left(T_{i+1}^{n+1} - T_{i-1}^{n+1}\right) - \Gamma\left(\frac{\partial q}{\partial z}\right)_i^n \qquad 4.8$$

where the major distinction from the explicit scheme is the evaluation of the temperature at the updated time (n+1). Since the right hand side of Eq. 4.8 is a function of T^{n+1}, the implicit method, involving the solution of a number-of-mesh-points-minus-two square matrix at each time step, is necessary. After one expands Eq. 4.8 it is apparent as demonstrated in Appendix D that the resulting matrix is tridiagonal and thus the solution is greatly simplified.

In order to determine the best solution technique (explicit or implicit) for the current problem, numerical experiments were made with the following conditions: free stream velocity of 50,000 feet per second altitude of 200,000 feet, and an ablator effective heat of ablation of 184 B.T.U. per pound mass. The same initial temperature profile and wall mass flux were assumed. The explicit code incorporated Eq. 4.7 to update the temperature profile and used a time step of 1.7×10^{-3} computed from the conduction term stability criterion. After six iterations the solution started to diverge and an automatic check in the code halved the time step allowing the solution to proceed an additional 826 iterations. The CDC 6600 central processor time required for compilation and 832 iterations was 512 seconds. An additional parameter of interest is $(\Delta T_i/\Delta t)_{max}$ which as can be seen from Eqs. 4.1, 4.7, or 4.8 is the measure of convergence to the "steady-state" or the time asymptotic solution. This parameter at 832 iterations had reduced to 3.0257×10^{-2}.

The implicit code using Eq. 4.8 was run with a time step of 10^{-2}, approximately an order of magnitude larger than the explicit code. A later run with a time step of 10^{-1} proved stable, but the data for the 10^{-2} run will be used for the comparison with the explicit code. After 84 iterations $(\Delta T_i/\Delta t)_{max}$ was down to $3.019x10^{-2}$ and the lapsed computer time was approximately 54 seconds. This is almost an order of magnitude savings in computer time. A larger time step, if stable as was 10^{-1} in the latter run, would result in an approximately proportional reduction in computer time required to reach a specified value of $(\Delta T_i/\Delta t)_{max}$. As a result of these comparisons it was determined that for the current class of problems the implicit method of solving the energy equation would yield a computer time savings of one to two orders of magnitude. Therefore, the implicit method (Eq. 4.8) was used for the remainder of the study.

In order to determine a reasonable value of $(\Delta T_i/\Delta t)_{max}$ for convergence, the implicit run with Δt of 10^{-2} was carried out to 950 iterations. At 476 iterations the wall mass flux reached .49022 pounds mass per square foot-second with $(\Delta T_i/\Delta t)_{max}$ equal $8.766x10^{-5}$. At 950 iterations the wall mass flux had not changed and $(\Delta T_i/\Delta t)_{max}$ had dropped to $9.9452x10^{-8}$. This is a clear indication that for these flight and material conditions convergence is reached when $(\Delta T_i/\Delta t)_{max}$ reduces to approximately 10^{-4}. Based on this numerical experiment the convergence criterion is assumed to be extendable to the complete class of problems that are currently under consideration. Since the computer time is proportional to the number of iterations, some runs were terminated and considered converged with $(\Delta T_i/\Delta t)_{max}$ larger than 10^{-4}. However, as was determined from this numerical experiment, stopping the calculation at approximately 100 iterations, more than one fourth time savings, yielded a $(\Delta T_i/\Delta t)_{max}$ of near 10^{-2} and an error in mass flux of less than 4%. This error is based on 950 iteration data being "exact".

It is important to note that although the implicit method was used throughout the study, the gas thermal conductivity, equation of state, and radiative flux divergence term are treated explicitly. This is necessary in order to have a linear system of equations as is pointed-out in Appendix D. The explicit coefficients cause no accuracy problem because we are seeking the time asymptotic solution, but for a true time dependent solution where intermediate time results are important, an iterative or averaging technique must be applied to these coefficients. The radiative flux divergence term does cause problems with the implicit time step because as absorption enhancement gets large this explicit term becomes dominant and controls the maximum allowable time step. Thus for large enhancement the time step was reduced to as low as 5×10^{-4} in order to maintain stability.

An additional numerical experiment was conducted to study the effects of different space step sizes for a fixed time step and convergence value of $(\Delta T_i/\Delta t)_{max}$. The three space step schemes were a fixed step size of 10^{-2}, a fixed step size of 10^{-3}, and a variable step size which changes from 10^{-2}, near the shock and wall where the temperature slope is fairly constant to 10^{-3} near the interface where the temperature slope is large. These step sizes are in nondimensional lengths which have the shock stand-off distance from the interface as a basis. Since the difference scheme becomes more accurate as the mesh size gets smaller, the 10^{-3} fixed step size was taken as "exact". The error in the wall mass flux with the variable step size was zero to the nearest ten thousandth and less than .02% with the 10^{-2} step size. This would suggest use of the larger step size since there is no appreciable impairment of accuracy and it reduces in this example the number of mesh points by an order of magnitude. The larger step size was used for calculations with little or no absorption enhancement and nose radii equal to or greater than one foot. For large enhancement and small nose radii, however, the conduction at the wall became important and larger, 10^{-2} or greater, step sizes caused instabilities. These instabilities resulted from changing the wall flux and thus the distance between the interface and the wall. These changes must be made in full space step increments and the larger mesh sizes caused temperature slope fluctuations near the wall that were too large for stability. Thus for stability a fixed step size of 10^{-3} was used for the calculations with appreciable enhancement.

One additional stabilizing technique should be mentioned before leaving this chapter. As pointed out in Chapter II, it is necessary to assume a value for the wall mass flux (or wall velocity for a specified ablation gas density) in order to determine the interface stand-off distance from the wall and thus the momentum profile in the ablation layer. With this boundary condition assumed, the solution proceeds and produces a net heat flux to the wall. Then by using Eq. 3.23 a corrected value of the wall mass flux is determined. It would seem that the computed value of the wall mass flux could used as the needed momentum boundary condition for the next iteration and as convergence, based on $(\Delta T_i/\Delta t)_{max}$, is reached there would be no change in predicted and computed values of the wall mass flux. This technique was used for little or no absorption enhancement and large nose radii and led to no difficulties because the adjustments in the interface stand-off distance required adding or removing temperature mesh points in an isothermal layer. Under conditions where the ablation layer was not isothermal, however, it became necessary to apply the damping technique

$$\dot{m}_u' = \theta\dot{m}_u + (1-\theta)\dot{m}_p \qquad 4.9$$

where $\dot{m}_u$ is the value used in the completed iteration, $\dot{m}_p$ is the value predicted by the completed iteration, $\dot{m}_u'$ is the value to be used in next iteration, and θ is a factor between zero and one. A θ of unity is the most stable condition but as is seen from Eq. 4.9 this would result in a fixed wall mass flux. A θ of zero is acceptable when the initial guess on $\dot{m}_u$ is very good and was used in the calculations with little or no enhancement. For the more severe conditions with respect to stability (i.e., large absorption enhancement) θ was set to unity until $(\Delta T_i/\Delta t)_{max}$ reached convergence. Then $\dot{m}_u$ and $\dot{m}_p$ were compared and if they were within 1% the calculation was terminated. If the two values were not within 1% Eq. 4.9 was applied with θ some value other than unity and the iterations were continued. Changing $\dot{m}_u$ always results in increasing $(\Delta T_i/\Delta t)_{max}$ and the solution must be again driven to convergence. This technique is time consuming but was the only method found stable enough to treat the large absorption enhancement cases.

With the considerations of this chapter in mind, the solution procedure can be summarized as follows:

1. Set trajectory and body conditions

2. Specify absorption coefficient model (i.e., grey gas or two step continuum by JS = 1 or 2 respectively; the code is written to treat general step models by simple data addition to the ALP subroutine)

3. Assume a temperature profile

4. Assume a wall mass flux

5. Compute the stagnation point geometry and momentum flow field

6. Evaluate the radiation flux divergence

7. Up-date the temperature profile by solving the energy equation

8. Compute $(\Delta T_i/\Delta t)_{max}$ and compare with convergence criterion

9. Compute heat fluxes and with wall heat flux determine resulting wall mass flux

10. Compare used and computed wall mass flux

11. If $(\Delta T_i/\Delta t)_{max}$ is greater than the convergence criterion go back to 6

12. If $(\Delta T_i/\Delta t)_{max}$ is equal to or less than the convergence criterion but $\dot{m}_u$ and $\dot{m}_p$ are not within 1%, compute $\dot{m}_u$ and go back to 5

13. If $(\Delta T_i/\Delta t)_{max}$ is equal to or less than the convergence criterion and $\dot{m}_u$ and $\dot{m}_p$ are within 1%, solution is complete.

CHAPTER V

RESULTS

Before we discuss the effects of ablation product enhancement, let us compare the present results with those of other analyses for the case of no enhancement. Throughout this chapter, the reference conditions, except where clearly specified, will be:

Altitude	-	190,000 feet
Velocity	-	55,000 feet per second
Nose radius	-	1 foot
Wall temperature	-	54000 °R (3000 °K)
Effective heat of ablation	-	2200 Btu per pound mass
Wall emissivity	-	1

These conditions were chosen because of the prevalence in the literature of results with these nominal conditions. Even though there is an exchange of energy between the shock and ablation layers which results in energy or temperature profile changes for different ablation properties, the shock and wall conditions are constant. These constant conditions were used in Eq. 3.31 to define characteristic numbers and nondimensionalizing parameters. For the stated reference conditions we then have:

Wall thermal conductivity	-	5.41×10^{-5} $\frac{\text{Btu}}{\text{ft-sec-°R}}$
Wall density	-	.1 lbm/ft^3
Shock temperature	-	30,280°R (16,820°K)
Shock density ratio	-	.059
Shock pressure	-	.98 atmospheres
Shock enthalpy	-	48,820 Btu/lbm
Shock mass flux	-	1.548 lbm/ft^2-sec
Shock stand-off distance	-	.044 feet
Shock Planck mean absorption coefficient	-	.128 feet^{-1}
Shock thermal conductivity	-	1.39×10^{-3} $\frac{\text{Btu}}{\text{ft-sec-°R}}$
Péclet number	-	2.049×10^3
Radiation cooling number	-	.0602
Boltzmann number	-	.0944
Bouguer number	-	5.68×10^{-3}
Conduction-radiation number	-	4.61×10^{-5}
Heat flux normalization factor	-	4545 Btu/ft^2-sec

A comparison of the tangential velocity profiles obtained in the present analysis with those of Wilson (1970) is given in Fig. 5.1. The Wilson data are for a viscous shock layer with the approximation of $\rho\mu$ = constant. The latter approximation is apparently good as the results are close to the more exact solution of Howe and Viegas (1963).

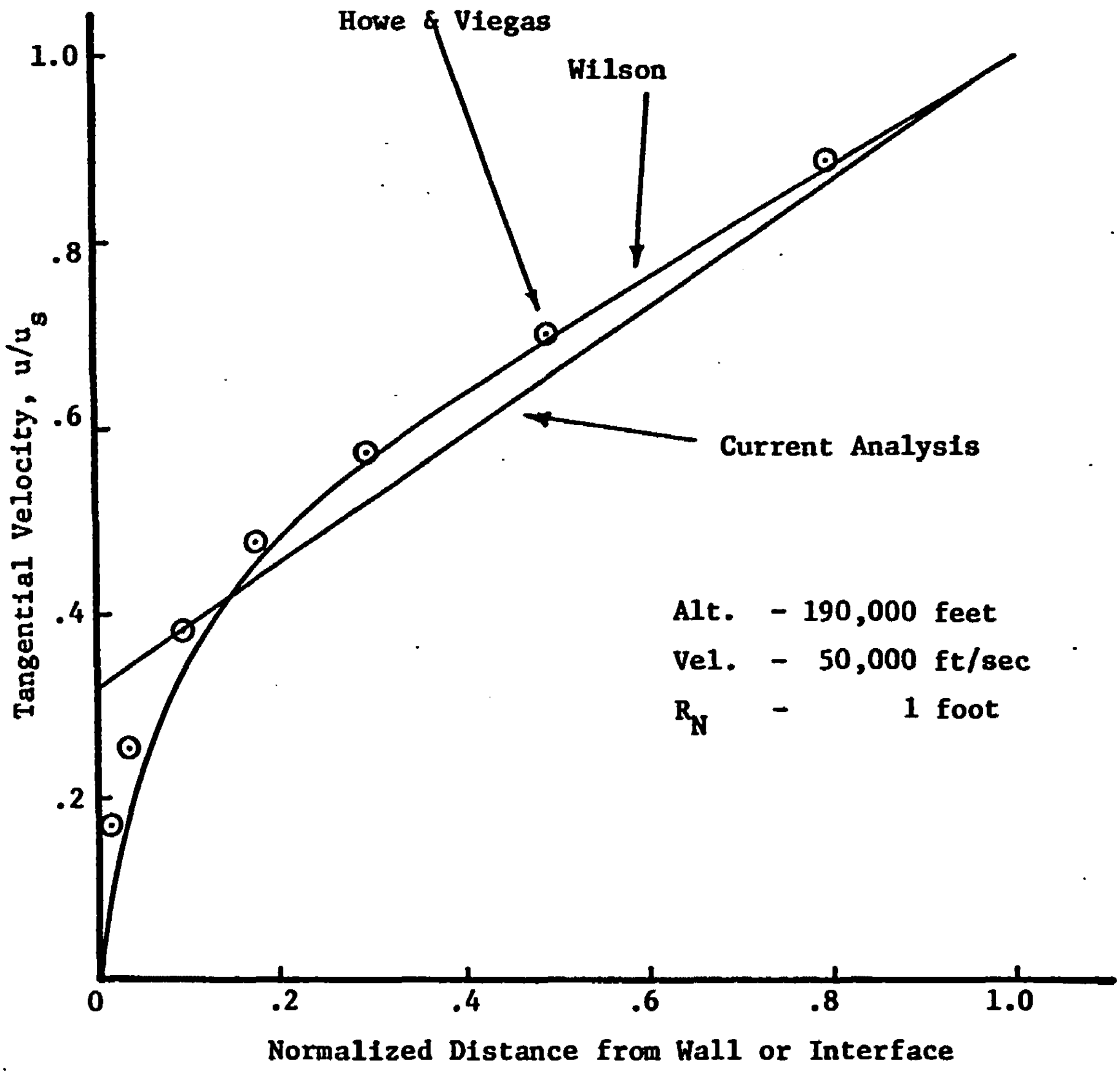

Figure 5.1 Tangential Velocity Comparison with Viscous Non-blowing Results

Both of these analyses are for three-dimensional stagnation point calculations with zero blowing, i.e. zero mass flux from the wall. The absissa zero of Fig. 5.1 corresponds to the wall for both the Wilson and Howe and Viegas data but is the interface or slip-layer in the current analysis. As will be discussed in more detail later, Wilson used his differential solution to treat the problem of massive blowing with radiation. The agreement of our simplified momentum equation solution in the region away from the absissa zero with the fully viscous solution of Howe and Viegas is worthy of note.

Figure 5.2 compares the current results with those of Chin (1968). As discussed in Appendix A, the current technique uses Chin's concept of two inviscid layers with the added approximation of constant density in the stream function equation with the shock layer density being that at the shock and the ablation layer density being that at the wall. The tangential velocity is determined from taking the appropriate derivative of Eq. 2.30 as defined by Eq. A.8. The relations between the normal and tangential velocities are discussed in Chapter II and Appendix A. The result is

$$u/u_s = 1 - [1-2\varepsilon(1-\varepsilon)]\,\frac{z}{R_N} \qquad 5.1$$

for the shock layer and

$$u/u_s = \left(\frac{2\rho_\infty U_\infty^2}{\rho_w V_w^2}\right)^{\frac{1}{2}} \left[2\,\frac{\rho_\infty}{\rho_w}\,(1-\varepsilon)\right]^{\frac{1}{2}} \frac{y}{R_N} \qquad 5.2$$

for the ablation layer. Since both Eqs. 5.1 and 5.2 are linear in the

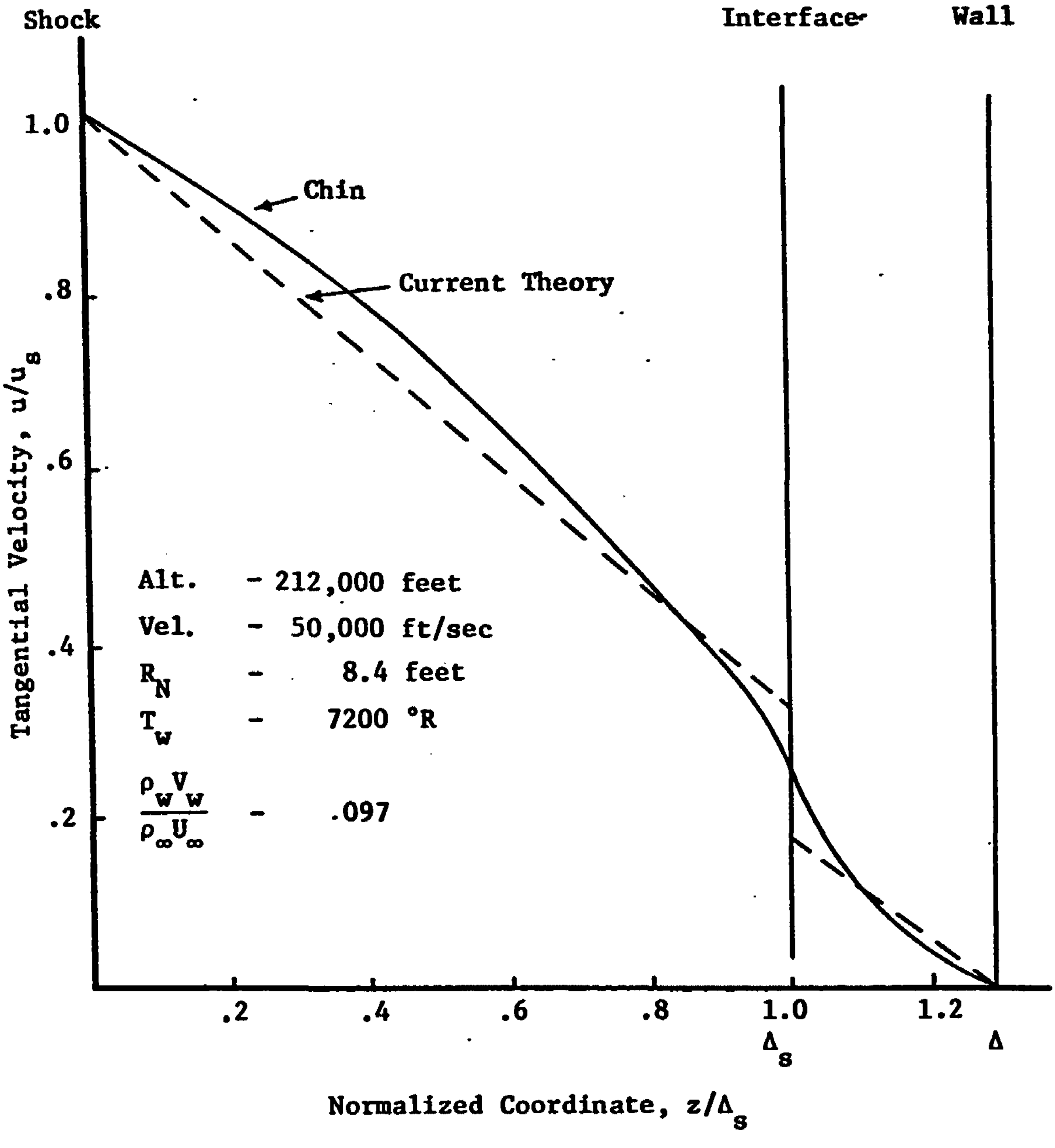

Figure 5.2 Tangential Velocity Comparison Coupled Momentum and Blowing

physical coordinate frame, the calculation necessary to produce Fig. 5.2 is the evaluation of each equation at the interface. From Eqs. 2.23 and 2.26 we have at the interface

$$z_i = \frac{\varepsilon R_N}{1 + [2\varepsilon(1-\varepsilon)]^{\frac{1}{2}}}$$

and

$$y_i = R_N\left(\frac{\rho_w V_w^2}{2\rho_\infty U_\infty^2}\right)^{\frac{1}{2}}$$

which yield

$$(u/u_s)^{\text{shock side}}_{\text{interface}} = [2\varepsilon(1-\varepsilon)]^{\frac{1}{2}} \qquad 5.3$$

for the shock layer and

$$(u/u_s)^{\text{wall side}}_{\text{interface}} = [2\,\frac{\rho_\infty}{\rho_w}\,(1-\varepsilon)]^{\frac{1}{2}} \qquad 5.4$$

for the ablation layer. The interface discontinuity of the current analysis, Fig. 5.2, is due to the shock layer and ablation layer densities being different. This discontinuity in tangential velocity on the interface for massive blowing problems was previously reported by Wallace and Kemp (1969). It is easily seen from Eq. 5.4 that this velocity discontinuity would not exist if one took $\rho_w = \rho_s$. Wallace and Kemp make this additional approximation which allows comparison with solutions to the Falkner-Skan boundary-layer equation. In this limiting case they found the two inviscid-layer approximation to give excellent results for V_w/u_s as low as 5 $Re^{-\frac{1}{2}}$ where

$$Re = \frac{u_s \ell}{\nu} \ .$$

For the specified reference conditions, if one takes ℓ as R_N and evaluates the viscosity at the shock, $Re^{-\frac{1}{2}} = 8.1 \times 10^{-3}$. At the condition of minimum wall mass flux of the current analysis and with the approximation that $\rho_w = \rho_s$ which is imposed by Wallace and Kemp, $(V_w/u_s)_{min} = 12\ Re^{-\frac{1}{2}}$. This comparison adds to the validity of the two inviscid-layer approximation in the regime of the current analysis.

Before leaving Fig. 5.2 it is of interest to note that in order to obtain velocity profiles, it was necessary for Chin to solve both the shock and ablation layer momentum equations for each iteration of the energy equation. In the current analysis, the shock momentum equation is solved only once for a given set of reference conditions and the ablation layer momentum equation is solved once for each calculated or assumed wall mass flux. In some of the present calculations with large enhancement of the ablation absorption coefficient, over 3000 iterations of the energy equation were required for convergence, but using the fixed wall mass flux technique only three to five mass flux changes were required. With the current analysis technique, this 3000 iteration problem required only five to seven evaluations of the momentum equations. The same problem using Chin's technique would require over 6000 complete integrations of the momentum equations in addition to the iterative solutions of the energy equation. With computer time requirements in mind, the small errors imposed by the approximate solution to the momentum equation seem justified. The tangential velocity has been discussed here for comparisons with other results, but the normal velocity given by Eq. 2.30 is the variable actually used in the energy equation solution. The comparison of Eq. 2.30 with other theories is discussed in Chapter II and agreement is found to be quite good.

Before leaving the momentum function discussion, it should be pointed-out that in obtaining Eq. A.16, we assumed

$$\frac{\rho_w V_w^2}{\rho_\infty U_\infty^2} \ll 1. \qquad 5.5$$

For the most severe blowing case of this study (zero absorption enhancement with the nongrey absorption coefficient), we determined

$$\frac{\rho_w V_w^2}{\rho_\infty U_\infty^2} = 2.3\text{x}10^{-3}$$

which justifies the approximation. Inequality 5.5 sets an upper limit on the blowing rate that can be treated by the current theory. The lower limit is established by the-boundary layer blowing limit (blowing rate at which the boundary layer is blown away from the surface). If the blowing rate falls below this lower limit, the assumption of an inviscid inner layer breaks down. Cole and Aroesty (1968) discuss theoretically the validity range of inviscid inner layers and Stewartson (1964) gives theoretical evidence that a laminar boundary layer blows off a flat plate when

$$\frac{\rho_w V_w}{\rho_e U_e} \geq Re^{-1/2} \qquad 5.6$$

where

$$Re = \frac{U_e x}{\nu_e}$$

and the subscript e refers to conditions at the edge of the boundary layer. If we extend this criterion to blunt body stagnation-point boundary layers we have

$$Re_s = \frac{U_s R_N}{\nu_s}$$

which for the reference conditions gives from Eq. 5.6

$$\frac{\rho_w V_w}{\rho_\infty U_\infty} \geq 8.1 \times 10^{-3}. \qquad 5.7$$

For the case of minimum wall mass flux of the current analysis

$$\frac{\rho_w V_w}{\rho_\infty U_\infty} = 9.75 \times 10^{-2}$$

and we are well into the massive blowing regime. With Inequality 5.6 as the lower limit on massive blowing, we can combine the two limits to yield

$$\frac{U_\infty}{V_w} >> \frac{\rho_w V_w}{\rho_\infty U_\infty} \geq (Re_s)^{-\frac{1}{2}} \equiv \left(\frac{\mu_s}{\rho_\infty U_\infty R_N}\right)^{\frac{1}{2}} \qquad 5.8$$

which defines the complete regime of the current theory.

In order to compare the current results for heat flux with other analyses we have chosen to use part of Wilson's compilation of data (Wilson, 1970, Fig. 11). Because of the different nose radii considered, the current data and Chin's data (Chin, 1968) incorporate radiative flux scaling by

$$q^r \sim R_N^{.25}$$

(Wilson, 1970). All data presented in Fig. 5.3 other than the current analysis are a result of continuum plus line calculations. Both the Wilson and Chin absorption coefficients are fairly detailed with the Chin model incorporating 9 continuum bands and 21 line groups. The Page model has only 2 continuum bands and 2 line groups but as can be seen from Fig. 5.3 and is shown in more detail in Page et al. (1968) these results are in good agreement with those of much more detailed absorption coefficient analyses. The two step model of the current analysis, as is discussed in Appendix B, is composed of the two continuum bands of the Page model. The point on Fig. 5.3 marked "TWO STEP x 1.25" is the two step model results of the current analysis increased by 25%. This is the factor suggested by Page to bring a continuum only result up to a continuum plus line result. The current analysis data

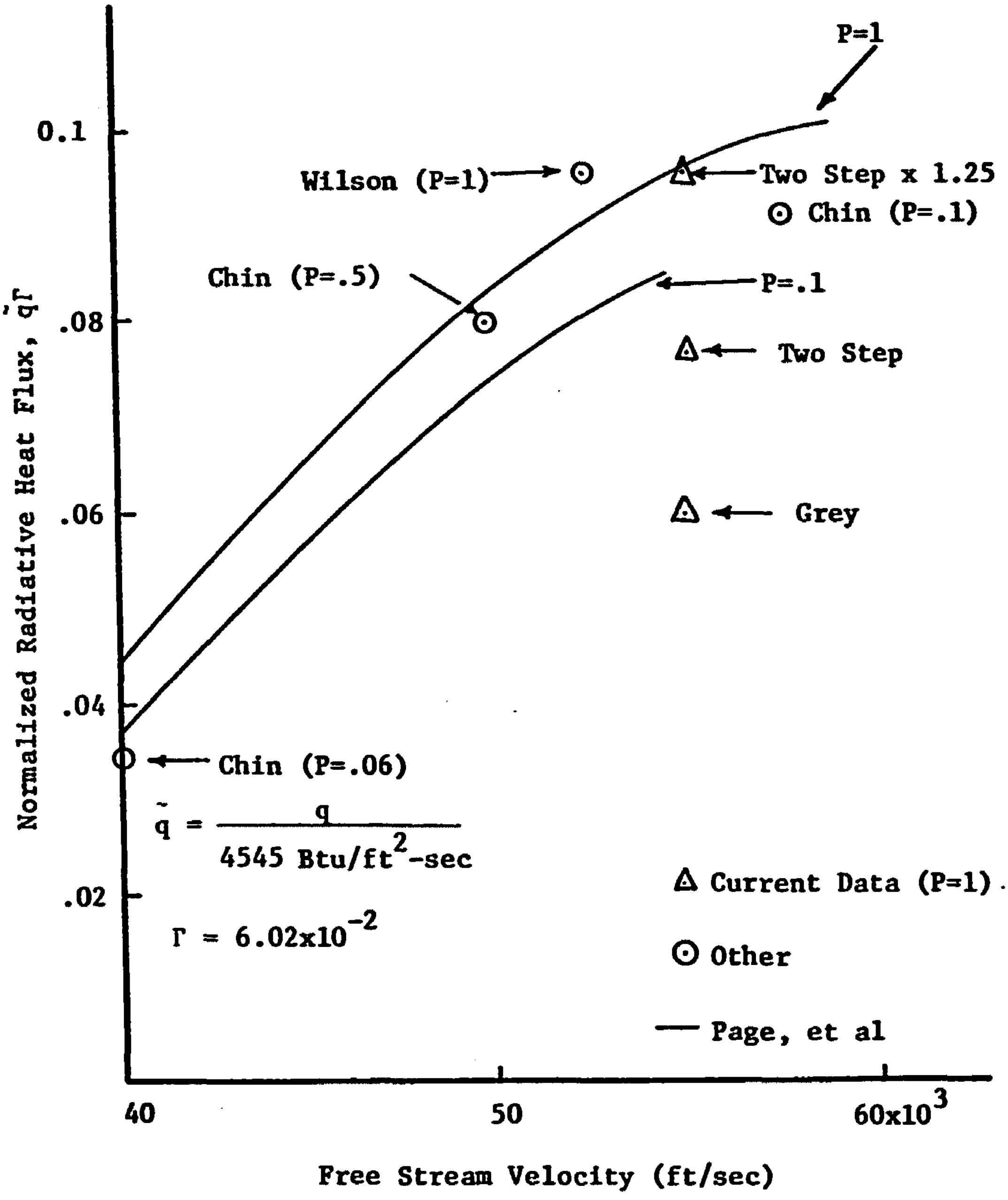

Figure 5.3 Radiative Flux Comparisons

presented in this figure are taken from the zero enhancement case. As will be discussed in the following paragraphs, with zero enhancement the radiative flux at the interface is essentially the same as at the wall. Thus for shock-layer pressures between 0.1 and 1.0 atmospheres, the blown layer does not affect the wall radiative heat flux, and our comparisons with nonblowing results are valid.

Consider now the very important results for ablation product absorption enhancement. As discussed in Appendix B, we have simulated the enhancement by increasing the temperature dependent absorption coefficient in the ablation layer only. For the grey-gas case where the absorption coefficient was taken as the Planck mean, this technique yields ablation layer enhancement over the entire frequency spectrum. Figure 5.4 shows the effect on the wall mass flux of enhancement through 2.1×10^7 and the components of the wall heat flux are given in Fig. 5.5. As is seen from Fig. 5.5, the radiative flux is the dominant mode of surface heat transfer and as will be shown, radiative mechanisms are responsible for the minimum in Fig. 5.4 which occurs at an enhancement of approximately 8×10^6. Shown in Fig. 5.6 are the optical depths at the interface, τ_{Δ_s}, and at the wall, τ_Δ. The slight increase in the wall radiative flux for enhancements through 10^4 is due to the majority of the ablation layer being optically thin in this range of enhancement. This optical thinness is shown by the τ_Δ curve in Fig. 5.6 and its effect on the wall flux might be expected by considering the energy equation for $\tau_\Delta << 1$. An approximate analysis shows

$$\text{emission} \sim \tilde{\Gamma}\, \alpha\, \tilde{T}^4$$

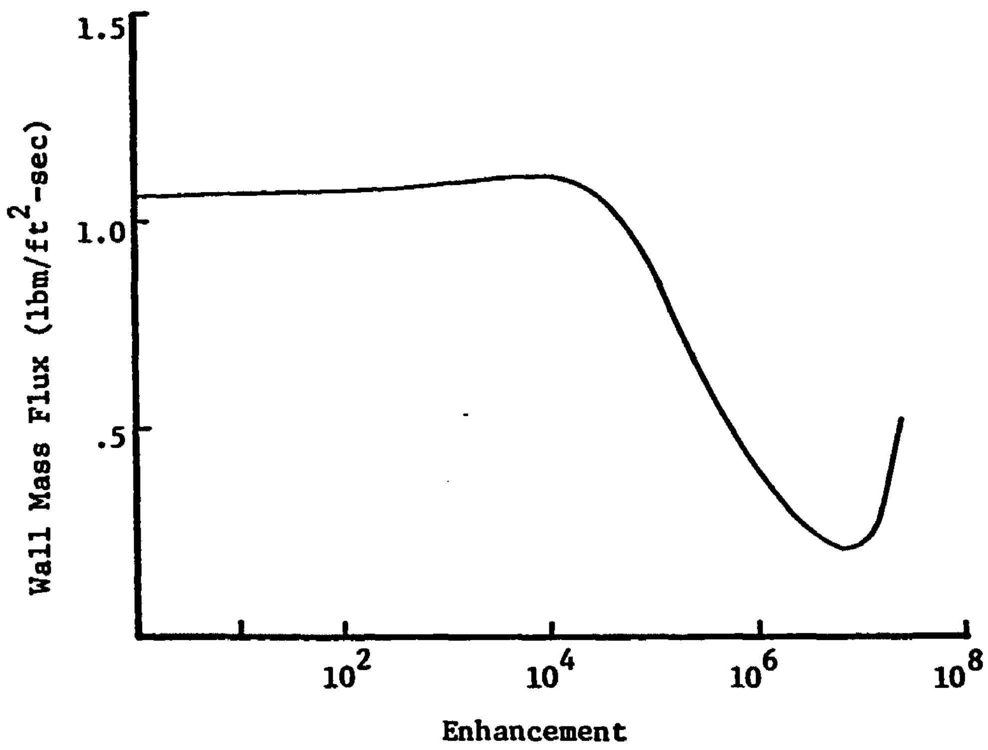

Figure 5.4 Grey-gas Absorption Coefficient Enhancement

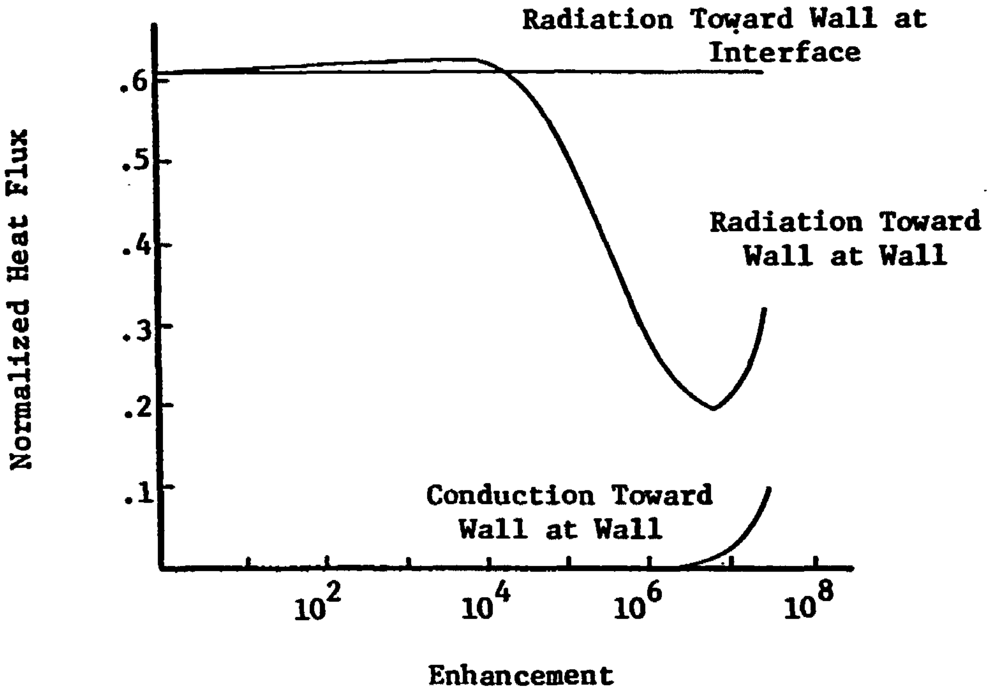

Figure 5.5 Components of the Heat Flux

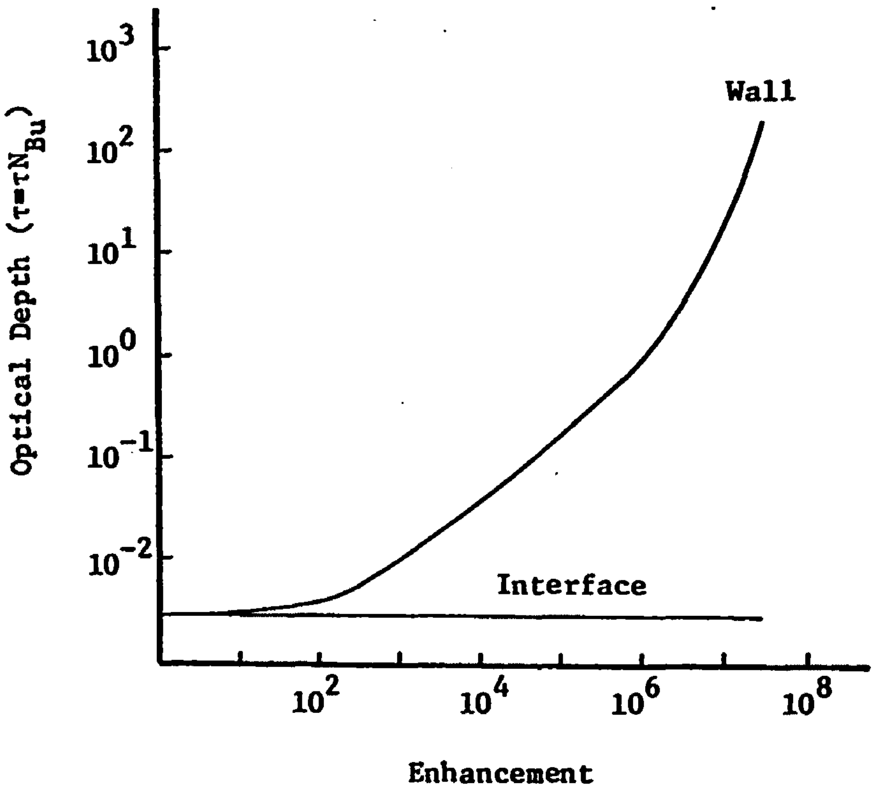

Figure 5.6 Optical Depth at Interface and Wall

while

$$\text{absorption} \sim \Gamma \, \tilde{\alpha}^2 \, \tilde{\Delta}_a \, \tilde{T}^4 \, .$$

The net result of this approximation is

$$\frac{\text{absorption}}{\text{emission}} \sim \tilde{\alpha} \, \tilde{\Delta}_a \sim \tau_\Delta - \tau_{\Delta s} \approx \tau_\Delta \qquad 5.9$$

and through an enhancement of 10^4, $\tau_\Delta < 1$ yielding an emission dominated ablation layer. Wilson (1970) observed from his calculations which use a detailed continuum model in addition to lines that there was a significant decrease in the vacuum ultraviolet continuum emission with wall mass injection. He also calculated increased wall radiative flux in the visible continuum under the same conditions. Wilson's results are consistent with the current analysis since as pointed out in Appendix B our grey absorption coefficient model is very close to the Page et al. (1968) visible continuum band. As the general rule observations of Hoshizaki and Lasher (1968) seem appropriate; "The monochromatic flux is enhanced by the presence of ablation species when the monochromatic optical depth is sufficiently small that the gas is optically thin at that frequency. Conversely, the monochromatic flux is reduced when the monochromatic optical depth is sufficiently large that the gas is highly absorbing at that frequency."

Figures 5.7 and 5.8 show the temperature and absorption coefficient profiles for enhancement parameters of 1 and 10^4 respectively. Note the approximately 2 orders of magnitude increase in

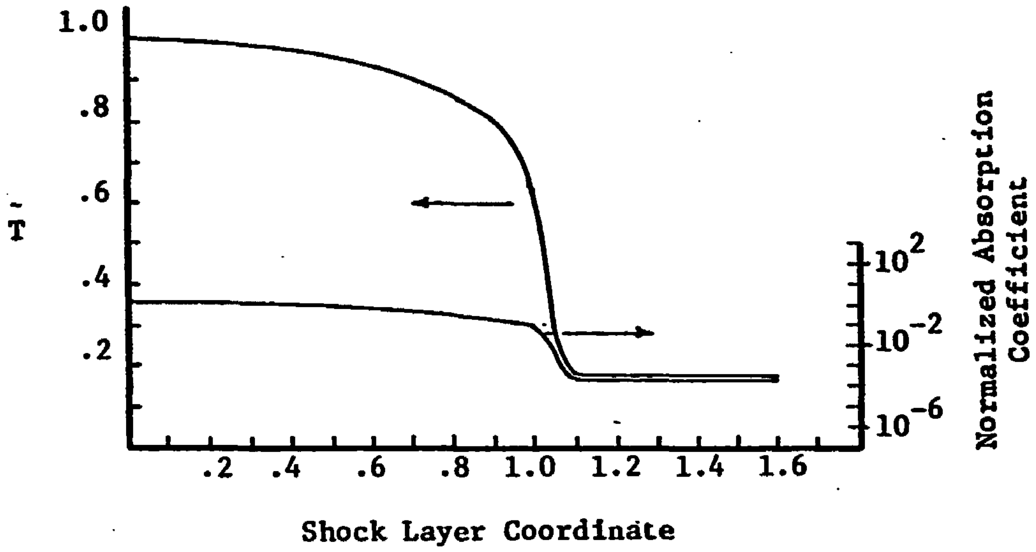

Figure 5.7 Temperature and Absorption Coefficient Profiles for Zero Enhancement

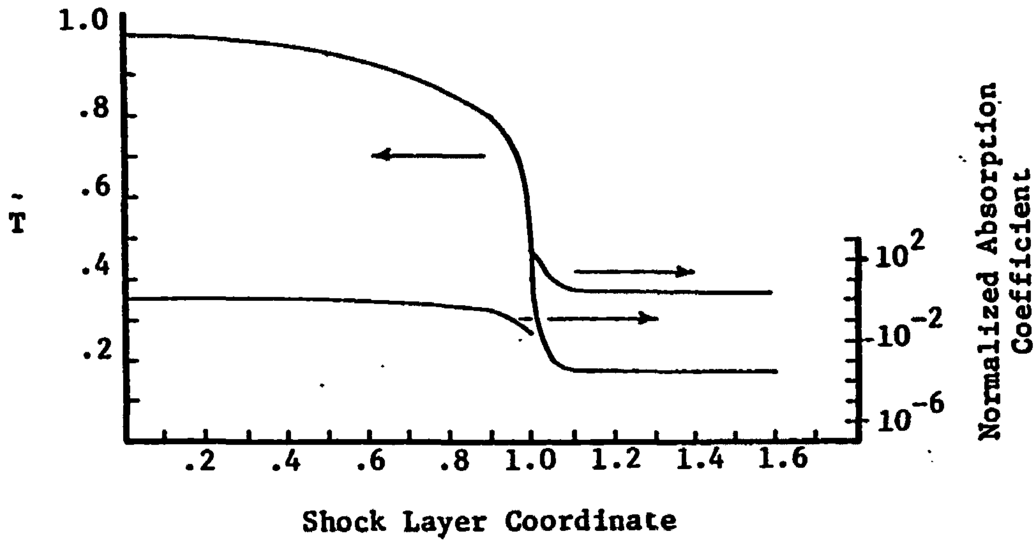

Figure 5.8 Temperature and Absorption Coefficient Profiles for 10^4 Enhancement

the ablation layer absorption coefficient over the shock layer absorption coefficient near the interface for an enhancement of 10^4. It is this small region of strongly emitting gas that is primarily responsible for the increased wall radiative flux. The approximate analysis resulting in Eq. 5.9 simply shows that the radiation emitted in the ablation layer is not absorbed in transit to the wall. To further illustrate this point and show what occurs for larger enhancements we have included Figs. 5.9 and 5.10. Figure 5.9 is a plot of the function $q_w^r(z)$ which represents the radiative flux originating between z and Δ that gets to the wall. It is given by

$$q_w^r(z) = \sum_{j=1}^{JS} \left\{ \int_{\tau_{j,\Delta}}^{\tau_j} I_j E_2[N_{Bu}(\tau_{j,\Delta} - \tau_j')]d\tau_j' \right\}. \qquad 5.10$$

The total radiative flux that reaches the wall is seen to be $q_w^r(0)$ and is the normalization used for Fig. 5.9. With this normalization, Fig. 5.9 represents at any value of z the fraction of wall radiative flux coming from the region between z and Δ. At an enhancement of 10^4, 16% of the wall flux originates in the ablation layer while at an enhancement of 1 essentially no flux originates in the ablation layer. Figure 5.10 shows the radiative flux directed toward the wall as a function of z. When the slope of this curve is positive, that region of the flow is cooling and thus adding to the flux. This is the case for the entire shock layer under the grey-gas approximation with the grey absorption coefficient taken as the Planck mean. Through an enhancement of 10^4 we can see that there is very little of any flux attenuation in the ablation layer and at 10^4 the previously discussed

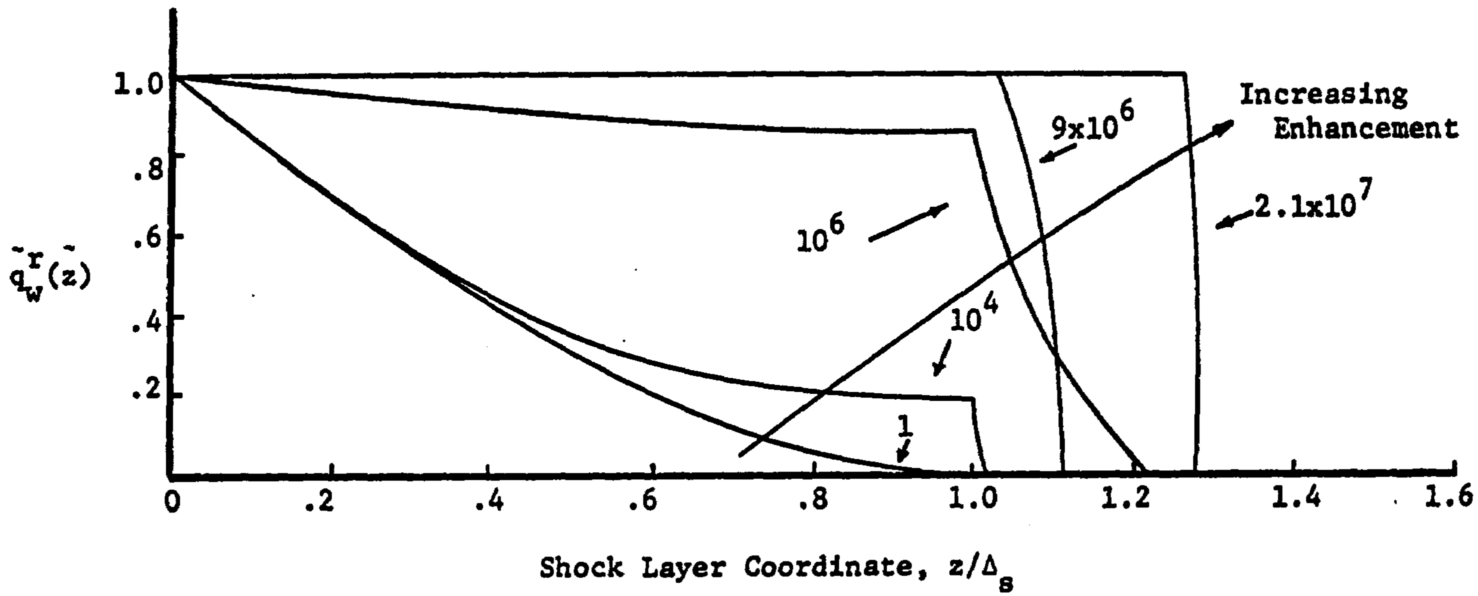

Figure 5.9 Wall Radiative Flux Source

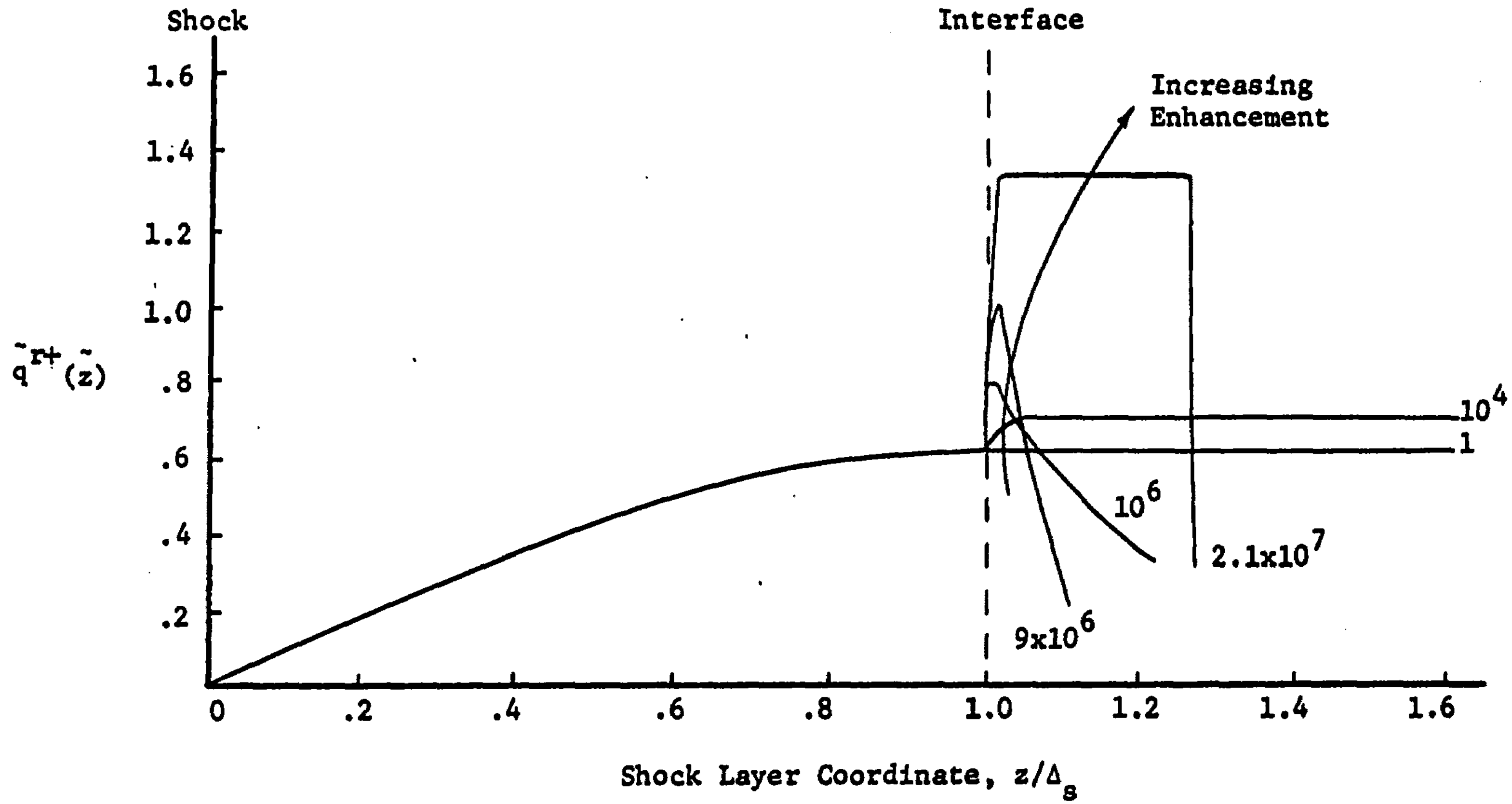

Figure 5.10 Radiative Flux Toward the Wall

emission near the interface in the ablation layer is seen to take place in the first 5% of the enhanced region. For an enhancement of 10^6 and even more pronounced at $9x10^6$ and $2.1x10^7$, the very steep positive slope just beyond the interface shows that the gas in this region is undergoing considerable radiative cooling and adding to the wall directed radiative flux. The 10^6 and $9x10^6$ curves fall off as the wall is approached thus showing that these regions of the ablation layer are highly absorbing and are attenuating the wall directed radiative flux. The large zero slope portion of the $2.1x10^7$ curve shows the region of the ablation layer that is in radiative equilibrium and the rapid decrease in the wall directed flux very near the wall is indicative of very strong attenuation in this region.

In order to examine the effects of thermal conductivity, a series of calculations were attempted with this variable set to zero. Under this condition the energy equation solution became unstable at the interface even with very small time steps. Upon examination of Eq. 3.36 we see that at the interface, where $\rho v = 0$, with zero thermal conductivity radiative equilibrium is required, i.e. dq^r/dz must go to zero, or the enthalpy profile must become infinite. Clearly the infinite slope is impossible and radiative equilibrium at a point when the remainder of the flow is in radiative nonequilibrium is extremely difficult to obtain. To overcome this difficulty, the normalized thermal conductivity was set equal to unity for all temperatures. This corresponds to the actual thermal conductivity at the wall and reduces the shock thermal conductivity by a factor of 25.76 for the reference conditions. The results of these calculations with constant thermal conductivity are shown in Fig. 5.11. By comparing these results with Fig. 5.4 we see that with small absorption enhancement the constant thermal conductivity results do not exhibit the increase in wall mass flux. This result might superficially seem contrary to the arguments given for an increased wall radiative heat flux in the $k = k(T)$ case, but upon closer examination we find that the source of the additional heat flux (the strongly emitting region in the ablation layer near the interface) is essentially eliminated in the constant conductivity case. This is seen in Figs. 5.12 and 5.13 (the temperature profiles for constant thermal conductivity and enhancement parameters of 1 and 10^4) to be due to the lack of diffusion of energy by conduction from the shock layer into the ablation layer. The temperature profiles for the $k = k(T)$ case are also included in Figs. 5.12 and 5.13 for comparison. Figure 5.14 shows the radiative flux directed toward the wall as a function of z for the case of constant thermal conductivity. In contrast to Fig. 5.10, Fig. 5.14 shows that as the ablation layer absorption coefficient is enhanced to 10^4 there is, just past the interface, only a 3.1% increase in the positive flux while for the $k = k(T)$ case at 10^4 the increase is 16.7%. Although the radiative flux at the wall for this constant thermal conductivity case is not much different from the $k = k(T)$ case, a comparison between Figs. 5.10 and 5.14 indicates a large difference in the wall directed flux interior to the ablation layer. Calculations show that at a normalized distance from the shock of 1.05 the wall directed radiative flux for the $k = k(T)$ case at an enhancement of $1.9\text{x}10^7$ is 1.51 times larger than the constant thermal conductivity

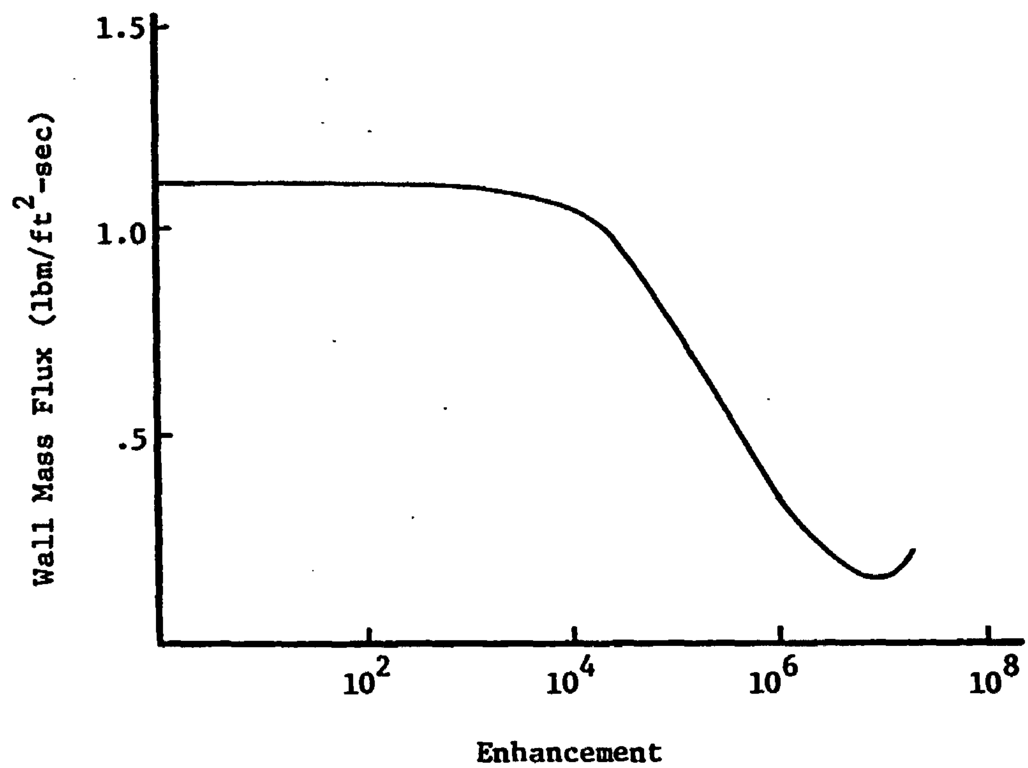

Figure 5.11 Grey-gas Absorption Coefficient Enhancement with Constant Thermal Conductivity

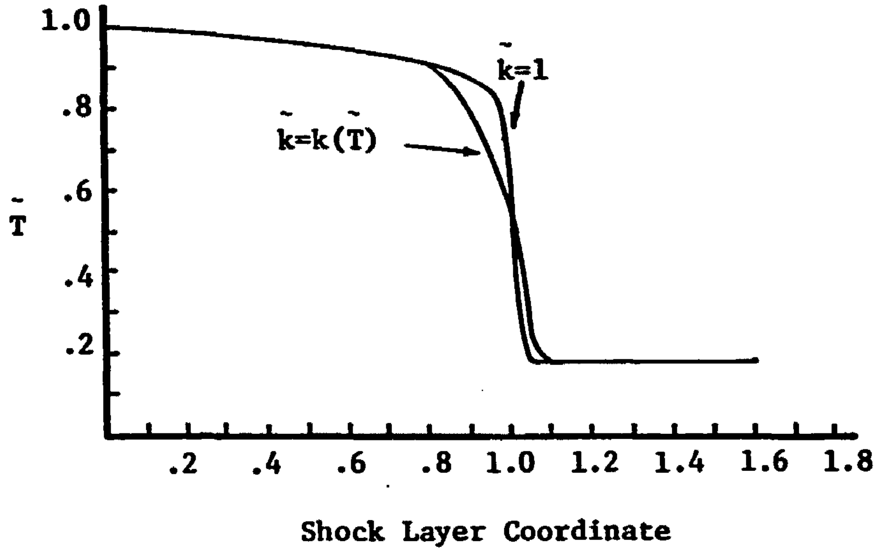

Figure 5.12 Temperature Profile for Zero Enhancement

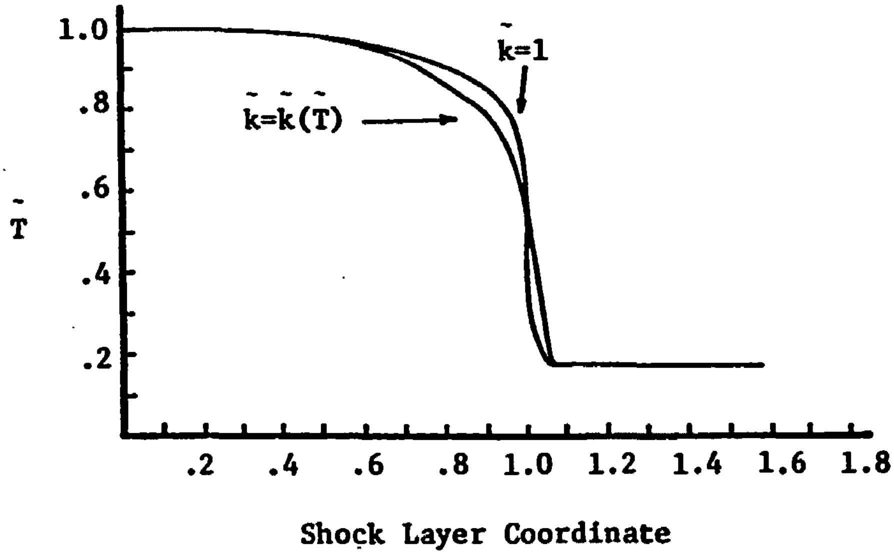

Figure 5.13 Temperature Profile for 10^4 Enhancement

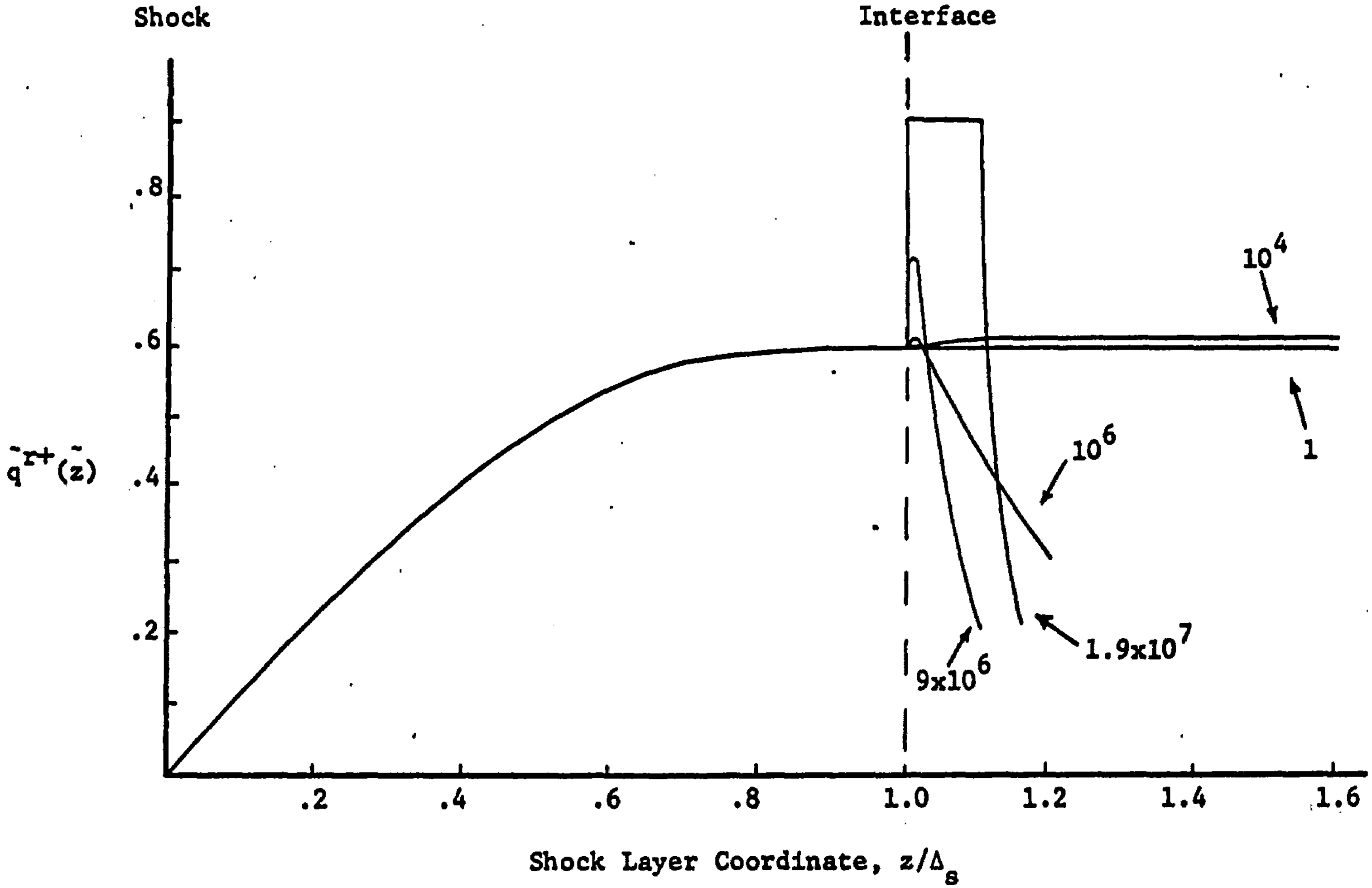

Figure 5.14 Radiative Flux Toward the Wall for Constant Thermal Conductivity

case. This is a result of reduced diffusion of energy from the shock layer to the strongly absorption enhanced ablation layer.

The approximately 5% increase in the zero enhancement wall mass flux for constant thermal conductivity in comparison with the $k = k(T)$ case is due again to the reduced diffusion of energy by thermal conduction. This is shown in Fig. 5.12 where the temperature profile for constant thermal conductivity is seen to indicate higher energy content and thus higher emitting power in the shock layer near the interface. The smearing effect of thermal conductivity was noted by Wilson (1970) when after his viscous calculations he pointed-out that viscous effects (including thermal conductivity) simply diffuse the region of steep temperature gradient near the interface over a larger spatial extent than would be calculated by inviscid theory. In the current analysis, the inclusion of actual thermal conductivity extends the high temperature region into the ablation layer where, with enhancement, the absorption coefficient is large. As can be noted a posteriori this simulates the effect of diffusing highly absorbing ablation species into the high-temperature region of the shock layer. Hoshizaki and Lasher (1968) concluded from their viscous calculations including diffusion that for mass injection comparable with the current analysis an increase in radiative flux over lower injection rates was due to the ablation products diffusing into the high-temperature region of the shock layer and reradiating towards the wall.

In the absorption enhancement regime between 10^4 and 9×10^6 the reduction in wall mass flux shown in Fig. 5.4 is due to absorption by the cooler portions of the ablation layer of radiative energy emitted by the hotter portions near the interface. Temperature profiles for this regime are given for enhancement parameters of 10^5, 10^6, $5x10^6$, and $9x10^6$ in Figs. 5.15, 5.16, 5.17, and 5.18 respectively. Through this regime the temperature profiles in the ablation layer are seen to go from isothermal at enhancement of 10^4 to one containing an inflection point at the interface for $9x10^6$ with a steep gradient near the wall. These profiles suggest almost no ablation layer absorption at 10^4 and very strong absorption for $9x10^6$ (note also the rapid drop-off of the flux curve near the wall for large enhancement as shown in Fig. 5.10). An additional point to note about this regime is shown in Fig. 5.6 where we see the ablation layer optical depth increasing from $4x10^{-2}$ at 10^4 enhancement to 13.9 at $9x10^6$ enhancement. We have now through enhancement and not by the assumption of "optically thick" produced an optically thick ablation layer. If we compare our ablation layer temperature profiles with the temperature profiles of Jischke and Baron (1969, Fig. 3) where they vary the optical depth of a one-dimensional hypersonic radiating shock layer, we see the trends as the optical depth increases are very similar. The differences in the curves near the hot boundary are due to that boundary being the region of largest convection for the hypersonic shock layer and the region of smallest convection for our ablation layer.

Let us now consider the final regime of absorption enhancement, enhancement greater than $9x10^6$. Typical ablation layer temperature profiles for enhancements of $1.5x10^7$ and $2.1x10^7$ are given in Figs. 5.19 and 5.20 respectively. The very large isothermal layer for an enhancement of $2.1x10^7$ where the ablation layer optical depth is 217.9

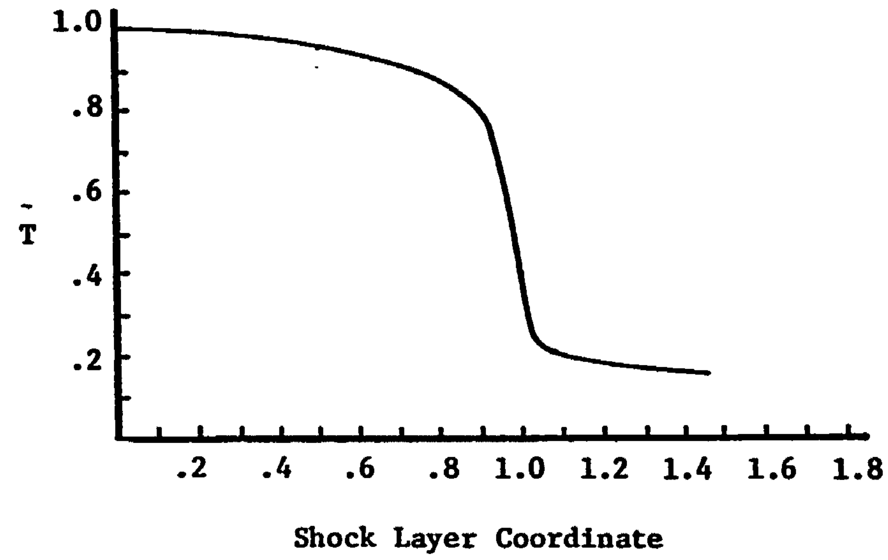

Figure 5.15 Temperature Profile for 10^5 Enhancement

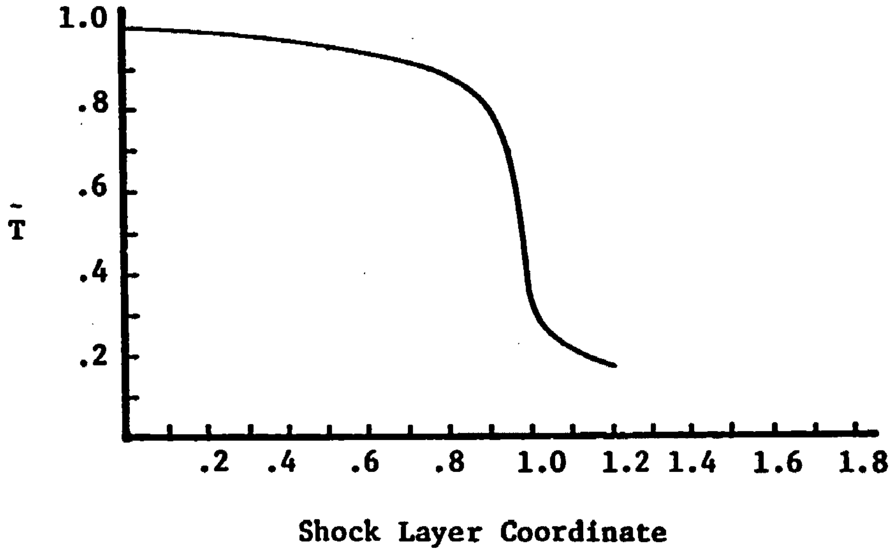

Figure 5.16 Temperature Profile for 10^6 Enhancement

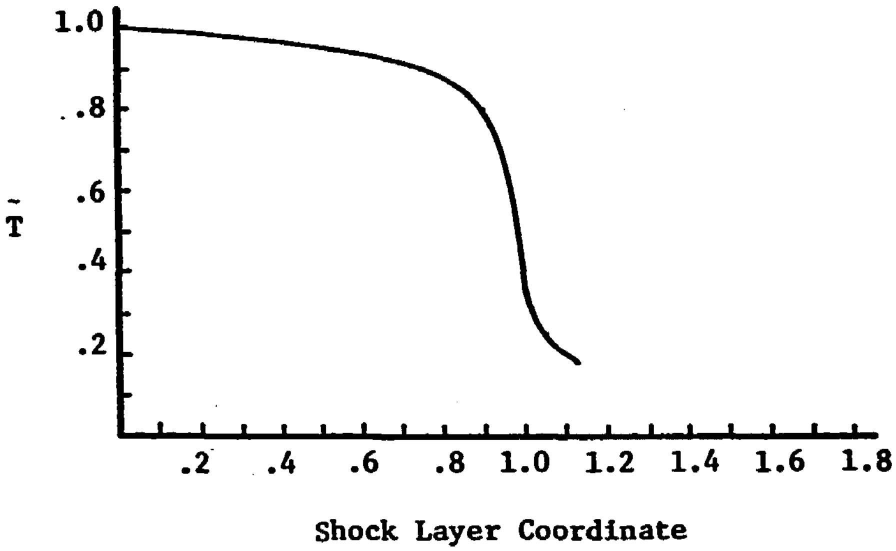

Figure 5.17 Temperature Profile for $5x10^6$ Enhancement

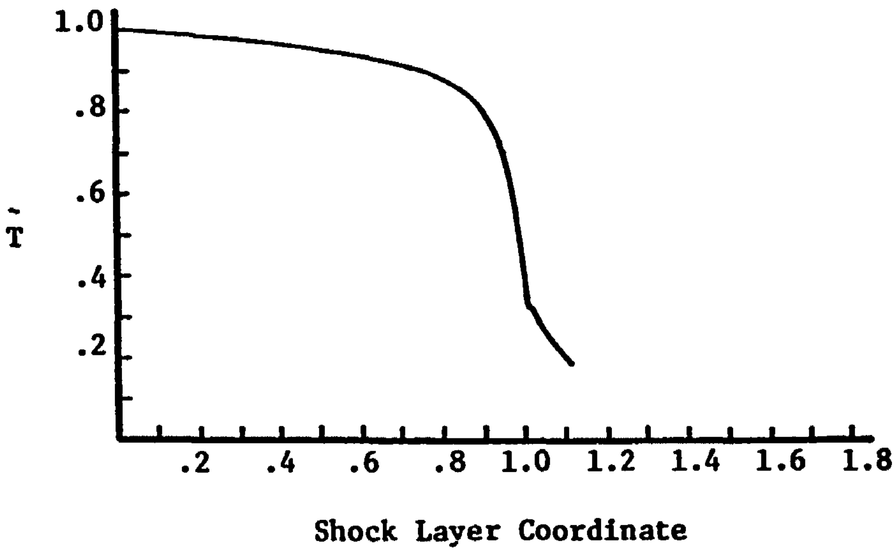

Figure 5.18 Temperature Profile for $9x10^6$ Enhancement

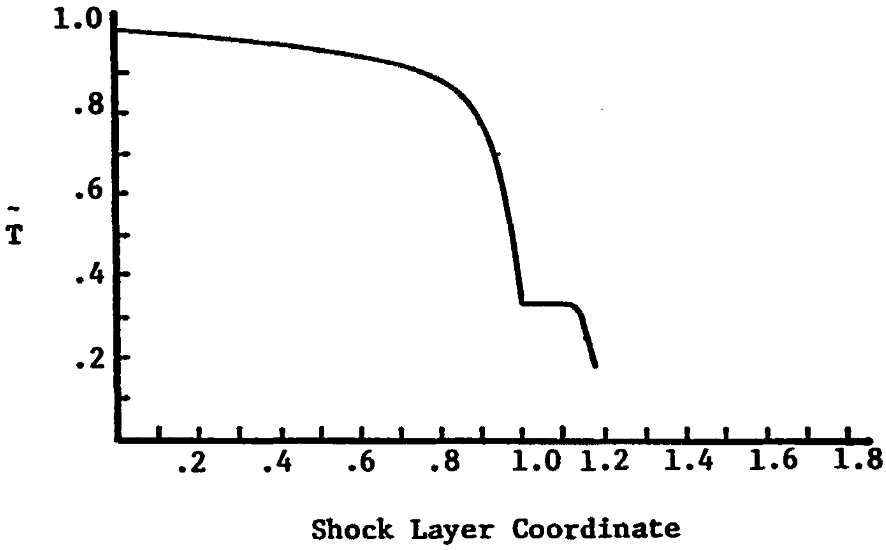

Figure 5.19 Temperature Profile for 1.5×10^7 Enhancement

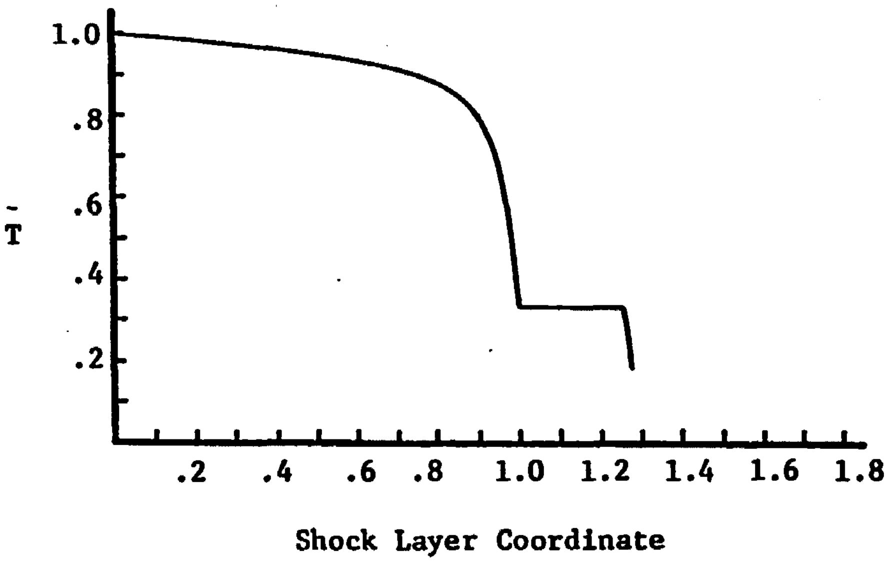

Figure 5.20 Temperature Profile for 2.1×10^7 Enhancement

is similar to the results of Yoshikawa and Chapman (1962, Fig. 11) for their limiting case of an infinite optical depth. The result of this very optically thick layer adjacent to an ablating wall with the ablation rate coupled to the wall heat flux is the previously unreported minimum in Fig. 5.4. One might expect the radiative flux to the wall and thus the wall mass flux to continue to decrease as the absorption coefficient is increased, but this clearly is not the case. The reason the wall radiative flux as shown in Fig. 5.5 starts to increase with enhancement greater than 8×10^6 is best understood through the concept of brightness temperature, $T_{\nu,br}$. Zeldovich and Raizer (1966, Vol. I, Ch. II-8) define $T_{\nu,br}$ as

$$\tilde{B}_\nu(\tilde{T}_{\nu,br}) = \int_{\tau_{\nu,\Delta}}^{\tau_\nu} \tilde{B}_\nu E_2(\tau_{\nu,\Delta} - \tau'_\nu) d\tau'_\nu \qquad 5.11$$

where $\tilde{B}_\nu$ is the Planck function normalized by $2\sigma T_s^4 N_{Bu}/\pi$ and $\tilde{T}_{\nu,br}$ is normalized by the temperature behind the shock. The brightness temperature denotes the temperature of a perfect black body emitting from its surface the same amount of spectral thermal radiation as the actual body or gas under consideration. Let us now integrate Eq. 5.11 over arbitrary frequency bands to get

$$\tilde{B}_j(\tilde{T}_{j,br}) = \int_{\tau_{j,\Delta}}^{\tau_j} \tilde{B}_j E_2(\tau_{j,\Delta} - \tau'_j) d\tau_j \qquad 5.12$$

where

$$\tilde{B}_j = \int_{\nu_{j-1}}^{\nu_j} \tilde{B}_\nu d\nu \; .$$

These frequency bands can be selected as the bands of an absorption coefficient model and one then would be able to define a brightness temperature for each band. We can now introduce a brightness temperature that corresponds to the integrated radiation flux by integrating Eq. 5.11 over the entire frequency spectrum. This yields

$$\frac{\tilde{T}^4_{br}}{2N_{Bu}} = \int_o^\infty \int_{\tau_{\nu,\Delta}}^{\tau_\nu} \tilde{B}_\nu E_2(\tau_{\nu,\Delta} - \tau_\nu')d\tau_\nu' d\nu$$

or for the step model absorption coefficient

$$\frac{T^4_{br}}{2N_{Bu}} = \sum_{j=1}^{JS} \int_{\tau_{j,\Delta}}^{\tau_j} \tilde{B}_j E_2(\tau_{j,\Delta} - \tau_j')d\tau_j' \quad . \qquad 5.13$$

Note that the right hand side of Eq. 5.13 is identical to Eq. 5.10 which is plotted in Fig. 5.9. Because the exponential integral decreases rapidly with optical depth from the wall, the main contribution to either the spectral or integrated wall flux will come from a depth into the gas of approximately one photon mean free path (i.e., at $\tau \approx 1$). Photons reaching the wall are born mainly in a layer near the wall with an optical thickness of order one. Photons born in layers farther removed from the wall are almost totally absorbed before reaching the wall. The approximately one photon mean free path layer adjacent to the wall is called the radiation layer (Zeldovich and Raizer, 1966, Vol. I, Ch II-8) and the brightness temperature is equal to some average temperature of this layer. For the current analysis, it was decided to pick an average temperature of the radiation layer by taking the gas temperature at an optical depth from the wall of $2/\pi$. This is the average distance from the wall at which a photon can be born and reach the wall and is determined from

$$\bar{\tau} = 2/\pi\int_0^{\pi/2} \mathrm{Sin}\theta d\theta \ . \tag{5.14}$$

Thus an approximate value of the brightness temperature can be taken as the gas temperature at an optical depth of $2/\pi$. The values of brightness temperature determined from the calculated temperature profiles are given in Table 5.1 along with the associated black-body radiative fluxes. For comparison the radiative flux to the wall computed from the radiative term in Eq. 3.33 or Eq. 5.10 evaluated at zero is also given. The correlation of those two heat fluxes with a maximum difference of 6% shows clearly that the brightness temperature accurately predicts the wall radiative heat flux and is a viable means of explaining the increased wall radiative heat flux for enhancement greater than 8×10^6. With this point established we can see that the temperature slope within a few photon mean free paths of the wall is becoming steeper with increased enhancement and thus increasing the average temperature of the radiative layer. This temperature increase yields photons reaching the wall that are born in a higher effective black-body temperature region and results in increased wall radiative flux. Since this is a radiative phenomena and diffusive processes, specifically conduction to the wall, are at least an order of magnitude less, it was not surprising to find that the brightness temperature concept correlated the constant thermal conductivity as well as the

Table 5.1 Comparison of Wall Radiative Heat Flux Determined by Brightness Temperature and by Radiative Flux Integral

ENHANCED FACTOR	OPTICAL DEPTH		NORMALIZED BRIGHTNESS TEMPERATURE	NORMALIZED WALL RADIATIVE HEAT FLUX	
	SHOCK-INTERFACE	SHOCK-WALL		BY BRIGHTNESS TEMPERATURE	BY DETAILED INTEGRAL
1	4.20×10^{-3}	4.21×10^{-3}			
10	4.20×10^{-3}	4.21×10^{-3}			
10^2	4.19×10^{-3}	5.00×10^{-3}			
10^4	4.18×10^{-3}	4.04×10^{-2}			
10^5	4.17×10^{-3}	2.25×10^{-1}			
10^6	4.15×10^{-3}	1.61	.235	.264	.281
9×10^6	4.15×10^{-3}	1.39×10^1	.209	.167	.172
1.5×10^7	4.15×10^{-3}	7.68×10^1	.222	.251	.230
2.1×10^7	4.15×10^{-3}	2.18×10^2	.240	.290	.275

$k = k(T)$ data of Table 5.1.

Many investigators (see for example; Wilson, 1970, Hoshizaki and Lasher, 1968; Chapman, 1967; Howe and Viegas, 1963; and Howe, 1961) have considered the effects on wall heat flux of varying either ablation product or injected gas absorption characteristics or models. In each of the examples above, the ablation or injection rate was not coupled to the wall heat flux but was arbitrarily established. In order to see the effect on wall heat flux of absorption product enhancement with an arbitrarily set wall mass flux, a series of calculations were carried-out with a constant wall mass flux of 1.113 lbm/ft^2-sec. Since this flux corresponds to the calculated result for an enhancement of 10^4 only enhancements greater than 10^4 were considered. As shown in Fig. 5.21, the wall radiative flux for the constant mass flux case does not increase even at an enhancement of 2.1×10^7. Also shown in the Figure is the wall radiative flux for the variable mass flux case. Temperature profiles for constant wall mass flux are shown for enhancements of 10^5, 10^6, 5×10^6, 9×10^6, 1.5×10^7, and 2.1×10^7 in Figs. 5.22-5.27. Comparison of these profiles with the corresponding enhancement profiles for the variable mass flux case show that up to the variable mass flux wall location the profiles are very similar. In the region beyond the variable mass flux wall location, the fixed mass flux temperature profiles are near isothermal. It is this isothermal optically thick region that absorbs photons emitted from the region of large temperature gradient and prevents the wall radiative flux from increasing even though the overall optical depth is larger for a particular enhancement than that calculated for the variable mass flux

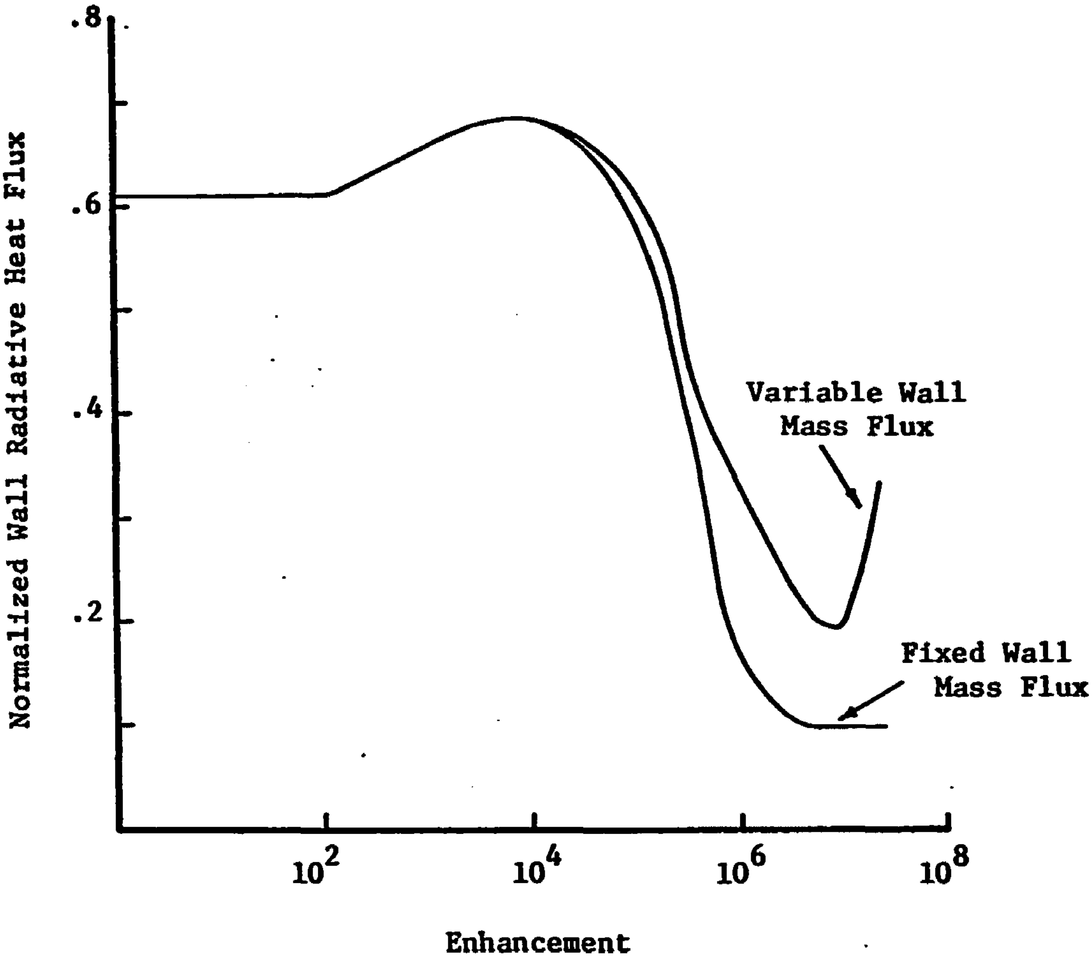

Figure 5.21 Wall Radiative Heat Flux for Grey-gas Absorption Coefficient Enhancement with Fixed and Variable Wall Mass Flux

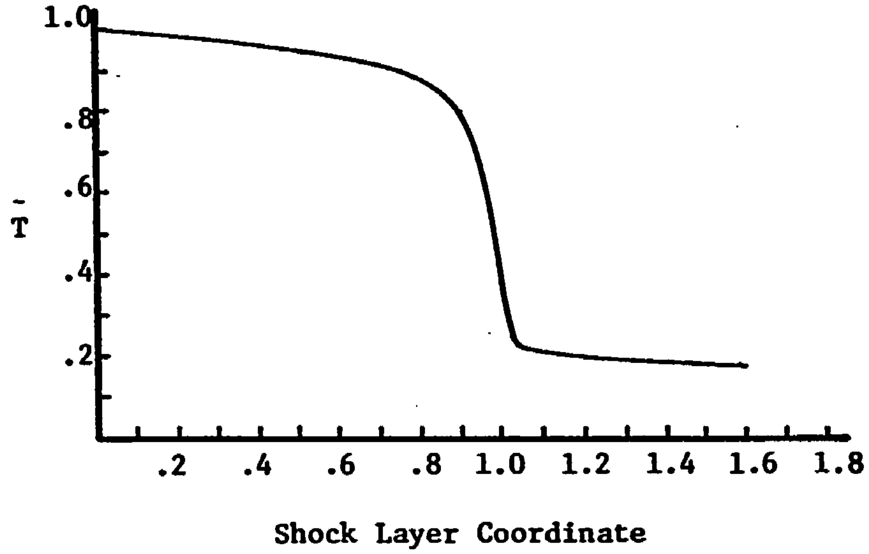

Figure 5.22 Temperature Profile for 10^5 Enhancement with Fixed Wall Mass Flux

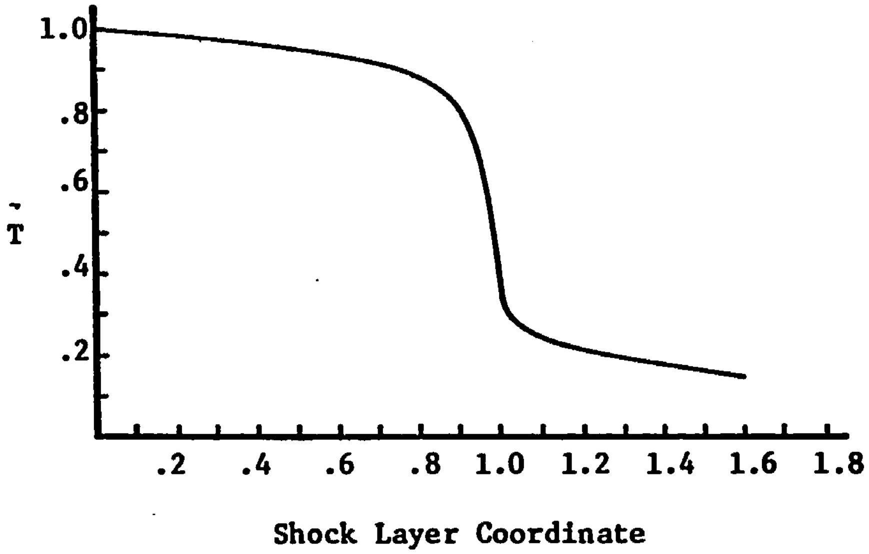

Figure 5.23 Temperature Profile for 10^6 Enhancement with Fixed Wall Mass Flux

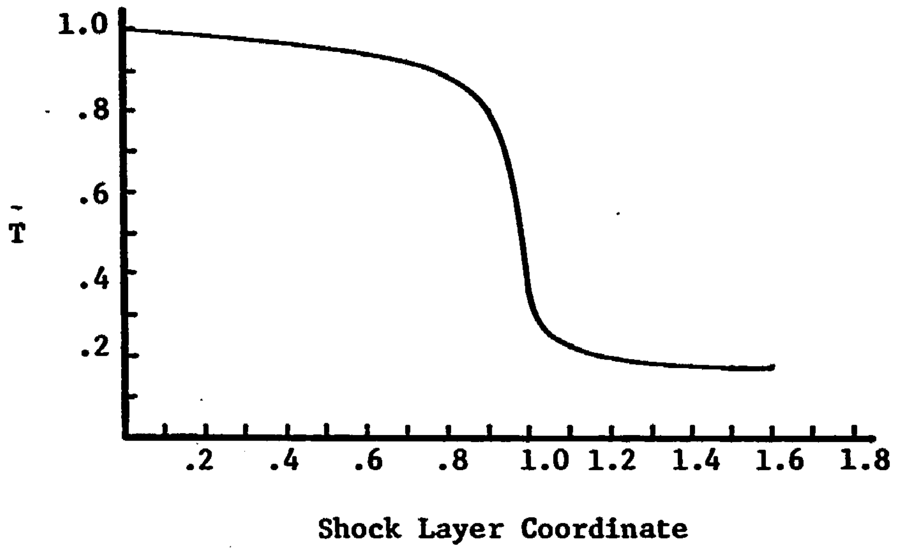

Figure 5.24 Temperature Profile for $5x10^6$ Enhancement with Fixed Wall Mass Flux

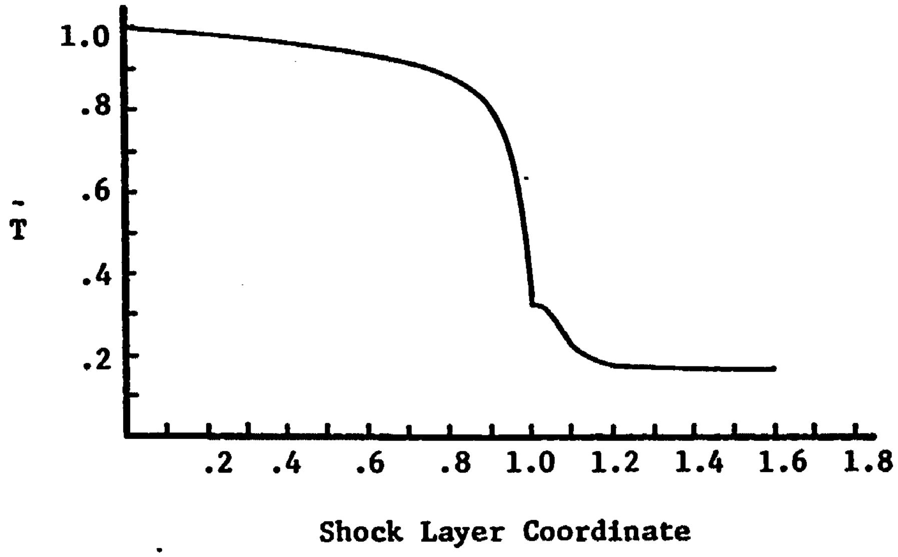

Figure 5.25 Temperature Profile for $9x10^6$ Enhancement with Fixed Wall Mass Flux

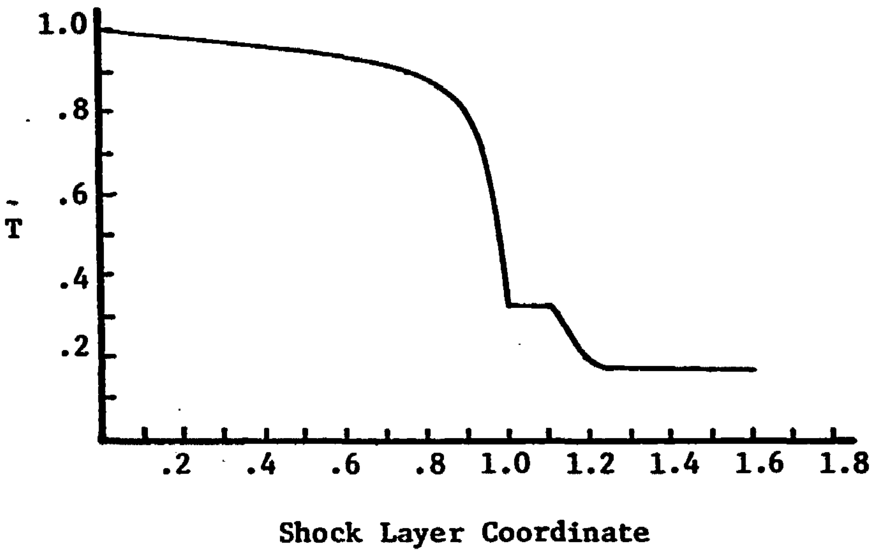

Figure 5.26 Temperature Profile for $1.5x10^7$ Enhancement with Fixed Wall Mass Flux

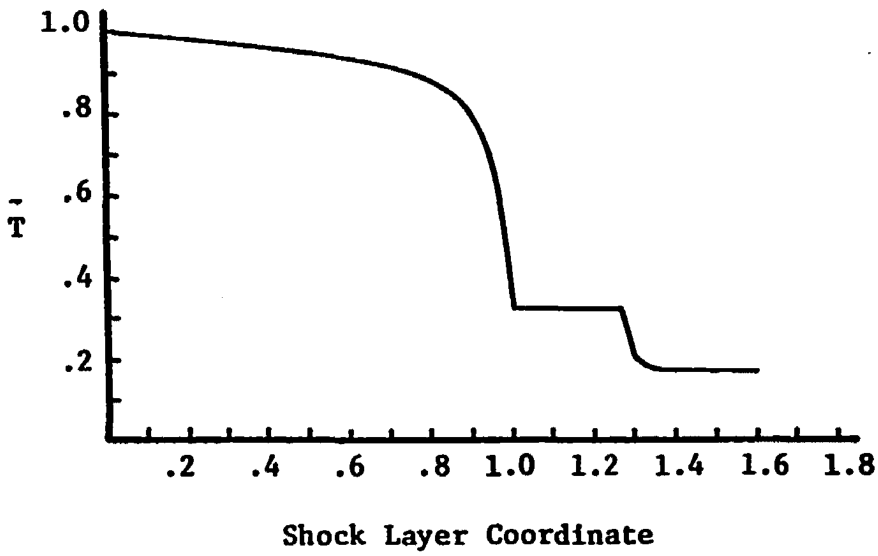

Figure 5.27 Temperature Profile for $2.1x10^7$ Enhancement with Fixed Wall Mass Flux

case. The key to understanding this phenomena is again the brightness temperature. By looking into the gas to an optical depth of approximately one, all we see is the isothermal temperature at all enhancements. The fixed mass flux ablation layer, even though optically thick, shields the wall from radiation from the hotter layer near the interface. Figures 5.25-2.27 show that as the enhancement is increased the steep temperature gradient moves closer to the wall, and it is anticipated that with additional enhancement there would be a minimum in the wall radiative flux. Additional enhancement could not be investigated with the present model because the explicit radiative flux divergence term in the energy equation requires such a small time step that computer time becomes prohibitive.

The results of these constant wall mass flux calculations indicate that extreme caution should be taken when drawing conclusions about ablation layer absorption enhancement or ablation product absorption coefficient models without coupling between wall heat flux and wall mass flux. As shown by Fig. 5.21, this coupling was the difference between a minimum in the wall radiative flux and no minimum. Even though enhancements of the order of 10^7 are only academic, it will be shown in the discussion of a more detailed absorption coefficient model that a minimum in the wall heat flux can occur at more practical degrees of enhancement. With this in mind consider an ablator-material design based on wall mass loss decreasing with increased enhancement as is the case for enhancements between 10^4 and $8x10^6$. Our results show the constant wall mass flux analysis may be misleading. If the new ablator material were enhanced to the order of 10^8, the variable wall mass flux analysis shows that the ablator would not be very effective although the constant wall mass flux analysis shows no upper limit for the beneficial effect of enhancement.

In addition to the parametric studies of ablation product absorption coefficient enhancement, the grey-gas model was also used for two additional analyses. The first analysis considered, for the reference conditions and no enhancement, the effect on wall mass flux of increasing the effective heat of ablation. From Eq. 3.23 we see that this increase will reduce the wall mass flux for fixed heat flux. However after finding that enhancement of the ablation absorption coefficient was only effective to a degree and then was detrimental in reducing the wall mass flux, it seemed necessary to examine the increased effective heat of ablation case. As Fig. 5.28 shows, the wall mass flux decreases monotomically through the limit of massive blowing which for the reference conditions occurs at a wall mass flux of 1.25×10^{-2} lbm/ft^2-sec. The wall mass flux drops to this limiting value at an effective heat of ablation of approximately 3×10^5 Btu/lbm; therefore, Fig. 5.28 beyond this limit is suspect. If this region were of interest, a boundary-layer analysis would be required. The current analysis did show that the wall conductive flux increased from the order of 10^{-5} at the reference effective heat of ablation to approximately .6 and equal to the wall radiative flux at the massive blowing limit. Prior to making the calculations it was anticipated that as the ablation layer got smaller with increased effective heat of ablation the conduction might become large and cause a minimum, but as shown in Fig. 5.28 the wall mass flux went like the effective heat

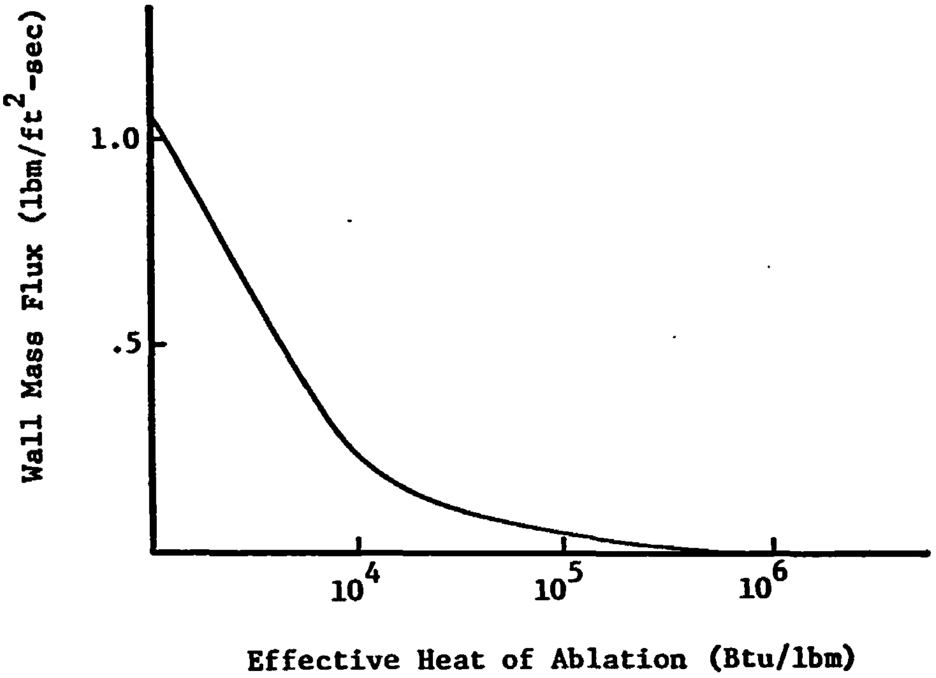

Figure 5.28 Effect of Increasing Effective Heat of Ablation

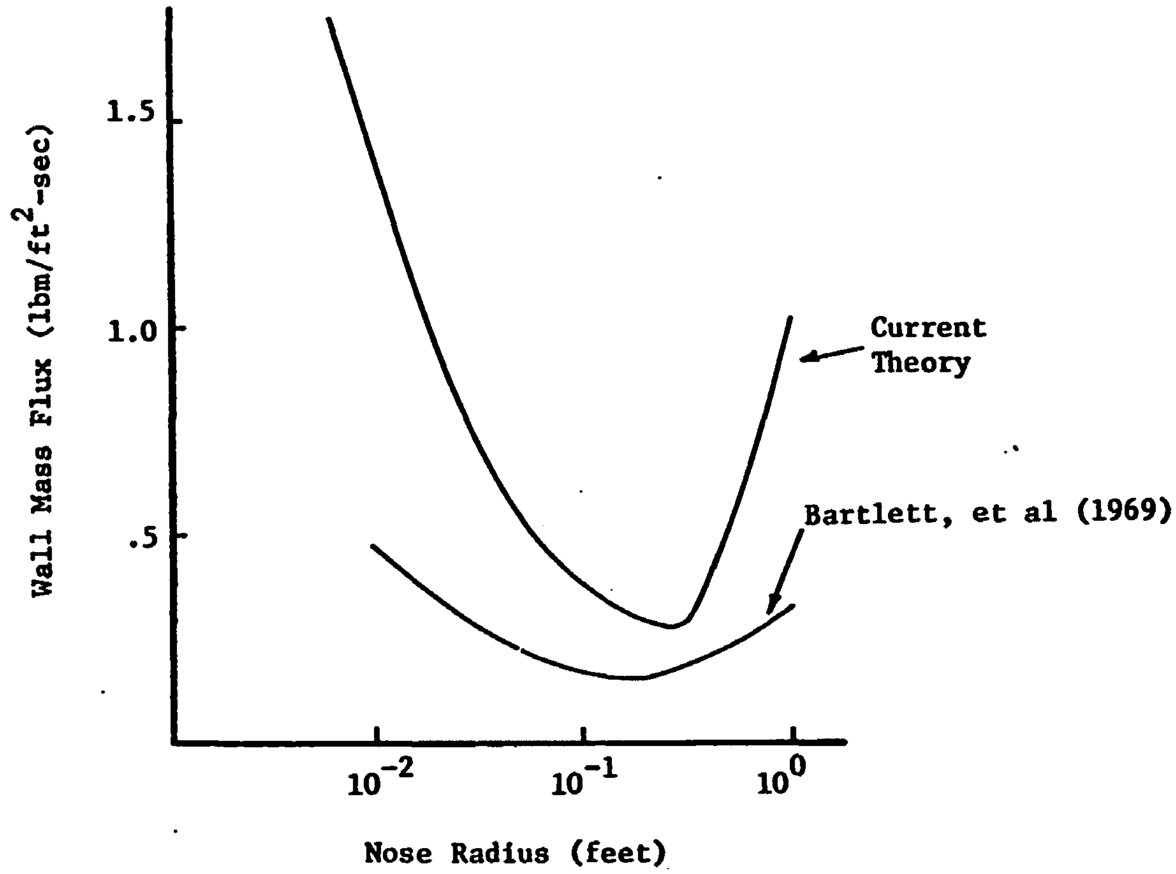

Figure 5.29 Effect of Varying Nose Radius

of ablation rather than the wall conductive flux.

The second additional analysis, again for the reference conditions and no enhancement, considered the effect on wall mass flux of small nose radii. As can be seen from Fig. 5.29 a minimum in the wall mass flux is reached at a nose radius of approximately .25 feet. For comparison, the results of Bartlett et al. (1969) for the same altitude and velocity but different material properties and solution technique are included. They used a detailed boundary-layer analysis, but superimposed the radiation. Although this solution technique will cause some differences, the major differences are due to Bartlet using for graphite an effective heat of ablation of the order of 10^4 Btu/lbm compared to our 2200 Btu/lbm and their using a wall temperature of approximately 7400°R compared to our 5400°R. Both of these differences reduce Bartlett's values of wall mass flux compared to ours, but their superimposed radiation included both lines and continuum which would tend to increase their values. Because of these major differences, it is difficult to conclude more than trend confirmation from Fig. 5.29. The current calculations, in addition to confirming the trends of Bartlett through the use of coupled-grey radiation transport, also show (see Fig. 5.30) that radiation is the dominant component of the wall heat flux for larger nose radii while conduction is dominant for the smaller nose radii. To assure these small nose radii cases were still in the massive blowing regime, checks were made using the criterion of Eq. 5.8. It was determined that the wall mass flux was always at least one order of magnitude above the blow-off value.

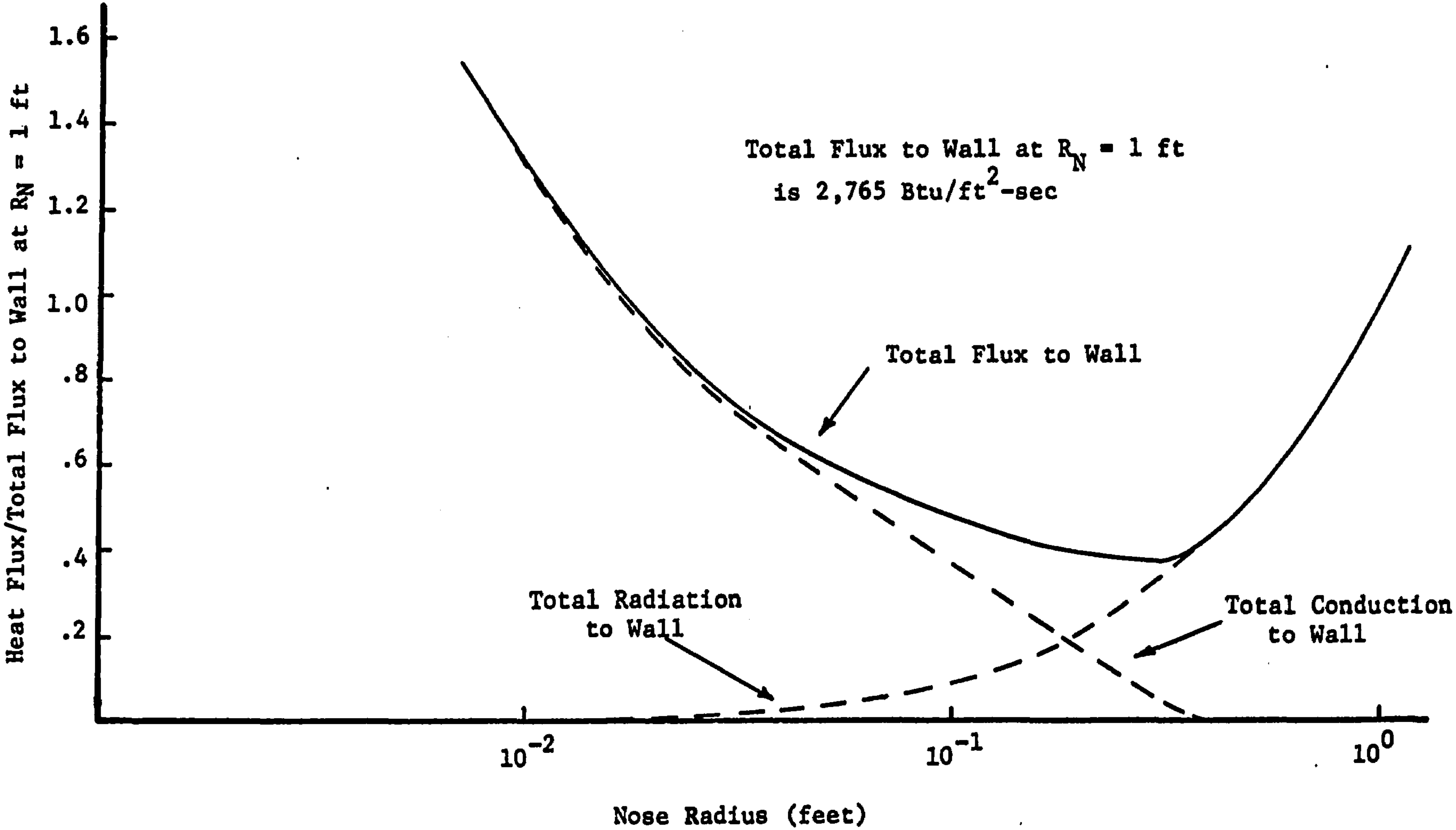

Figure 5.30 Wall Heat Flux for Varying Nose Radius

The wall mass flux results for the two-step continuum model are shown in Fig. 5.31. In obtaining these data, both the visible and vacuum ultraviolet absorption coefficients were enhanced equally by a multiplicative factor. In order to understand the first minimum (note Fig. 5.31 at an enhancement of 100) we can observe the behavior of the spectral heat fluxes as shown in Fig. 5.32. The wall flux in the vacuum ultraviolet decreases rapidly because the ablation layer optical depth in this spectral band exceeds unity with an enhancement of only 30. The optical depths for both spectral bands are shown in Fig. 5.33. As was seen in the grey-gas analysis, the wall flux started to decrease for enhancements greater than 10^4 which corresponded to an overall optical depth of approximately 4×10^{-2}. The optical depth for the vacuum ultraviolet with no enhancement is .395, therefore, the decrease in wall heat flux for this spectral band with enhancement can be expected. The increase in wall heat flux for the visible band is again expected from the grey-gas results where for enhancements up to 10^4 the wall heat flux increased. As in the grey-gas case the ablation layer optical depth is much less than unity and we have an emission dominated ablation layer in the visible band. The reason the visible component of the wall heat flux increases more rapidly than the grey-gas case and more than doubles the no enhancement value with an enhancement of 10^3 is that all the vacuum ultraviolet shock layer energy that reaches the interface is absorbed and greatly increases the temperature at the interface. This is easily seen from Fig. 5.32 where at enhancements greater than 100 essentially none of the vacuum ultraviolet heat flux that strikes the interface (the vacuum

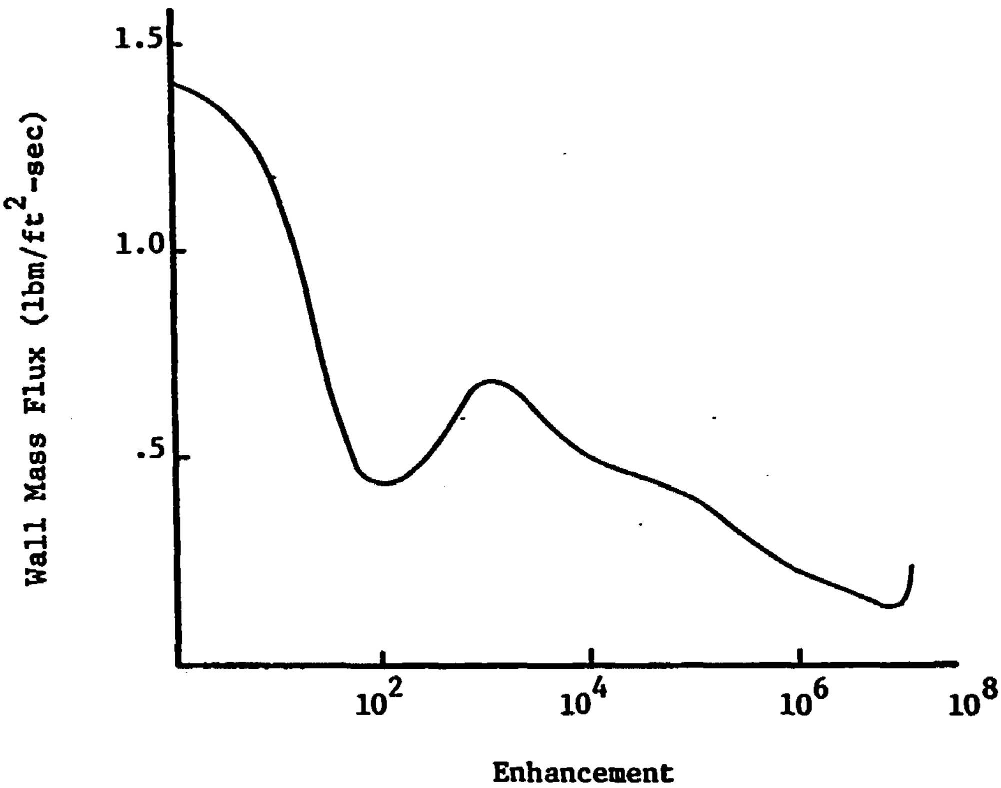

Figure 5.31 Two Energy Group Absorption Coefficient Enhancement

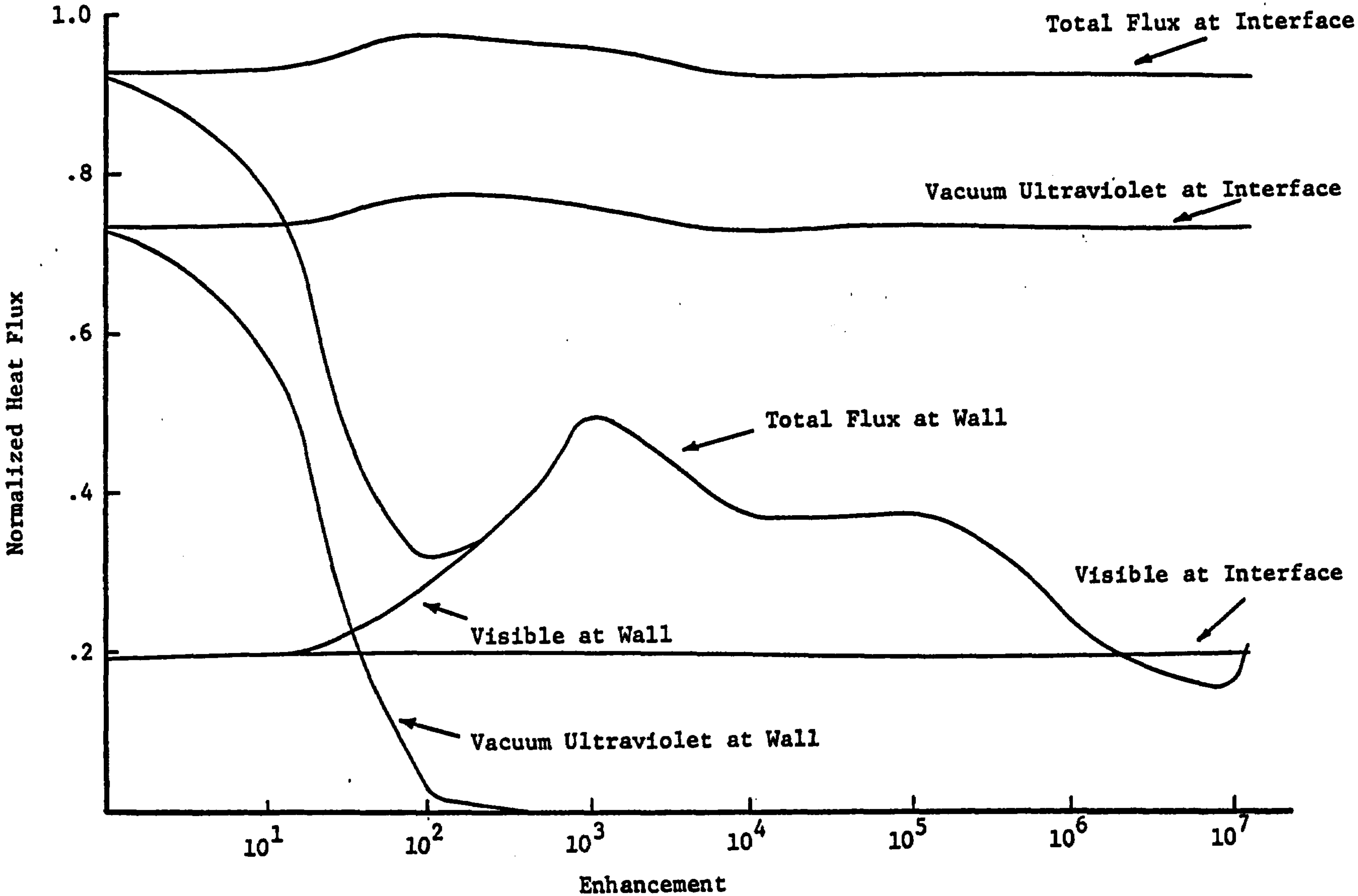

Figure 5.32 Spectral Radiative Flux Toward the Wall

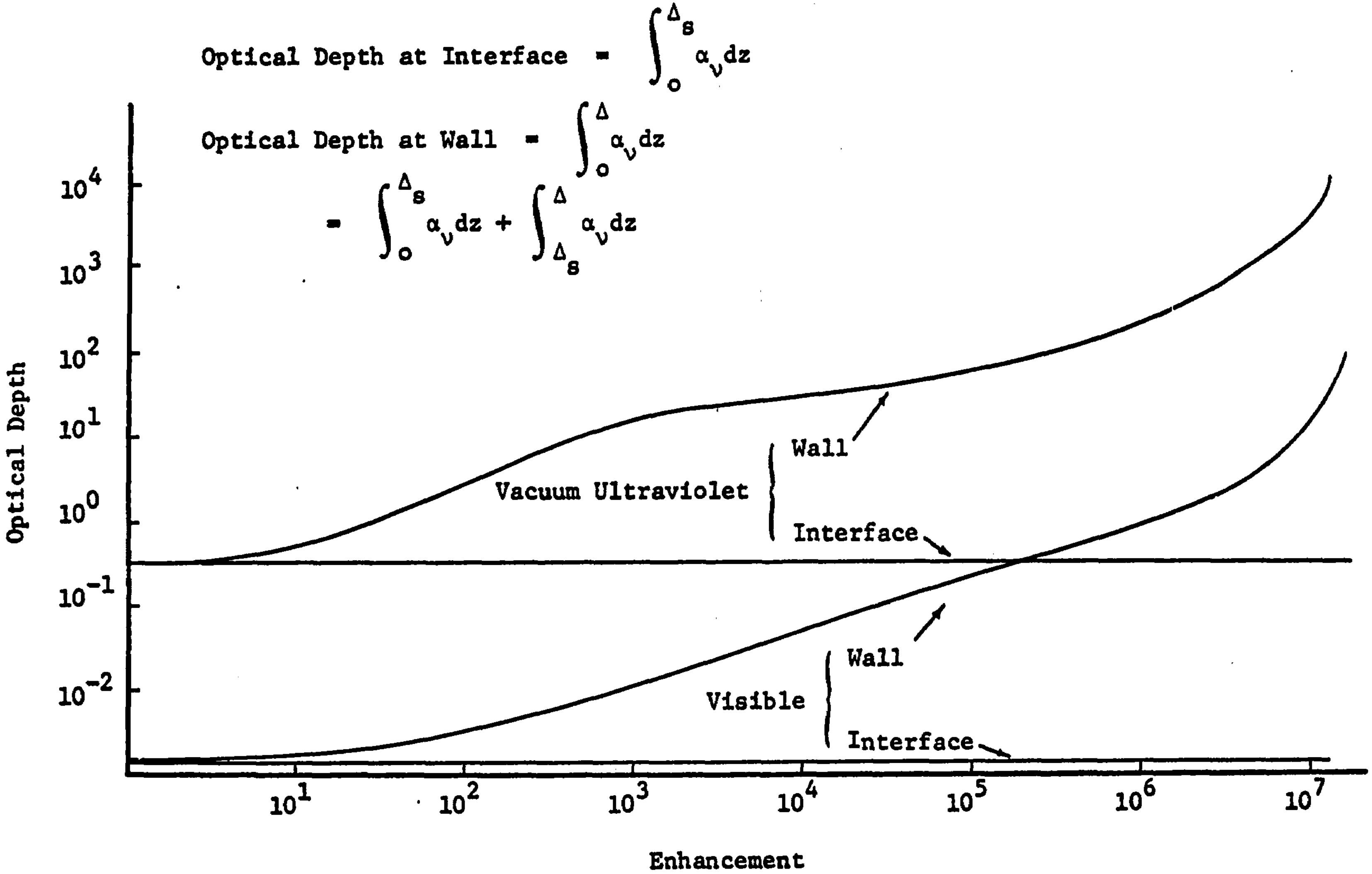

Figure 5.33 Spectral Optical Depths

ultraviolet heat flux at the interface is approximately 80% of the total) reaches the wall.

At an enhancement of 10^3 we can see from Fig. 5.32 that the visible wall heat flux starts to decrease. This is due to the ablation layer visible optical thickness approaching one. At an enhancement of 10^3, the optical thickness in the visible spectral band is only $1.5\text{x}10^{-2}$, but as shown in the grey-gas analysis an optical thickness of the order of 10^{-2} is sufficient to cause a wall heat flux reduction with additional enhancement. Between enhancements of 10^3 and $8\text{x}10^6$, the wall mass flux continues to decrease with increased enhancement. The explanation for this behavior is the same as for the grey-gas case in the enhancement regime between 10^4 and $9\text{x}10^6$. Basically it involves absorption by the cooler portions of the ablation layer of radiation emitted by the hotter portion near the interface. The second minimum in the wall mass flux curve is due to the very optically thick, in both spectral bands, gas adjacent to the wall. As in the grey-gas case, the photons that reach the wall are emitted from the hot radiation layer and as the temperature profile steepens the effective radiation layer temperature increases. Typical temperature profiles for enhancements of 1, 10, 20, 50, 10^2, 10^3, 10^4, 10^5, 10^6, $8.2\text{x}10^6$ and $1.3\text{x}10^7$ are shown in Figs. 5.34-5.44. These profiles exhibit the same trends as the grey-gas profiles.

After observing the first minimum in Fig. 5.31, it seemed necessary to investigate the effects of single band enhancement. To do this one simply applies the enhancement parameter to only the selected band. Figure 5.45 shows the results for vacuum ultraviolet

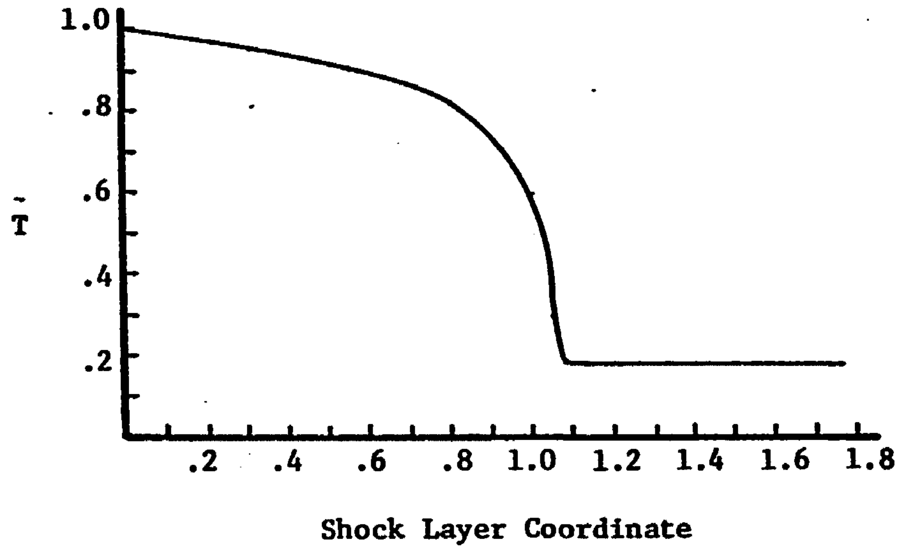

Figure 5.34 Temperature Profile for Zero Enhancement with Two Energy Group Absorption Coefficient

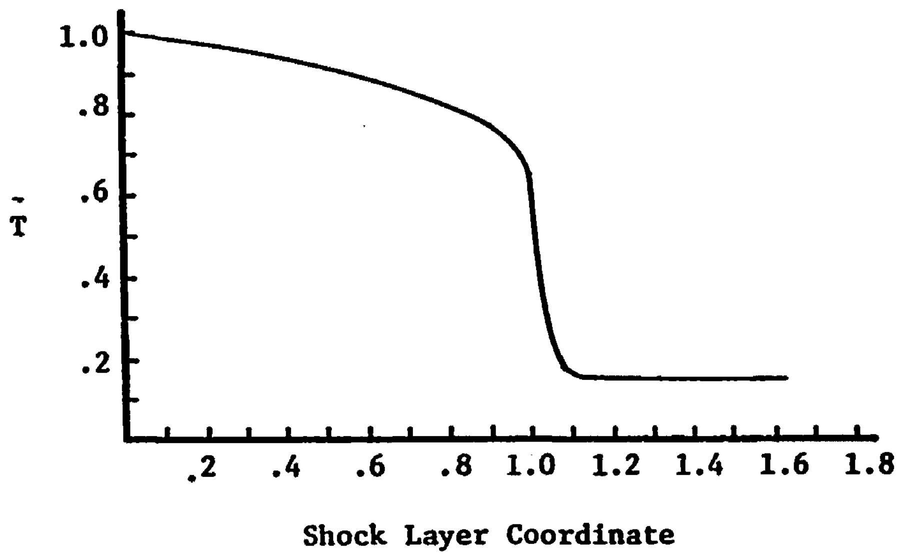

Figure 5.35 Temperature Profile for 10 Enhancement with Two Energy Group Absorption Coefficient

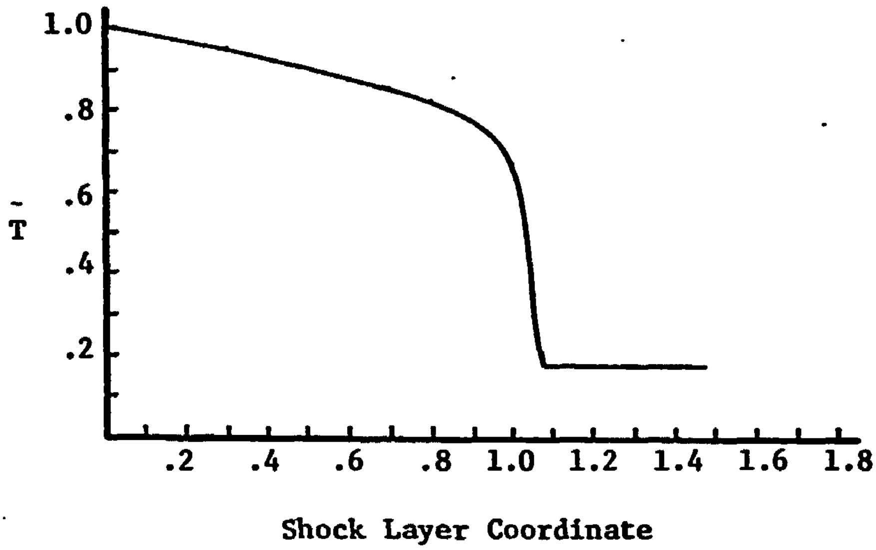

Figure 5.36 Temperature Profile for 20 Enhancement with Two Energy Group Absorption Coefficient

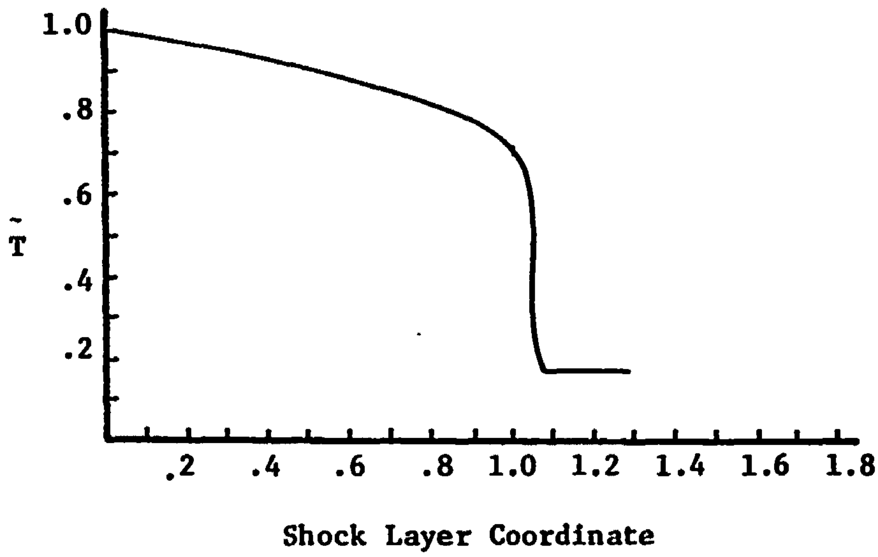

Figure 5.37 Temperature Profile for 50 Enhancement with Two Energy Group Absorption Coefficient

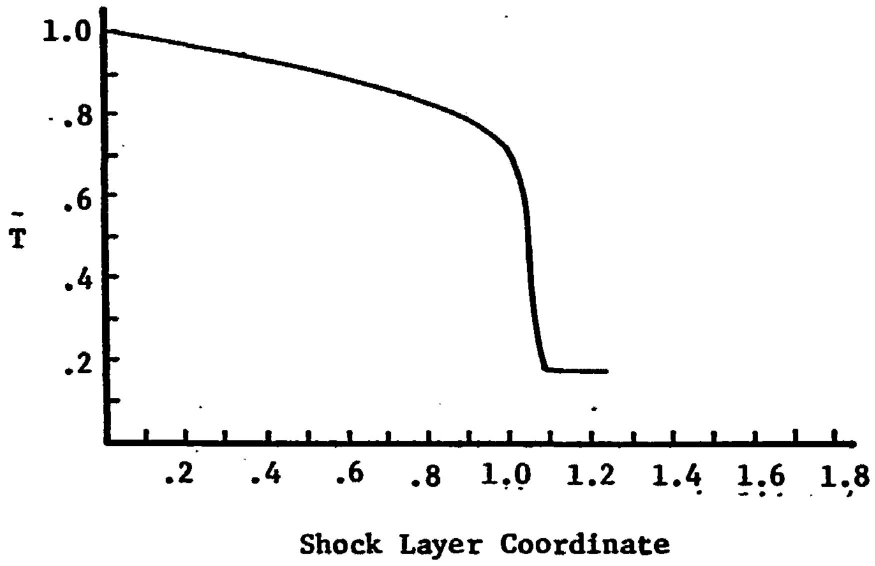

Figure 5.38 Temperature Profile for 10^2 Enhancement with Two Energy Group Absorption Coefficient

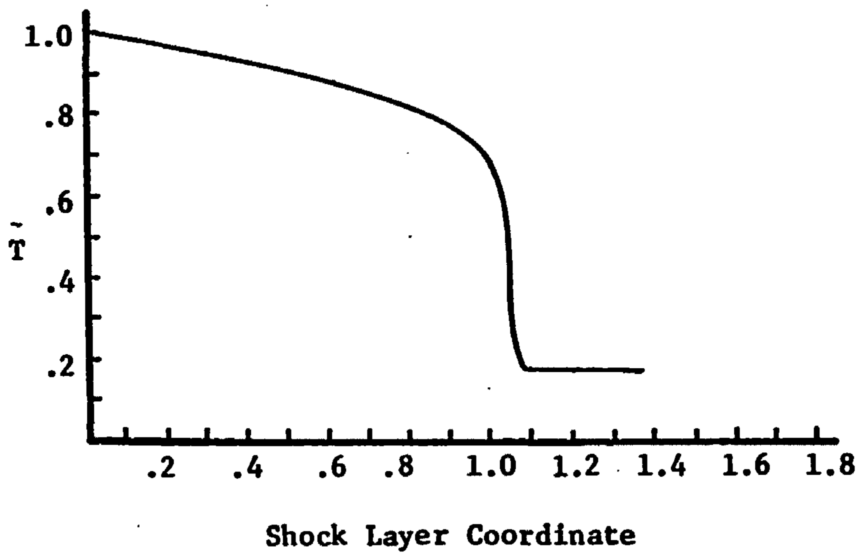

Figure 5.39 Temperature Profile for 10^3 Enhancement with Two Energy Group Absorption Coefficient

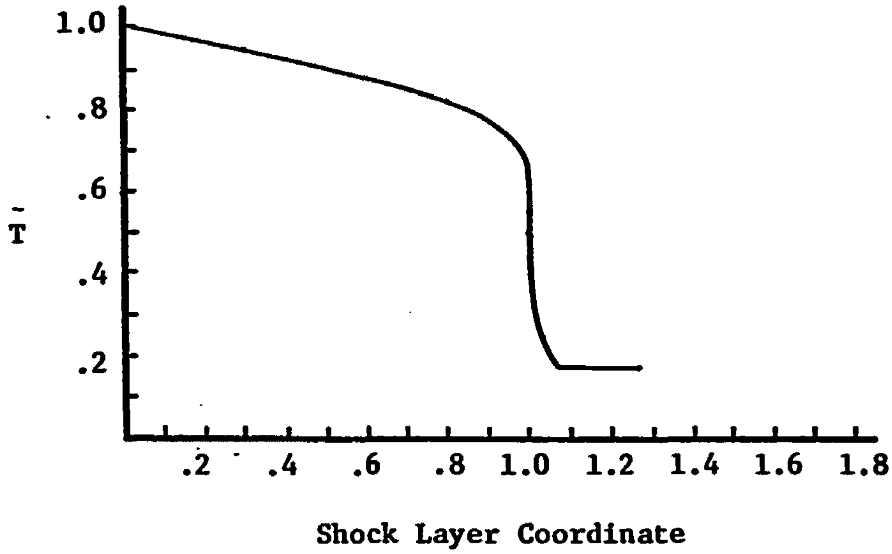

Figure 5.40 Temperature Profile for 10^4 Enhancement with Two Energy Group Absorption Coefficient

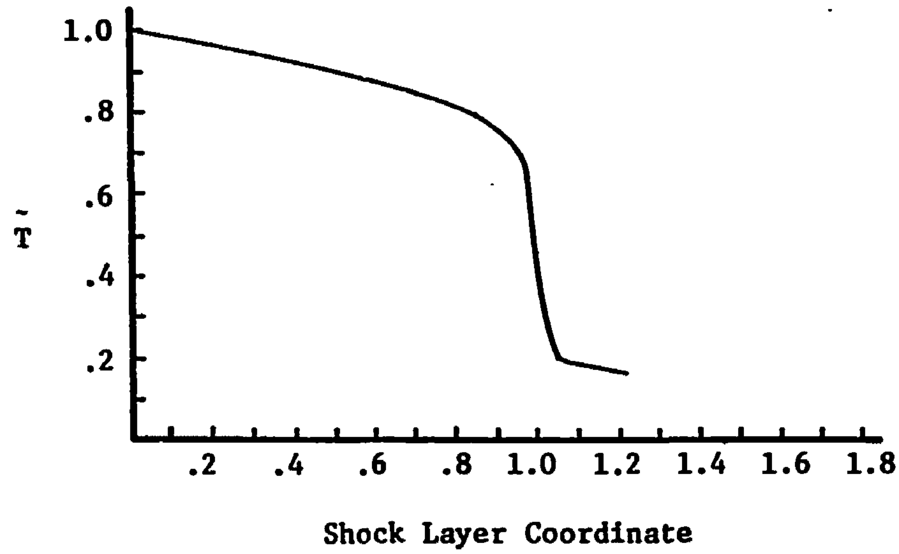

Figure 5.41 Temperature Profile for 10^5 Enhancement with Two Energy Group Absorption Coefficient

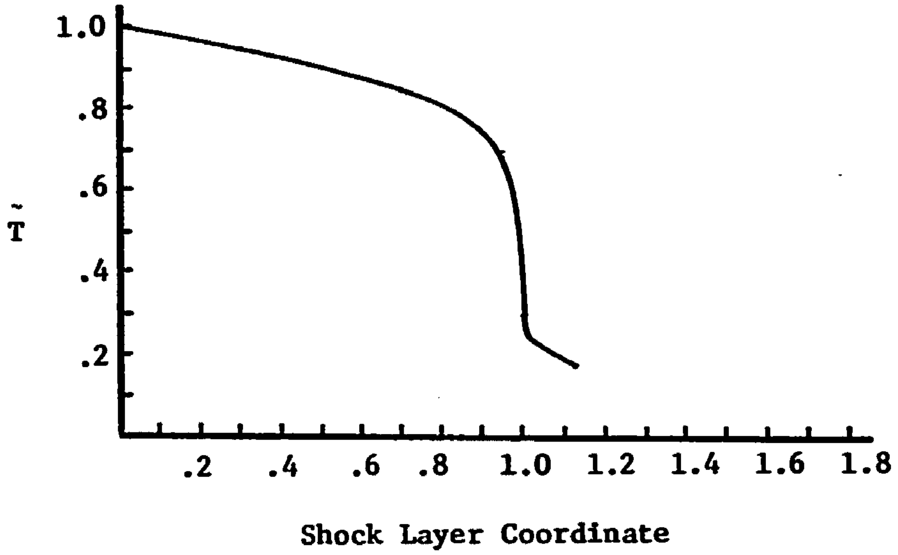

Figure 5.42 Temperature Profile for 10^6 Enhancement with Two Energy Group Absorption Coefficient

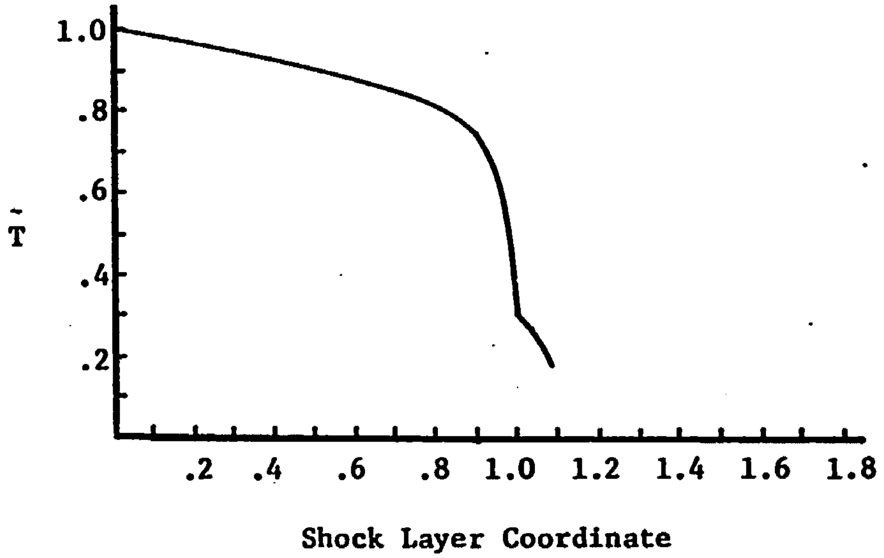

Figure 5.43 Temperature Profile for 8.2×10^6 Enhancement with Two Energy Group Absorption Coefficient

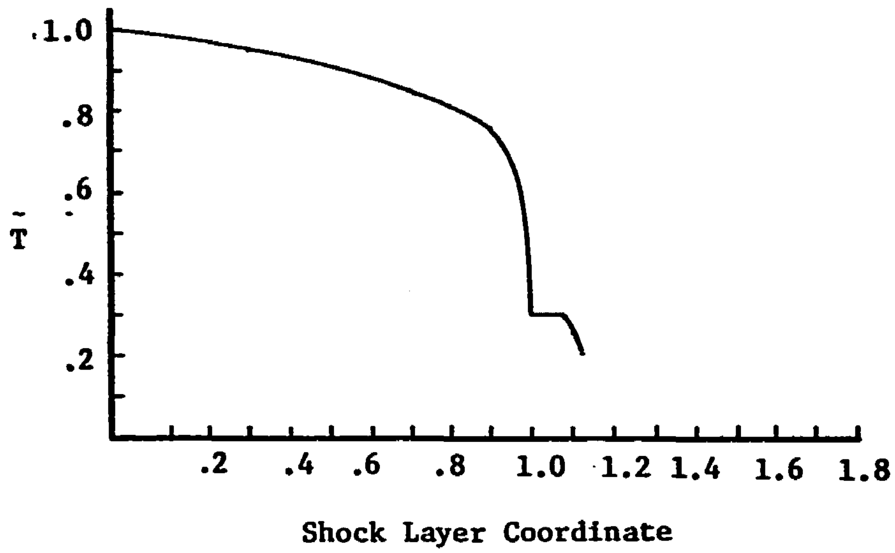

Figure 5.44 Temperature Profile for 1.3×10^7 Enhancement with Two Energy Group Absorption Coefficient

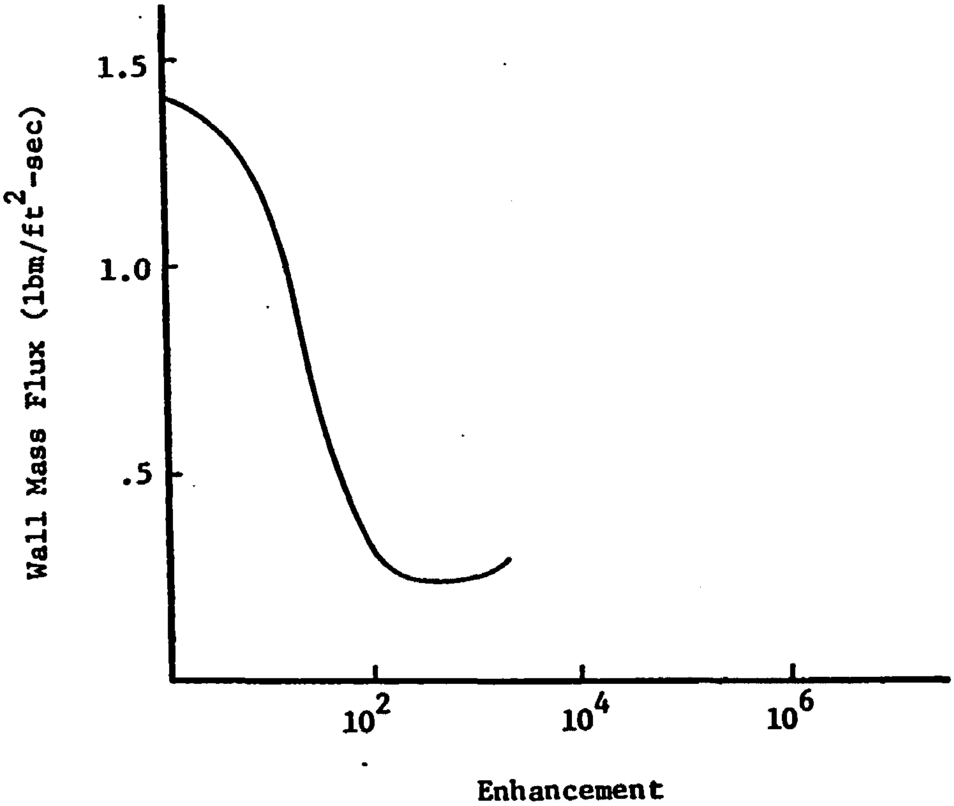

Figure 5.45 Vacuum Ultraviolet Enhancement

enhancement and we see that a minimum does occur. From the point of view of reducing the ablation mass loss, the rapid reduction and minimum of .246 lbm/ft^2-sec compared to two band enhancement which only reduced to .438 lbm/ft^2-sec is very significant. Single band enhancement is more practical than multiband enhancement because it can be accomplished by seeding the ablator with selected highly absorbing species. The optical depths and components of the heat flux at both the wall and interface are shown in Figs. 5.46 and 5.47 respectively. Like the two band enhancement, the minimum, which occurs at an enhancement of 400, is due to the visible band heat flux increasing because this band is very optically thin. Also note the striking increase in the vacuum ultraviolet heat flux to the interface. As can be seen from Figs. 5.48-5.51 which show the temperature profiles for vacuum ultraviolet enhancements of 200, 400, 10^3, and $2x10^3$, the increased interface heat flux is due to diffusion of energy by conduction from the shock layer and thus increasing the emissive power. This characteristic could not be observed by a nonheat-conducting model.

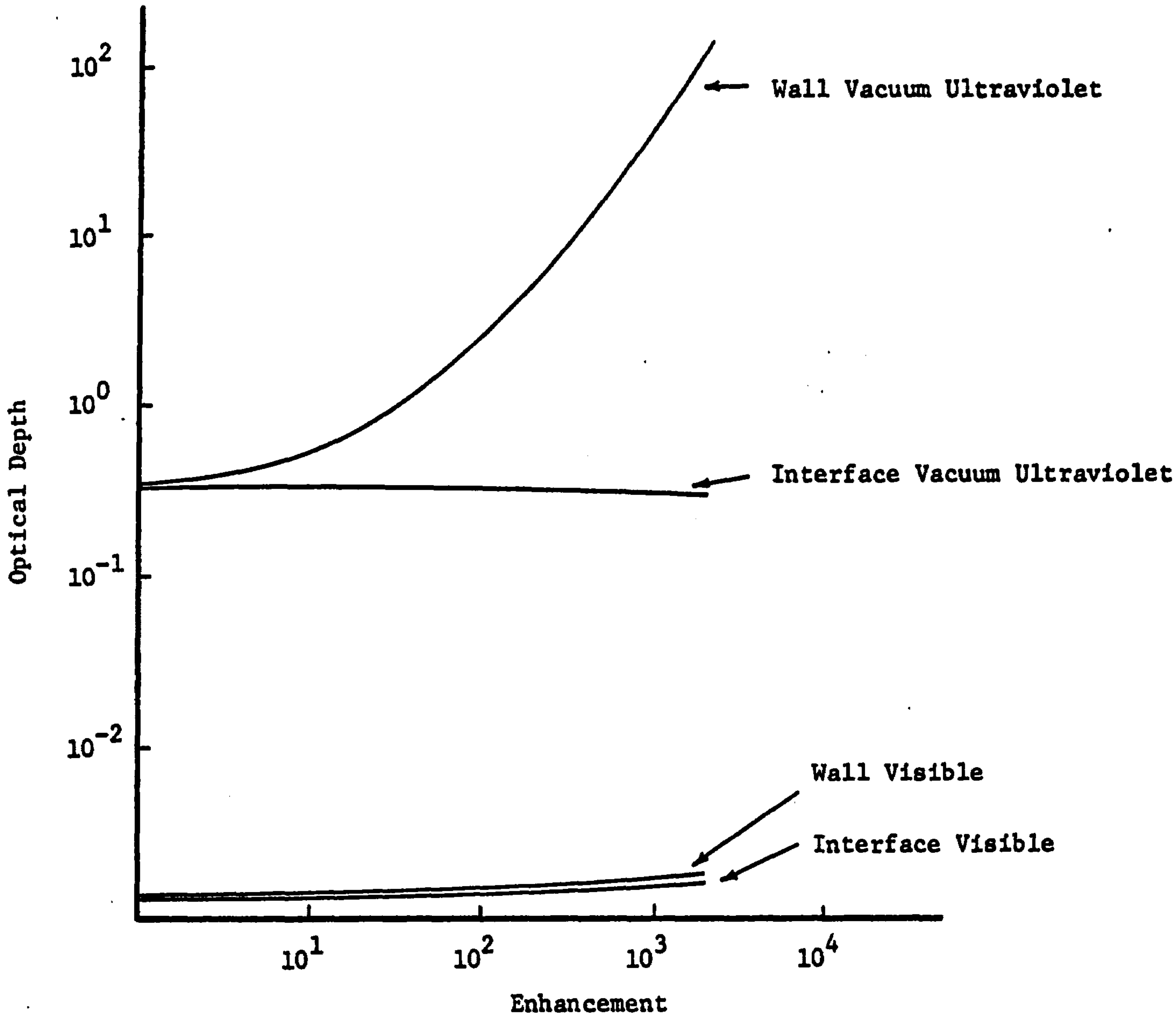

Figure 5.46 Spectral Optical Depths with Vacuum Ultraviolet Enhancement

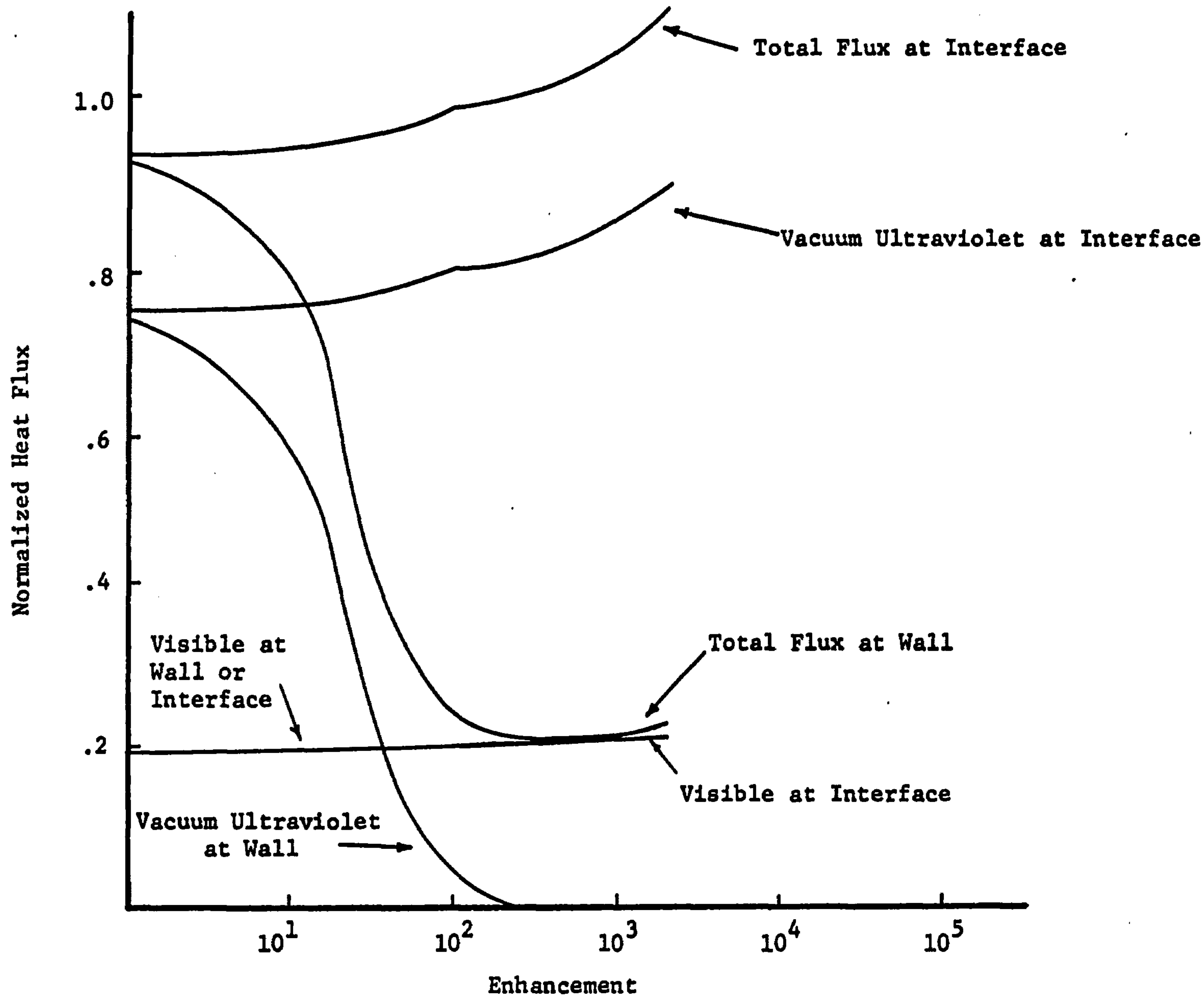

Figure 5.47 Spectral Radiative Flux Toward the Wall with Vacuum Ultraviolet Enhancement

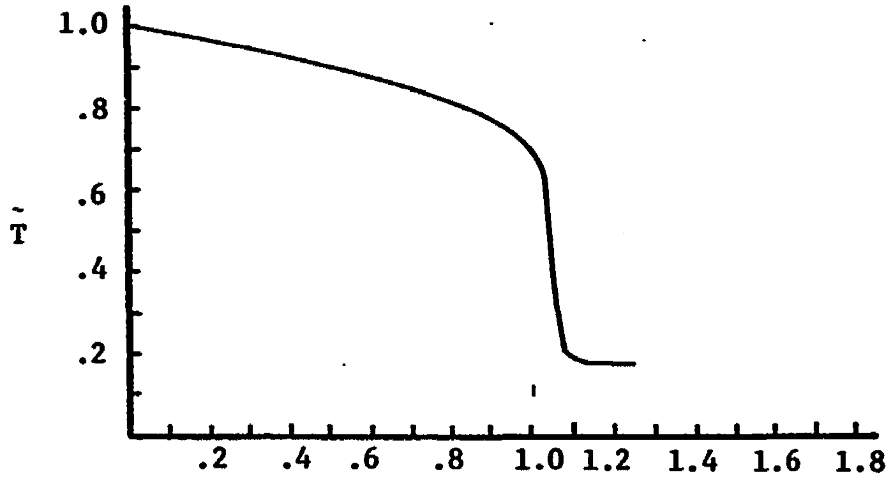

Shock Layer Coordinate

Figure 5.48 Temperature Profile for $2x10^2$ Enhancement of the Vacuum Ultraviolet

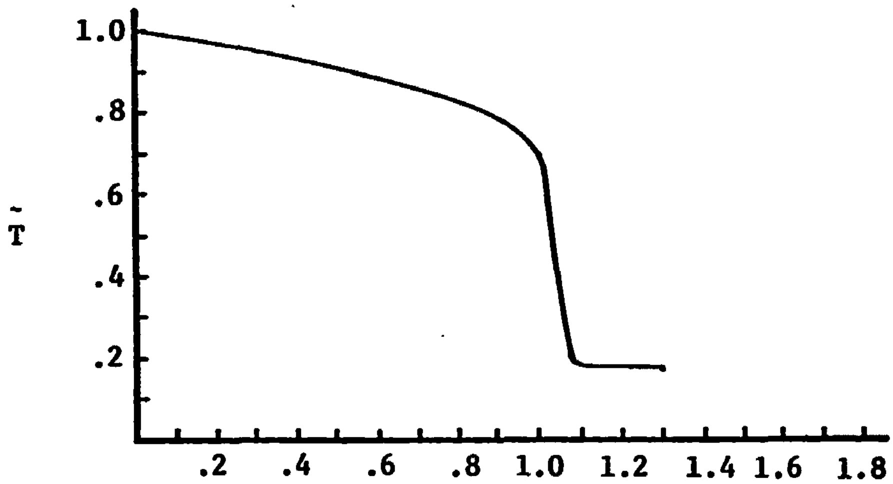

Shock Layer Coordinate

Figure 5.49 Temperature Profile for $4x10^2$ Enhancement of the Vacuum Ultraviolet

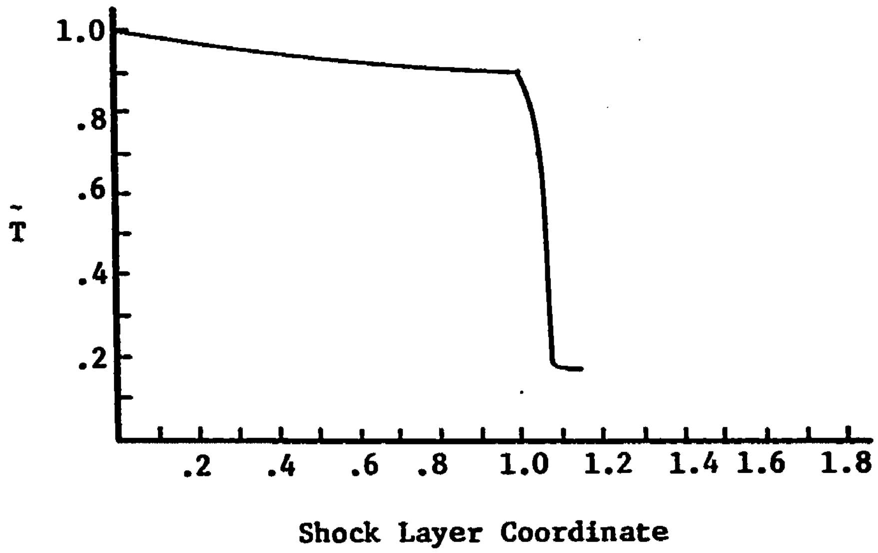

Figure 5.50 Temperature Profile for 10^3 Enhancement of the Vacuum Ultraviolet

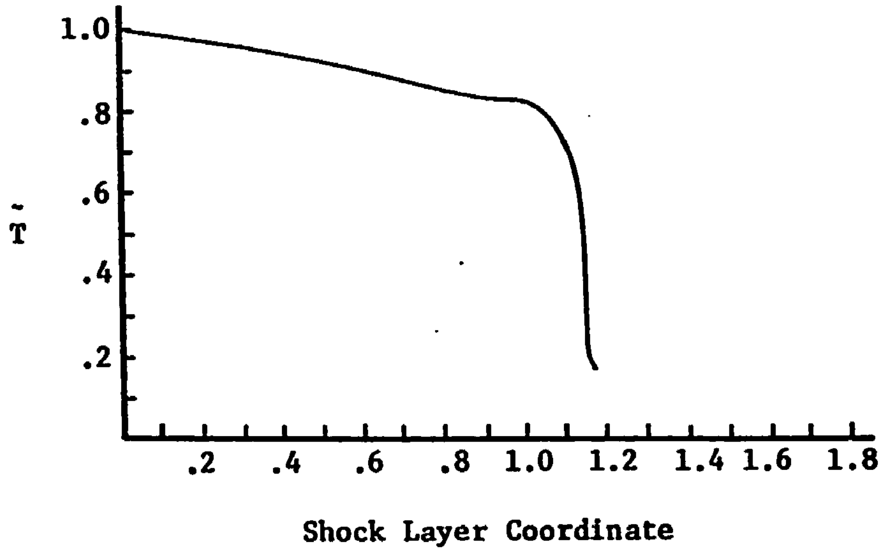

Figure 5.51 Temperature Profile for $2x10^3$ Enhancement of the Vacuum Ultraviolet

CHAPTER VI

CONCLUSIONS AND RECOMMENDATIONS

The results of both the grey-gas and two-step continuum absorption coefficient calculations show that as the ablation layer absorption coefficient is enhanced a minimum in the ablation mass loss rate is reached. Enhancement of the absorption coefficient beyond that necessary to give a minimum causes the wall mass loss rate to increase and the trend indicates that the improved ablator performance through enhancement can be lost with too much enhancement. Calculations that do not couple the ablation mass loss rate with the wall heat flux fail to predict an eventual ablation mass loss rate increase and thus caution should be exercised when drawing conclusions about ablator performance from models that hold the wall mass flux fixed.

With ablation layer enhancement of a single absorption coefficient energy band, a rapid decrease in ablation mass loss rate is experienced and a minimum occurs. This single energy band enhancement can be used to simulate injection through ablator seeding of molecules that are highly absorbing in one energy band. Again the minimum is an indicator that too much enhancement, simulating too much seeding, can be detrimental to ablator performance.

Within the framework of a grey-gas approximation, one can, through numerical enhancement, study the full range of ablation layer optical thicknesses from thin to thick without making a priori approximations. In addition, with numerical enhancement, a selected energy band of the absorption coefficient can also be varied through all optical thicknesses.

Although there are no published results with which to make comparisons over the full range of enhancements, comparisons at zero enhancement are good and trends at large enhancements are very similar to published limiting cases.

The inclusion of thermal conductivity was found to stabilize the numerical scheme and although the conduction term in the energy equation is dominant near the interface, conduction has very little effect on the overall results. With the thermal conductivity reduced to approximately zero, an increase of 5% in the wall radiative heat flux was observed. This increase came for the zero enhancement case and is due to a lack of thermal diffusion from the high temperature shock layer into the lower temperature ablation layer. It was found a posteriori that thermal diffusion in the current model caused the ablation layer near the interface to be hot for the enhanced cases, thus simulating the real case of highly emitting ablation species being transferred by molecular diffusion into the high temperature shock layer.

For the grey-gas case, increasing the effective heat of ablation causes a much greater decrease in wall mass loss rate than the same multiplicative factor increase in ablation layer absorption coefficient through enhancement. The decrease in wall mass loss rate with increased effective heat of ablation continues through the lower limits of massive blowing theory without reaching a minimum.

Comparisons of the current grey-gas results for varying nose radius with published results show the same trends and confirm that a minimum in wall mass loss rate does occur and is due to transition from a radiation dominant regime to a conduction dominant regime.

Because of the simplicity of the absorption coefficient models used in this analysis, it is not possible to make specific recommendations as to which energy bands, when enhanced, will have the greatest effect on wall mass loss rate. We have demonstrated that different energy band enhancement can have different effects. It is recommended that calculations be made using detailed air opacities which include lines and real candidate ablator vapor opacities. As an improvement to numerical enhancement of the ablation layer opacities one could incorporate the diffusion equation into the current two inviscid layer scheme and obtain selected enhancement by increasing a particular specie concentrations as it leaves the wall. With the data from this type of analysis one could give guidance for new ablation material development that could result in minimizing the ablation mass loss for a particular mission.

LIST OF REFERENCES

Anderson, J.A., Jr, "A Simplified Analysis for Re-Entry Stagnation Point Heat Transfer from a Viscous Nongray Radiating Shock Layer," AIAA 6th Aerospace Sciences Meeting, AIAA Paper No. 68-164, 1968a.

Anderson, J.A., Jr, "An Engineering Survey of Radiating Shock Layers," AIAA Entry Vehicle Systems and Technology Meeting, AIAA Paper No. 68-1151, 1968b.

Bartlett, E.P., W.E. Nicolet, and J.T. Howe, "Heat-Shield Ablation at Superorbital Reentry Velocities," Aerotherm TN No. 69-63, Aerotherm Corporation, Mountain View, CA, 1969.

Bryson, A.E., and Yu-Chi Ho, *Applied Optimal Control*, Ginn and Company, 1969.

Bryson, A.E., and W.F. Denham, "A Steepest-Ascent Method for Solving Optimum Programming Problems," Journal of Applied Mechanics, pp 247-257., 1962.

Bryson, A.E., W.F. Denham, F.J. Carroll, and K. Mikami, "Determination of Lift or Drag Programs to Minimize Re-Entry Heating," Journal of Aerospace Sciences, pp 420-430, 1962.

Byers, J.A. and J. Killen, "Finite-Difference Methods for Collisionless Plasma Models," *Methods in Computational Physics*, Vol. 9, Plasma Physics, Academic Press, 1970.

Callis, L.B., "Time Asymptotic Solutions of Blunt-Body Stagnation-Region Flows with Nongray Emission and Absorption of Radiation," AIAA Fluid and Plasma Dynamics Conference, AIAA Paper No. 68-663, 1968.

Carnahan, B., H.A. Luther, J.O. Wilkes, *Applied Numerical Methods*, John Wiley and Sons, Inc., 1969.

Chapman, G.T., "Heat Transfer in the Stagnation-Point Laminar Boundary Layer with Mass Transfer and Radiant Energy Absorption," *Proceedings of the 1967 Heat Transfer and Fluid Mechanics Institute*, Stanford University Press, pp 163-188, 1967.

Cheng, P. and W.E. Vincenti, "Inviscid Radiating Flow Over a Blunt Body," Journal of Fluid Mechanics, Vol. 27, pp 625-646, 1967.

Chin, J.H., "Inviscid Radiating Flow Around Bodies, Including the Effect of Energy Loss and Non-Grey Self-Absorption," LMSC 668005, Lockheed Missiles & Space Company, Sunnyvale, CA, 1965.

Chin, J.H., "Radiation Transport for Stagnation Flows Including the Effect of Lines and Ablation Layer," AIAA Fluid and Plasma Dynamics Conference, AIAA Paper No. 68-664, 1968.

Cole, J.D. and J. Aroesty, "The Blowhard Problem--Inviscid Flows with Surface Injection," International Journal of Heat and Mass Transfer, Vol. XI, No. 7, pp 1167-1183, 1968.

Douglas, J., Jr, "The Effect of Round-Off Error in the Numerical Solution of the Heat Equation," Journal of A.C.M., Vol. 6, pp 48-58, 1959.

Gera, J., "Branched Trajectory Optimization by the Projected Gradient Technique," AIAA Journal, Vol. 8, No. 6, pp 1121-1126, 1959.

Goulard, R., "Similarity Parameters in Radiative Gas-Dynamics, " *High Temperature in Aeronautics*, C. Ferrari, ed. Pergamon Press, Inc., pp 181-210, 1964.

Hayes, W.D., "Some Aspects of Hypersonic Flow," The Ramo-Wooldridge C. P. Report, Los Angeles, CA, 1955.

Hayes, W.D. and R.F. Probstein, *Hypersonic Flow Theory*, Academic Press, 1959.

Hansen, C.F., "Approximations for the Thermodynamic and Transport Properties of High-Temperature Air," NASA TR R-50, 1959.

Hildebrand, F.B., *Methods of Applied Mathematics*, Prentice Hall, 1965.

Hoshizaki, H. and K.H. Wilson, "Viscous Radiating Shock Layer About a Blunt Body," AIAA Journal, Vol. 3, No. 9, pp 1614-1622, 1965.

Hoshizaki, H. and L.E. Lasher, "Heat Transfer to an Ablating Body," AIAA Journal, Vol. 6, No. 8, pp 1441-1449, 1968.

Howe, J.T., "Shielding of Partially Reflecting Stagnation Surfaces Against Radiation by Transpiration of an Absorbing Gas," NASA TR R-95, 1961.

Howe, J.T. and J.R. Viegas, "Solutions of the Ionized Radiating Shock Layer, Including Reabsorption and Foreign Species Effects, and Stagnation Region Heat Transfer," NASA TR R-159, 1963.

Jischke, M.C. and J.R. Baron, "Application of the Method of Parametric Differentiation to Radiative Gasdynamics," AIAA Journal, Vol. 7, No. 7, pp 1326-1355, 1969.

Martin, J.J., *Atmospheric Reentry*, Prentice Hall, 1966.

McCalla, T.R., *Introduction to Numerical Methods and Fortran Programming*, John Wiley and Sons Inc., 1967.

Moretti, G. and Albbett, M., "A Time Dependent Computational Method for Blunt Body Flows," AIAA Journal, Vol 4, No. 12, pp 2136-2141, 1966.

Nerem, R.M., "An Approximate Analyses of Thermal Conduction and Radiative Transport in the Stagnation-Point Shock Layer," AIAA Journal, Vol 4, No. 3, pp 539-541, 1966.

Olstad, W.B., "Nongray Radiating Flow About Smooth Symmetric Bodies with Large Blowing," AIAA 4th Thermophysics Conference, 1969.

Olstad, W.B., "Stagnation-Point Solutions for Inviscid Radiating Shock Layers," NASA TN D-5792, 1970.

Olstad, W.B., "Nongray Radiating Flow About Smooth Symmetric Bodies," AIAA Journal, Vol 9, No. 1, 1971.

Page, W.A., D.L. Compton, W.J. Borucki, D.L. Ciffone, and D.M. Cooper, "Radiative Transport in Inviscid Nonadiabatic Stagnation-Region Shock Layers," AIAA 3rd Thermophysics Conference, AIAA Paper No. 68-784, 1968.

Penner, S.S., M. Thomas, and G. Adomeit, "Similarity Parameters for Radiative Energy Transfer in Isothermal and Nonisothermal Gas Mixtures," *Supersonic Flow Chemical Processes and Radiative Transfer*, D.B. Olfe and V. Zakkay, eds., Pergamon Press Inc., pp 279-305, 1964.

Richtmyer, R.D., and K.W. Morton, *Difference Methods for Initial-Value Problems*, Interscience Publishers, 1967.

Roberts, K.V., and N.O. Weiss, "Convective Difference Schemes," *Mathematics of Computation*, No. 20, pg 272, 1966.

Schechter, R.S., *The Variational Method in Engineering*,McGraw-Hill, 1967.

Stewartson, K., *The Theory of Laminar Boundary Layers in Compressible Fluids*, Oxford University Press, London, 1964.

Vincenti, W.G. and C.H. Kruger, Jr, *Introduction to Physical Gas Dynamics*, John Wiley and Sons, Inc., 1965.

Vincenti, W.G. and B.S. Baldwin, Jr., "Effect of Thermal Radiation on the Propagation of Plane Acoustic Waves," Journal of Fluid Mechanics, Vol. 12, pt. 3, pg. 449, 1962.

Wakefield, R.M. and J.H. Lundell, "Comparison of the Performance of a Charring Ablator Under Transient and Constant Combined Convective and Radiative Heating," AIAA 7th Aerospace Sciences Meeting, AIAA Paper No. 69-151, 1969.

Wallace, J and N. Kemp, "Similarity Solutions to the Massive Blowing Problem," AIAA Journal, Vol. 7, No. 8, pg 1517, 1969.

Wilson, K.H., "Stagnation Point Analysis of Coupled Viscous-Radiating Flow with Massive Blowing," NASA CR 1548, 1970.

Yoshikawa, K.K. and D.R. Chapman, "Radiative Heat Transfer and Absorption Behind a Hypersonic Normal Shock Wave," NASA TN D-1424, 1962.

APPENDIX A

CONSERVATION LAW FORMULATIONS

The geometry and nomenclature for the inviscid hypervelocity flow field are given in Fig. A.1. As $x/R_n << 1$ in the stagnation region the conservation equations for a general two-dimensional or axisymmetric flow field may be greatly simplified (Chin, 1968). For the hypervelocity case, the kinetic energy change across the shock layer is small compared to enthalpy change and the pressure variation along the stagnation streamline is very small. The shock and dividing streamline or interface are assumed to be concentric with the body surface. Under these assumptions the conservation equations are:

continuity,

$$\frac{\partial x^L \rho u}{\partial x} + \frac{\partial A x^L \rho v}{\partial y} = 0; \qquad \text{A.1}$$

x-momentum,

$$u \frac{\partial u}{\partial x} + v \frac{\partial u}{\partial y} + Kuv = - 1/\rho \frac{\partial P}{\partial x} ; \qquad \text{A.2}$$

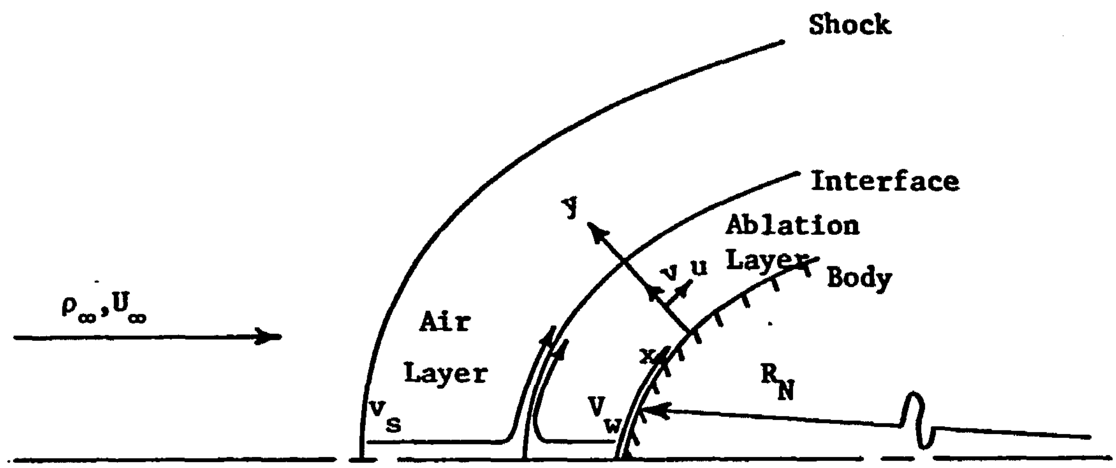

Figure A.1 Geometry and Nomenclature Blunt Body Flow

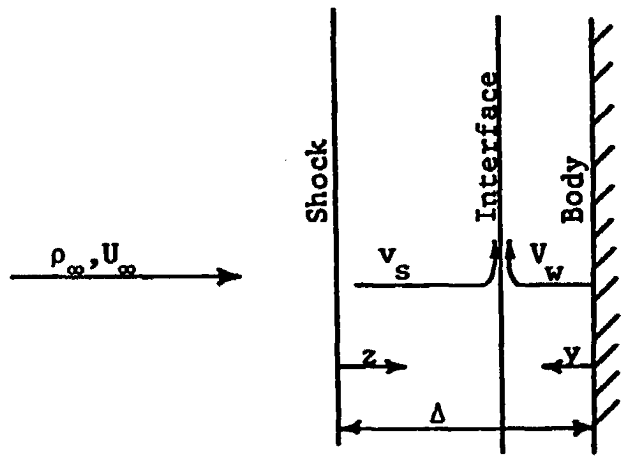

Figure A.2 Stagnation Point Slab Geometry y-momentum,

$$P = P_s = \rho_\infty U_\infty^2(1-\varepsilon)\left(1 - \frac{x^2}{R_N^2}\right) + P_\infty; \qquad \text{A.3}$$

and energy,

$$u \frac{\partial h}{\partial x} + Av \frac{\partial h}{\partial y} = - \frac{A}{\rho} \operatorname{div} \bar{q} \qquad \text{A.4}$$

where L is zero for two-dimensional and one for axisymmetric flow, K is the body curvature (equal to $1/R_N$ at the stagnation point), A is a geometry factor equal to (1+Ky) but assumed constant and equal to one (for thin shock layers Ky is very small in comparison with unity) and div $\bar{q}$ is the divergence of the heat flux.

The boundary conditions are:

at the shock, $y = \Delta$,

$$\begin{aligned} u &= u_s = U_\infty \frac{x}{R_N}, \\ v &= v_s = -\varepsilon U_\infty, \\ h_s &= h_s(\rho_\infty, V_\infty), \\ \varepsilon &= \varepsilon(\rho_\infty, V_\infty); \end{aligned} \qquad \text{A.5}$$

at the interface, $y = \Delta_a$, unknown prior to the solution,

$$v = 0 \; ; \tag{A.6}$$

and at the wall, $y = 0$,

$$v = V_w = \dot{m}_w / \rho_w = \frac{\text{heat absorbed at wall}}{\rho_w H_{eff}} \; ,$$

$$u = u_w = 0 \; , \tag{A.7}$$

$$h_w = h_w(P_w, T_w) \; ,$$

T_w is the sublimation temperature .

For this compressible inviscid flow, Chin (1965) used transformations similar to the Lees-Dorodnitsyn transformations for compressible boundary layers (Hayes and Probstein, 1959, pg 290) and assumed similarity to obtain the following results for the shock layer:

$$F = \frac{\rho v}{\rho_s v_s} \; , \qquad \frac{dF}{d\xi} = - \frac{u}{u_s} \tag{A.8}$$

$$d\xi = (L+1) \frac{\rho}{\rho_s} \frac{dz}{\varepsilon R_N} \; , \quad g = \frac{h}{h_s} \; , \tag{A.9}$$

$$F \frac{d^2F}{d\xi^2} = \frac{1}{L+1} \left[\left(\frac{dF}{d\xi} \right)^2 - 2\varepsilon(1-\varepsilon) \frac{\rho_s}{\rho} \right] , \tag{A.10}$$

and

$$F\frac{dg}{dz} = -\frac{2}{\rho_\infty U_\infty^3}\frac{dq}{dz} \qquad \text{A.11}$$

where z is a coordinate which is zero at the shock and increases toward the body (see Fig. A.2). In Eqs. A.8 and A.11, it has been assumed that the shock stand-off distance is small compared to the nose radius so that $A \approx 1$. The boundary conditions under this transformation become:

at the shock, $\xi = z = 0$,

$$F = -\frac{dF}{d\xi} = g = 1 \qquad \text{A.12}$$

and at the interface, $\xi = \xi_i$, unknown prior to the solution,

$$F = 0. \qquad \text{A.13}$$

For the ablation layer, Chin (1968) used similar transformation techniques to obtain the following results:

$$F = \frac{\rho v}{\rho_w V_w},\ \frac{dF}{d\eta} = -\frac{u\rho_w^{1/2} R_N}{U_\infty \rho_\infty^{1/2} x[2(1-\epsilon)]^{1/2}}, \qquad \text{A.14}$$

$$d\eta = (L+1)\frac{\rho}{\rho_w}\left(\frac{2\rho_\infty U_\infty^2}{\rho_w V_w^2}\right)^{1/2}\frac{dy}{R_N},\ g = \frac{h}{h_w}, \qquad \text{A.15}$$

$$F\frac{d^2F}{d\eta^2} = \frac{1}{(L+1)}\left[\left(\frac{dF}{d\eta}\right)^2 - \frac{\rho_w}{\rho}\right], \qquad \text{A.16}$$

and

$$F\frac{dg}{dy} = -\frac{1}{\rho_w V_w h_w}\frac{dq}{dy} \qquad \text{A.17}$$

where y is a coordinate which is zero at the wall and increases toward the shock. Again we have assumed $A \approx 1$, because the interface standoff distance is much less than the nose radius. In obtaining Eq. A.16 a term was found negligible by noting that

$$1 \gg \frac{\rho_w V_w^2}{\rho_\infty U_\infty^2} \simeq 10^{-4}$$

for the no absorption enhancement case at 190,000 feet and 55,000 feet per second and decreased with absorption enhancement because V_w decreased. The boundary conditions for the ablation layer equations are:

at the wall, $\eta = y = 0$,

$$F = 1, \quad \frac{dF}{d\eta} = 0, \quad g = 1 , \qquad \text{A.18}$$

and at the interface, $\eta = \eta_i$, unknown a priori

$$F = 0 . \qquad \text{A.19}$$

Let us now consider the momentum equations (A.10 and A.16) and develop a unified equation which describes the momentum field in either layer. This is simply done by defining

$$f(\zeta) = \begin{cases} 2\varepsilon(1-\varepsilon)\rho_s/\rho(\xi), & \text{shock layer} \\ \rho_w/\rho(\eta) & , \text{ablation layer} \end{cases} \qquad \text{A.20}$$

which yields the unified momentum equation as

$$F\, F'' = \sigma[F'^2 - f(\zeta)]. \qquad \text{A.21}$$

In this equation it was convenient to replace $\frac{1}{(L+1)}$ by σ where

$$\sigma = \begin{cases} 1 & , \text{two-dimensional planar flow} \\ \tfrac{1}{2} & , \text{axisymmetric flow} \end{cases} .$$

In the shock layer $\zeta \to \xi$ while in the ablation layer $\zeta \to \eta$. The prime notation indicates derivatives with respect to the independent variable ζ. The unified boundary conditions are

at $\zeta = 0$,

$$F = 1, \quad F' = -\gamma, \qquad \text{A.22}$$

at $\zeta = \zeta_1$,

$$F = 0 \qquad \text{A.23}$$

where γ is 1 for the shock layer and zero for the ablation layer.

The energy equations (A.11 and A.17) are equivalent as can be shown by returning all variables to dimensional form. With Eqs. A.8 and A.9, Eq. A.11 becomes

$$\rho v \frac{dh}{dz} = - \frac{2\rho_\infty U_\infty h_s}{\rho_\infty U_\infty^3} \frac{dq}{dz} \qquad \text{A.24}$$

where mass continuity ($\rho_s v_s = \rho_\infty U_\infty$) has been used. We can now write the one-dimensional energy relation across a normal shock as

$$h_s = \frac{1}{2} U_\infty^2 (1-\varepsilon^2) + h_\infty ,$$

but for the free stream conditions of interest $\varepsilon \sim .06$ and $h_\infty << U_\infty^2$ we have

$$h_s \simeq \frac{1}{2} U_\infty^2 .$$

Now Eq. A.24 becomes

$$\rho v \frac{dh}{dz} = - \frac{dq}{dz} . \qquad \text{A.25}$$

We can follow the same procedure with Eq. A.17 to get identical results but in the y-coordinate frame. With the change of variable $z = \Delta - y$ (see Fig. A.2), the ablation layer energy equation becomes Eq. A.25 and we now have one expression for the energy equation and it is valid from the shock to the body. The boundary conditions are:

at $z = 0$ (shock),

$$h = h_s , \tag{A.26}$$

and at $z = \Delta$ (body)

$$h = h_w . \tag{A.27}$$

Equations A.21 and A.25 along with their respective boundary conditions and the appropriate equations of state close into a consistent set of three equations (A.21, A.25, and A.28) and three unknowns (ρ,v, and h) by the state equation

$$h = h(P,\rho) . \tag{A.28}$$

The inclusion of pressure in Eq. A.28 does not add an additional unknown because by Eq. A.3 we have assumed the pressure to be constant in the stagnation region.

APPENDIX B

THERMODYNAMIC AND RADIATIVE PROPERTIES

In order to carry out the solutions to the conservation equations it is necessary to have either tabulations or expressions for state, thermodynamic, and radiative properties of both the air and ablative species. For simplicity and computational speed, we have in general resorted to analytical expressions for property values. The equation of state correlations and Planck mean absorption coefficients are taken from Olstad (1970), the gas thermal conductivity data was curve fit from Hansen (1959), and the two energy group absorption coefficient data was taken from Page et al. (1968). These properties are discussed in the remainder of this Appendix.

Olstad noted that the available data for both density and temperature could be approximately represented by functions separable in the variables pressure and enthalpy in the form $(P/P_o)^n f(h/RT_o)$. From plots of $f(h/RT_o)$ for various pressures he deduced

$$T = 308.8 \left(\frac{P}{P_o}\right)^{0.09} \left(\frac{h}{RT_o}\right)^{0.55}, \ ^\circ K \qquad \text{B.1}$$

and

$$\rho/\rho_o = 7.944 \left(\frac{P}{P_o}\right)^{0.96} \left(\frac{RT_o}{h}\right) \qquad \text{B.2}$$

where P_o is sea-level standard pressure, ρ_o is sea-level standard density, T_o is 273°K, and R is the gas constant for air ($2.882\text{x}10^6$ cm^2/sec^2-°K). Upon inversion and units conversion Eq. B.1 becomes

$$h = \frac{33.85}{P^{.1635}} \left(\frac{T}{556}\right)^{1.819}, \ \frac{Btu}{lb_m} \qquad \text{B.3}$$

with T in °R and P in atmospheres. In the convective terms of the energy equation (Eq. 3.36) we must treat the expression $d\tilde{h}/d\tilde{z}$ which can be expanded to

$$\frac{d\tilde{h}}{d\tilde{z}} = \frac{\partial\tilde{h}}{\partial\tilde{T}} \frac{d\tilde{T}}{d\tilde{z}} + \frac{\partial\tilde{h}}{\partial\tilde{P}} \frac{d\tilde{P}}{d\tilde{z}} \ . \qquad \text{B.4}$$

For our stagnation-point solution, we have assumed the pressure to be constant and therefore the last term in Eq. B.4 is zero. By Eq. B.3 we now have

$$\frac{\partial\tilde{h}}{\partial\tilde{T}} = \frac{61.6}{h_s P^{.1635}} \left(\frac{T_s}{556}\right)^{1.819} (\tilde{T})^{.819} \ . \qquad \text{B.5}$$

Equation B.2 can also be converted to our system of units yielding

$$\rho/\rho_o = 7.944(P)^{1.1235} \left(\frac{T}{556}\right)^{-1.819} \ . \qquad \text{B.6}$$

This equation of state information was developed for air but in the current analysis was also used for the ablative products. This approximation not only simplifies the computational procedure but also allows consideration of ablative materials over a wide range of radiative and decomposition properties while maintaining the same equations of state. This prevents the ill-defined ablator-material equation of state information in today's literature from masking the prime considerations of this analysis, namely, effects of varying radiative and decomposition properties.

It is desirable to be able to make flow field calculations for various free stream velocities and altitudes. For the flight regime of interest in the current analysis (nominal 200,000 feet and 50,000 feet per second), ideal gas relations across a normal shock give a density ratio of .1667 while the Mollier Diagram gives .0582 through an iterative solution. In order to keep our calculations economical without the extremely large errors of ideal gas calculations, Olstad's shock condition correlations

$$T_s = 1038 \left(\frac{\rho_\infty}{\rho_o}\right)^{0.09} U_\infty^{1.28}, \ ^\circ K$$

and

$$\varepsilon = \frac{\rho_\infty}{\rho_s} = .0695 \left(\frac{\rho_\infty}{\rho_o}\right)^{0.04} U_\infty^{0.08}$$

were used. In these expressions U_∞ is in kilometers per second. We can now convert to our system of units yielding

$$T_s = 1870 \left(\frac{\rho_\infty}{\rho_o}\right)^{0.09} \left(\frac{U_\infty}{3.28}\right)^{1.28}, \ ^\circ R \qquad \text{B.7}$$

and

$$\varepsilon = .0695 \left(\frac{\rho_\infty}{\rho_o}\right)^{0.04} \left(\frac{U}{3.28}\right)^{0.08} \qquad \text{B.8}$$

where now U_∞ is in kilofeet per second. The results of Eqs. B.7 and B.8 were compared with Mollier Diagram results for the nominal flight conditions and correction factors of .897 and .935 respectively were applied to these equations yielding

$$T_s = 1678 \left(\frac{\rho_\infty}{\rho_o}\right)^{0.09} \left(\frac{U_\infty}{3.28}\right)^{1.28}, \ ^\circ R \qquad \text{B.9}$$

and

$$\varepsilon = .0650 \left(\frac{\rho_\infty}{\rho}\right)^{0.04} \left(\frac{U_\infty}{3.28}\right)^{0.08} . \qquad \text{B.10}$$

Equations B.9 and B.10 are now exact at 200,000 feet and 50,000 feet per second and yield accurate results in the full range of flight conditions studied. The remaining needed shock condition, P_s, can be determined by inverting Eq. B.6 to get

$$P = .147\left(\frac{T}{556}\right)^{1.618}\left(\frac{\rho}{\rho_o}\right)^{.89} \qquad \text{B.11}$$

which when evaluated at the shock yields

$$P_s = .147\left(\frac{T_s}{556}\right)^{1.618}\left[\left(\frac{1}{\varepsilon}\right)\left(\frac{\rho_\infty}{\rho_o}\right)\right]^{.89} . \qquad \text{B.12}$$

The thermal conductivity data were taken from Hansen (1959) where the data are tabulated every 500°K from 500-15,000°K and at each order of magnitude pressure change from 10^{-4}-100 atmospheres. Because the parametric studies on absorption enhancement, nose radius and effective heat of ablation were run at 190,000 feet and 55,000 feet per second where the pressure behind the shock is 1.03 atmospheres it was sufficient to use only the one atmosphere thermal conductivity data. As can be seen from Fig. B.1, the thermal conductivity is a highly varying function of temperature and in order to have an accurate representation the curve was divided into six temperature ranges (less than 3000, 3-4000, 4-600, 6-800, 8-11,000, and greater than 11,000°K). Within each temperature range the thermal conductivity was fit to a 6th order polynomial in temperature with a min-max curve fit technique. On comparing the polynomial results with the tabulated data a maximum error of 6.6% was determined at 4,500°K.

For the grey-gas calculations of this study the Planck mean absorption coefficient as defined by

$$\alpha_P = \frac{\int_0^\infty \alpha_\nu B_\nu d\nu}{\int_0^\infty B_\nu d\nu}$$

was selected as the grey-gas absorption coefficient. Olstad (1970) was

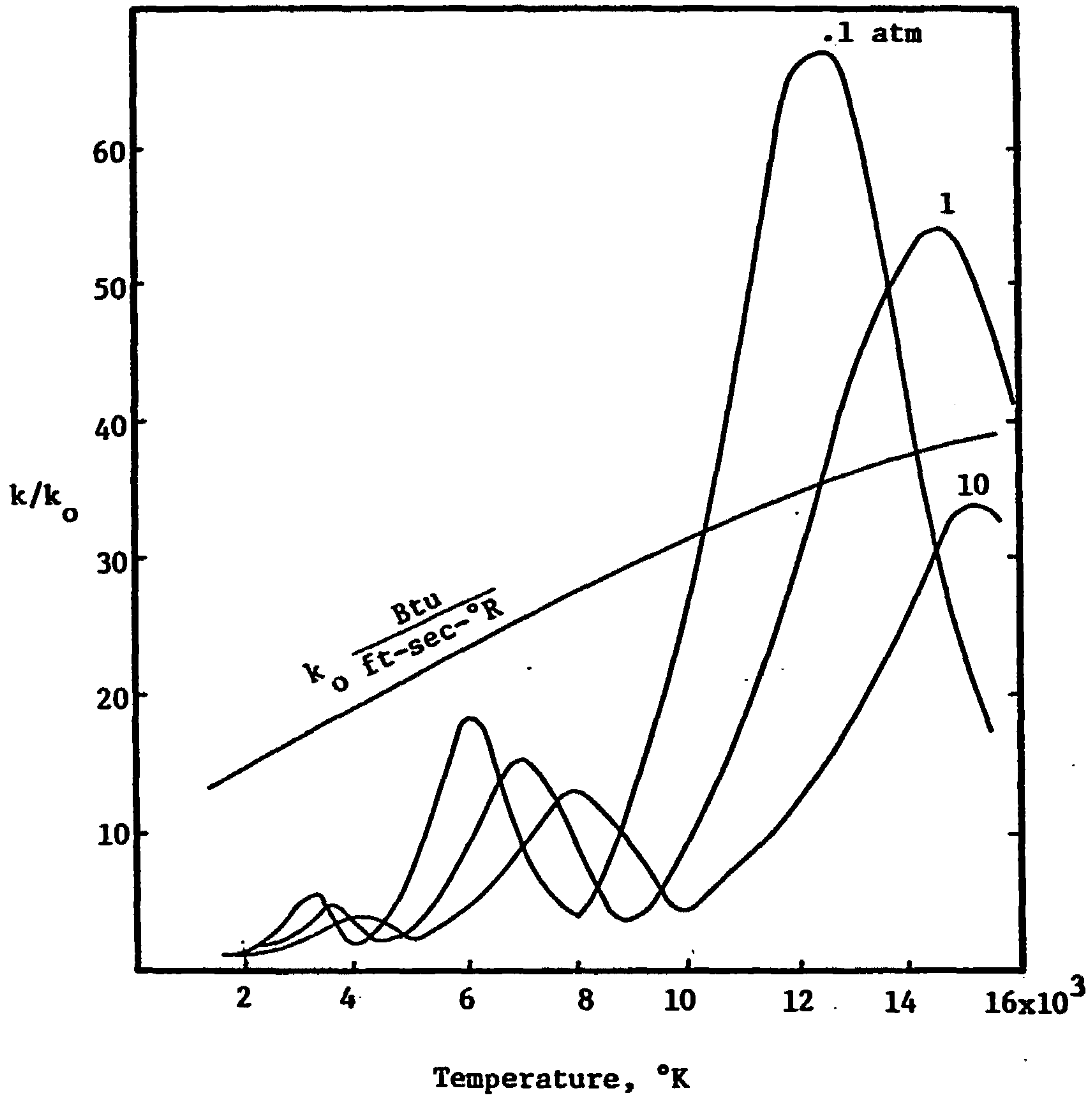

Figure B.1 Thermal Conductivity of Air

able to approximate the curves for the variation of $\log_{10} \alpha_P$ with $\log_{10} T$ with straight lines to get

$$\alpha_P = 7.94\times10^{-26}\left(\frac{\rho}{\rho_o}\right)^{3.25} T^{\left[6.0 - .5\log_{10}\left(\frac{\rho}{\rho_o}\right)\right]}, \mathrm{cm}^{-1}$$

which he found valid for temperatures up to 20,000°K at pressures from 10^{-1} to 10^{1} atmospheres. At lower pressures the formula is only valid to lower temperatures; for example, at 10^{-3} atmospheres the maximum temperature for which the formula is valid is 15,000°K. It is more desirable for the current work to express the Planck mean absorption coefficient in terms of temperature and pressure. Through the use of cross plotting Olstad also determined

$$\alpha_P = 1.19\times10^{-9}(P)^{\left[1.9685 - .174\ell n_e(P)\right]}\left(\frac{T}{556}\right)^{\left[4.631 - .1896\ell n_e(P)\right]} \mathrm{ft}^{-1} \qquad \text{B.13}$$

where again P is in atmospheres and T is in °R.

Although Eq. B.13 is the appropriate Planck mean absorption coefficient for air, it was also used for the ablative layer in the zero absorption enhancement case. In order to simulate numerically the effects of absorption enhanced ablative products, the Planck mean absorption coefficient for air was increased by a multiplicative factor (Th) applied uniformly through the ablative layer (see Fig. B.2a). This technique is representative of a case where all the ablative species demonstrate enhanced absorption characteristics because as shown by Fig. B.2b which is taken from Wilson (1970) the ablative product mass fraction is uniform through most of the ablative layer. If one

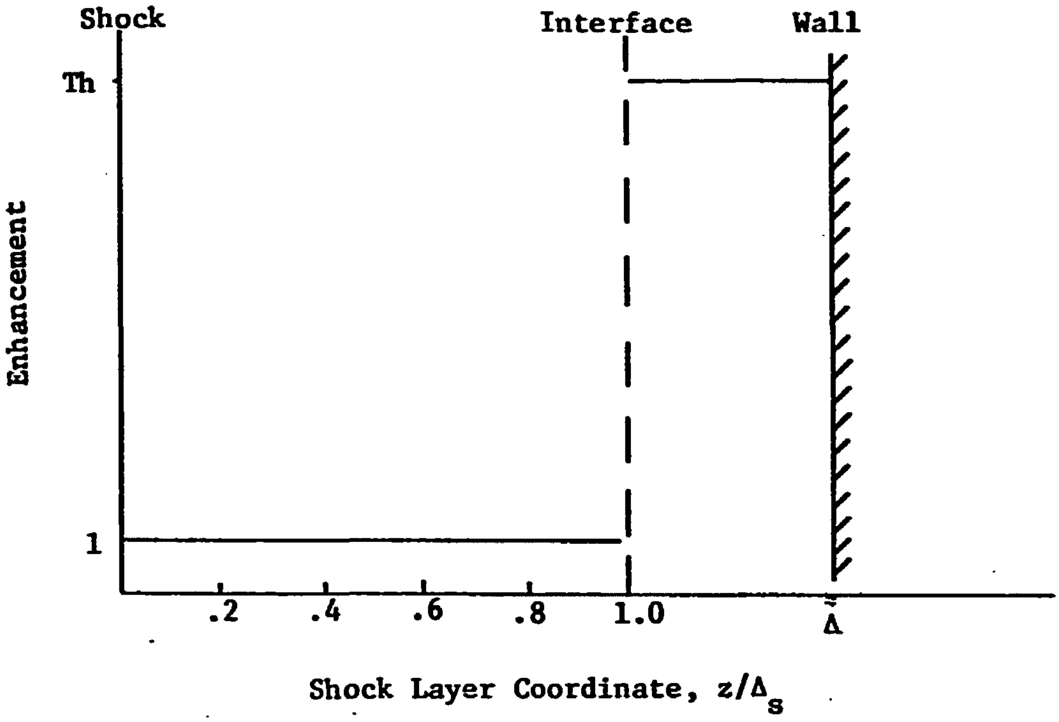

(a) Model

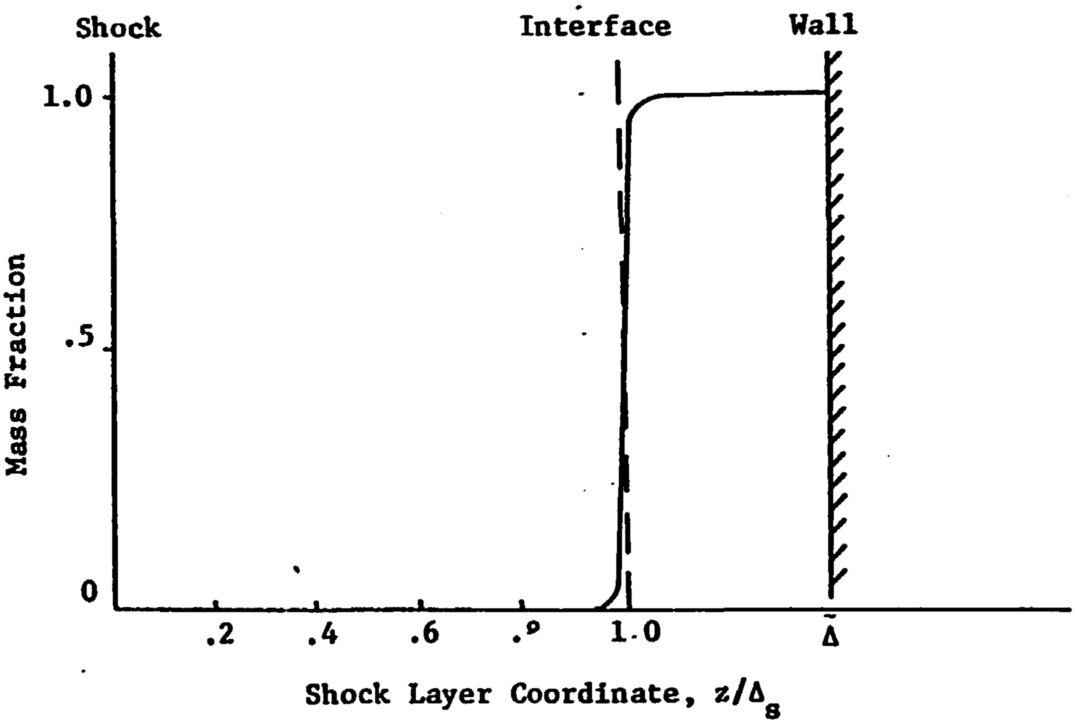

(b) Actual

Figure B.2 Absorption Enhancement Factor (Th) and Typical Ablative Product Mass Fraction desired to enhance the absorption characteristics of the ablative layer by some species that only forms away from the wall by chemical reaction with diffused free-stream constituents or due to the elevated temperature near the interface as is the case for neutral carbon and carbonitride (CN) for the Apollo material (see Fig. B.3b which is taken from Bartlett et al. (1969). It could not be simulated by the step function Th of Fig. B.2a. This simulation would require a multiplicative function like Di shown in Fig. B.3a. Figure B.4a shows a typical temperature profile from the current analysis along with a quantitative plot of Eq. B.13. Figure B.4b shows the same Planck mean absorption coefficient when operated on by the enhancement parameter Th. The second curve in Fig. B.4b illustrates how a diffusive enhancement parameter, Di, would affect the grey absorption coefficient.

The multistep or multienergy group absorption coefficient model is represented by

$$\alpha_\nu = \sum_{j=1}^{JS} \alpha_j(P,T)H(\nu-\nu_{j-1})H(\nu_j-\nu) \qquad \text{B.14}$$

where H(x) is the Heaviside function defined in Chapter II. As is pointed-out in Chapter III, a step function representation of the absorption coefficient can be made as accurate as desired by simply increasing the number of frequency steps, JS. It should also be noted that there is no loss in generality by requiring the cut-off frequencies (i.e., ν_1, $\nu_2 \cdots \nu_j \cdots \nu_{JS}$) to be the same for the shock and ablative layers. This can best be seen in Fig. B.5 where a hypothetical shock absorption coefficient with considerable frequency dependence for high

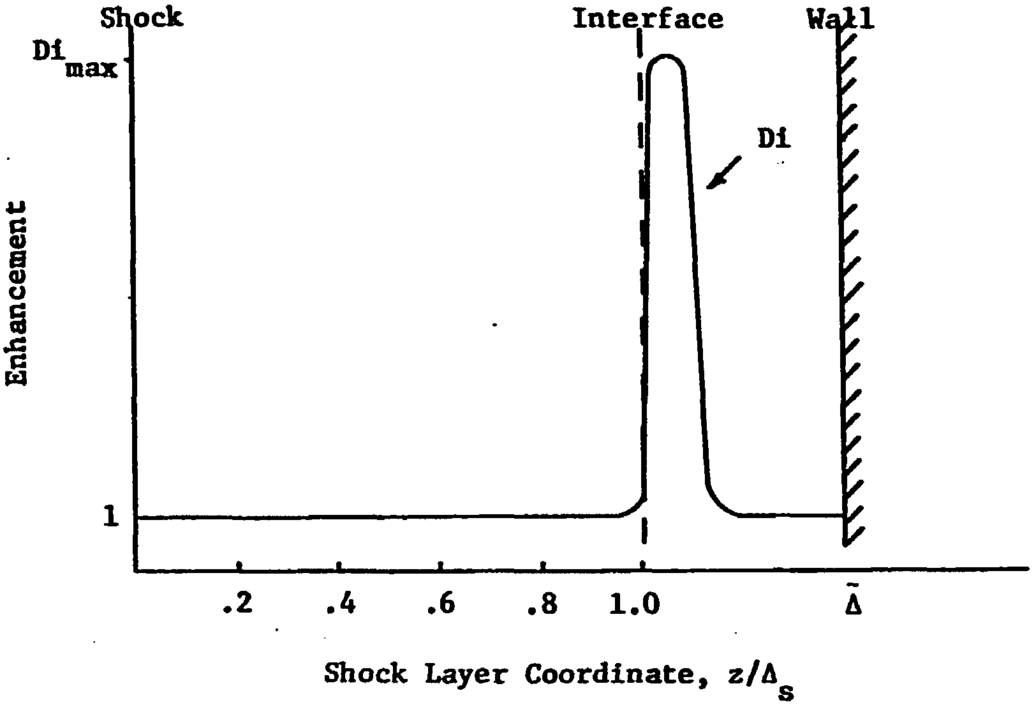

(a) Model

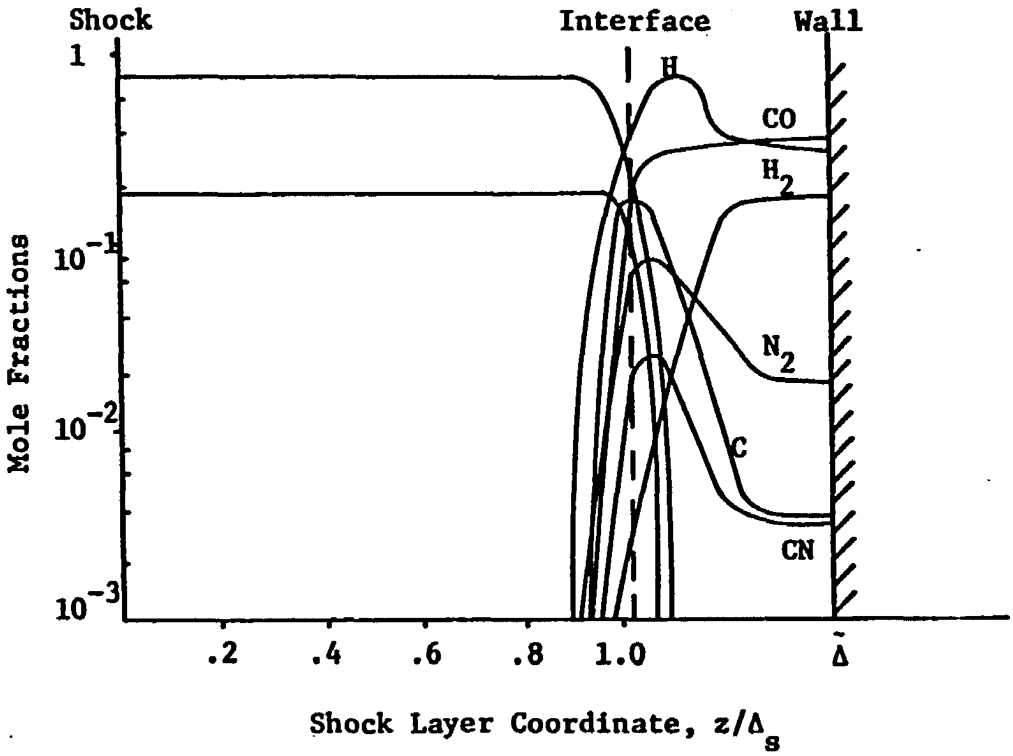

(b) Actual

Figure B.3 Absorption Enhancement Factor (Di) and Typical Apollo Material Ablative Product Mole Fractions

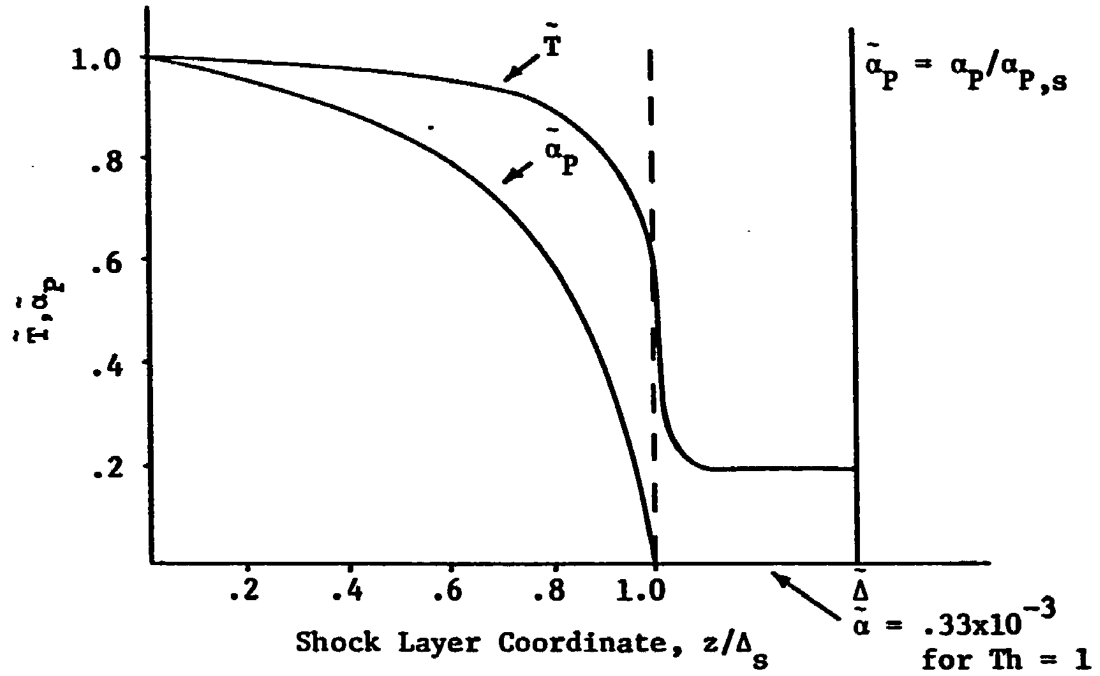

(a) Th = 1

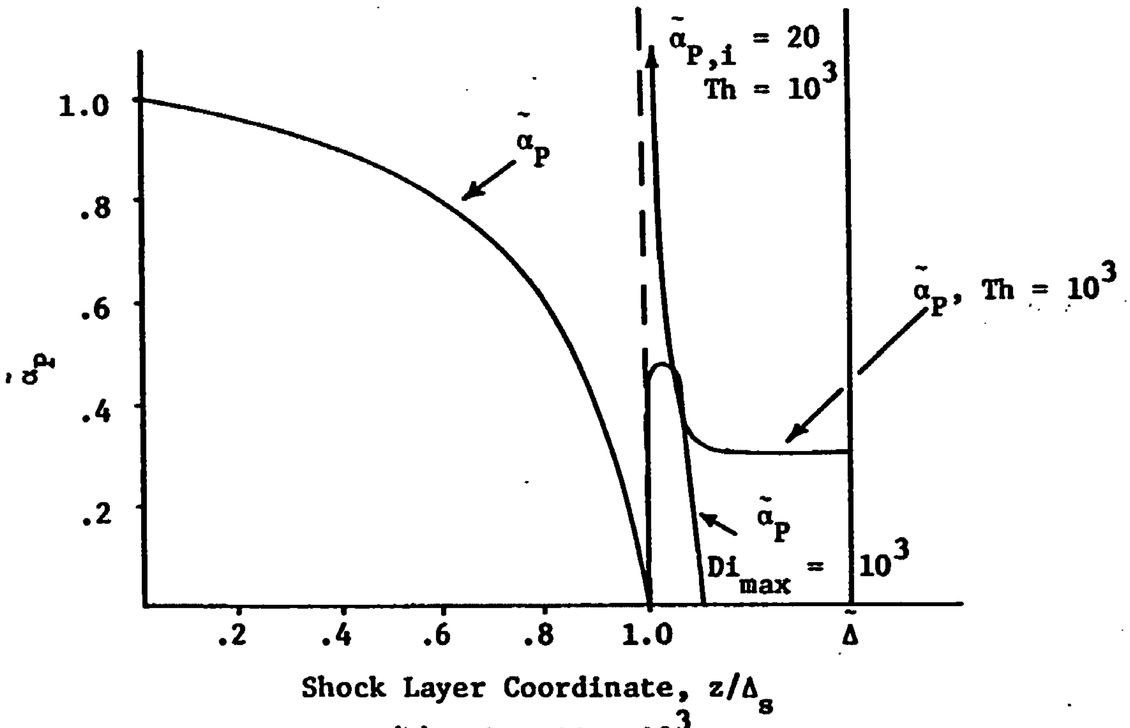

(b) $Th = Di = 10^3$

Figure B.4 Effects of Enhancement on the Planck Mean Absorption Coefficient

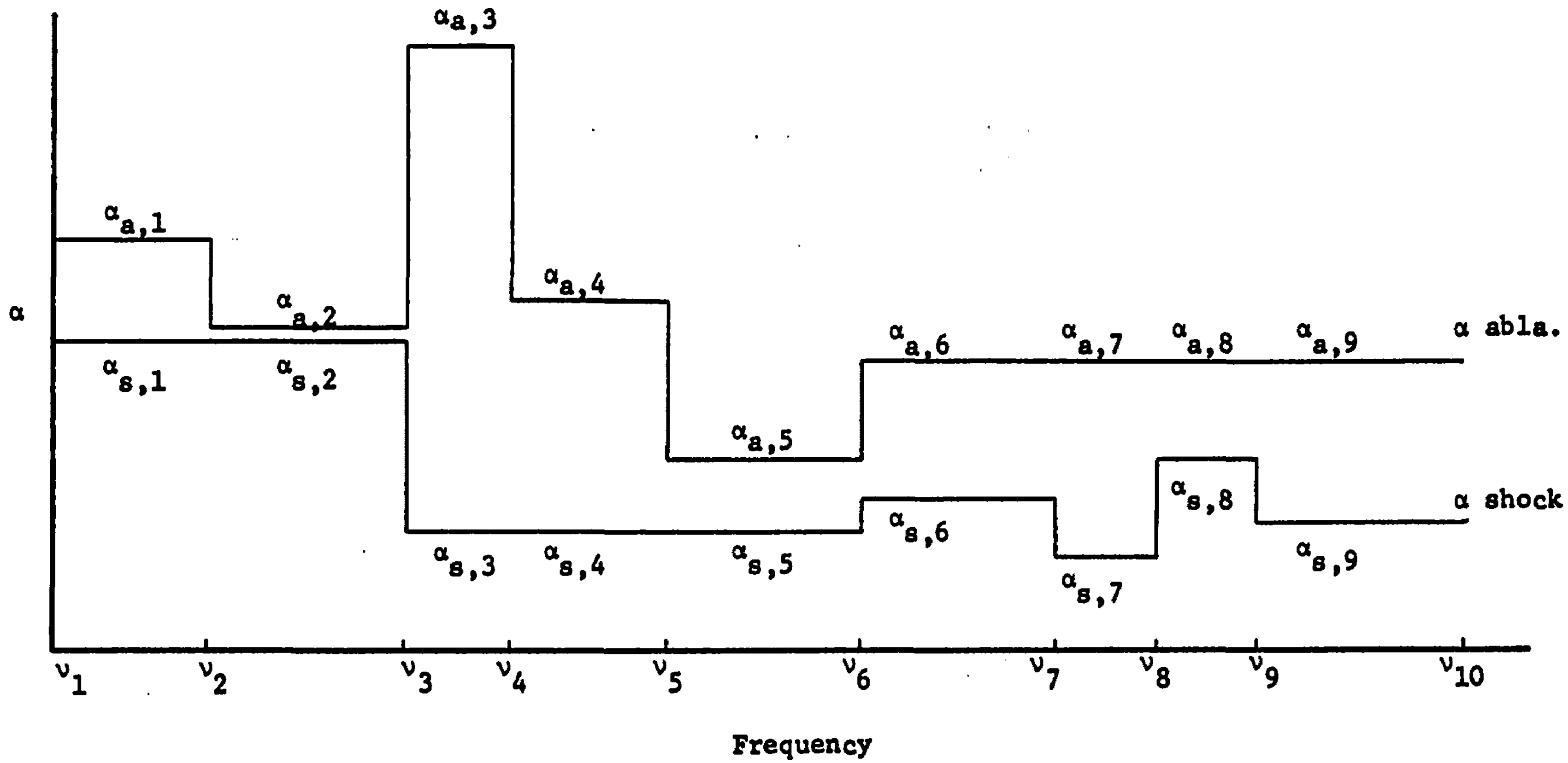

Figure B.5 Schematic Representation of the Ablation and Shock Layer Absorption Coefficients

frequencies is represented by $\alpha_{s,j}$ while the ablative absorption coefficient with considerable frequency dependence for low frequencies is represented by $\alpha_{a,j}$. The result is that when either layer requires substantial frequency detail, the other layer has some adjacent frequency groups with identical absorption coefficients. The effects of either gross or diffusive absorption enhancement in a particular frequency band can be simulated by making the enhancement parameters frequency dependent giving Th_j and Di_j. These parameters are shown schematically in Fig. B.6. An example of enhancement in a particular band which could be accurately represented by the gross enhancement parameter, Th_j, is the injection of CO_2 which is highly absorbent in the vicinity of 10.6 microns. Increases in this Th_j would simulate increases in the injected mass flux of CO_2.

The two energy group absorption coefficient model used in the current analysis consists of a visible continuum (1130 Å $< \lambda < \infty$) band and a vacuum ultraviolet continuum ($0 < \lambda <$ 1130 Å) band. The actual values were taken from the two continuum steps of Page et al. (1968) where he presents a four band model at a pressure of one atmosphere. This particular model was chosen in anticipation of making additional calculations with Page's lines included, but the incompatibility of his vacuum ultraviolet line data (Page treated this group of lines as a single "equivalent" heavily self-absorbed line with a Lorentz profile) with our current step model prevented this extension. Figure B.7 gives this two band absorption model and for comparison shows the Planck mean absorption coefficient Eq. B.13 and Anderson's (1968b) two step model. It is interesting to note that Page's visible continuum absorption

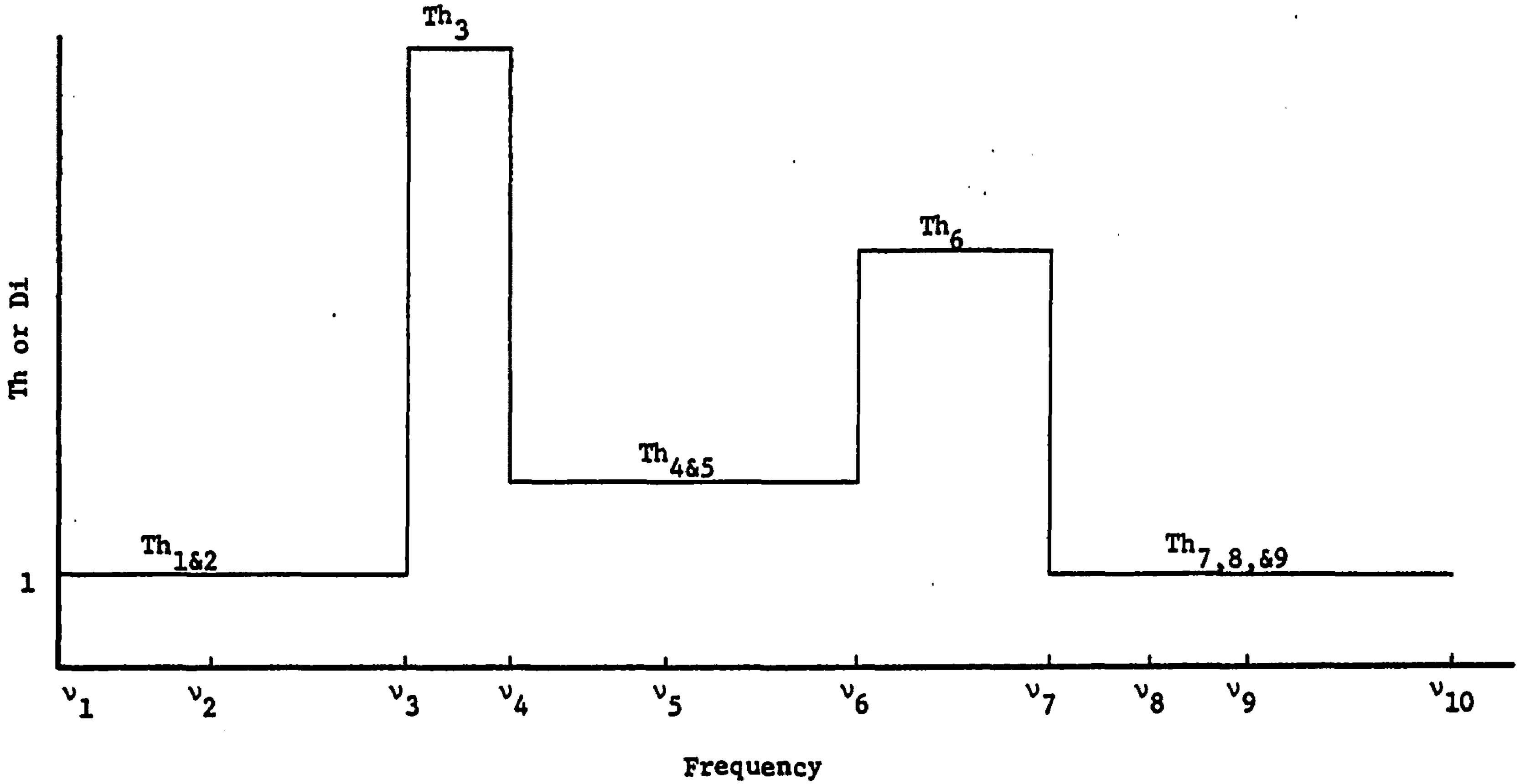

Figure B.6 Schematic Representation of the Absorption Enhancement Parameters

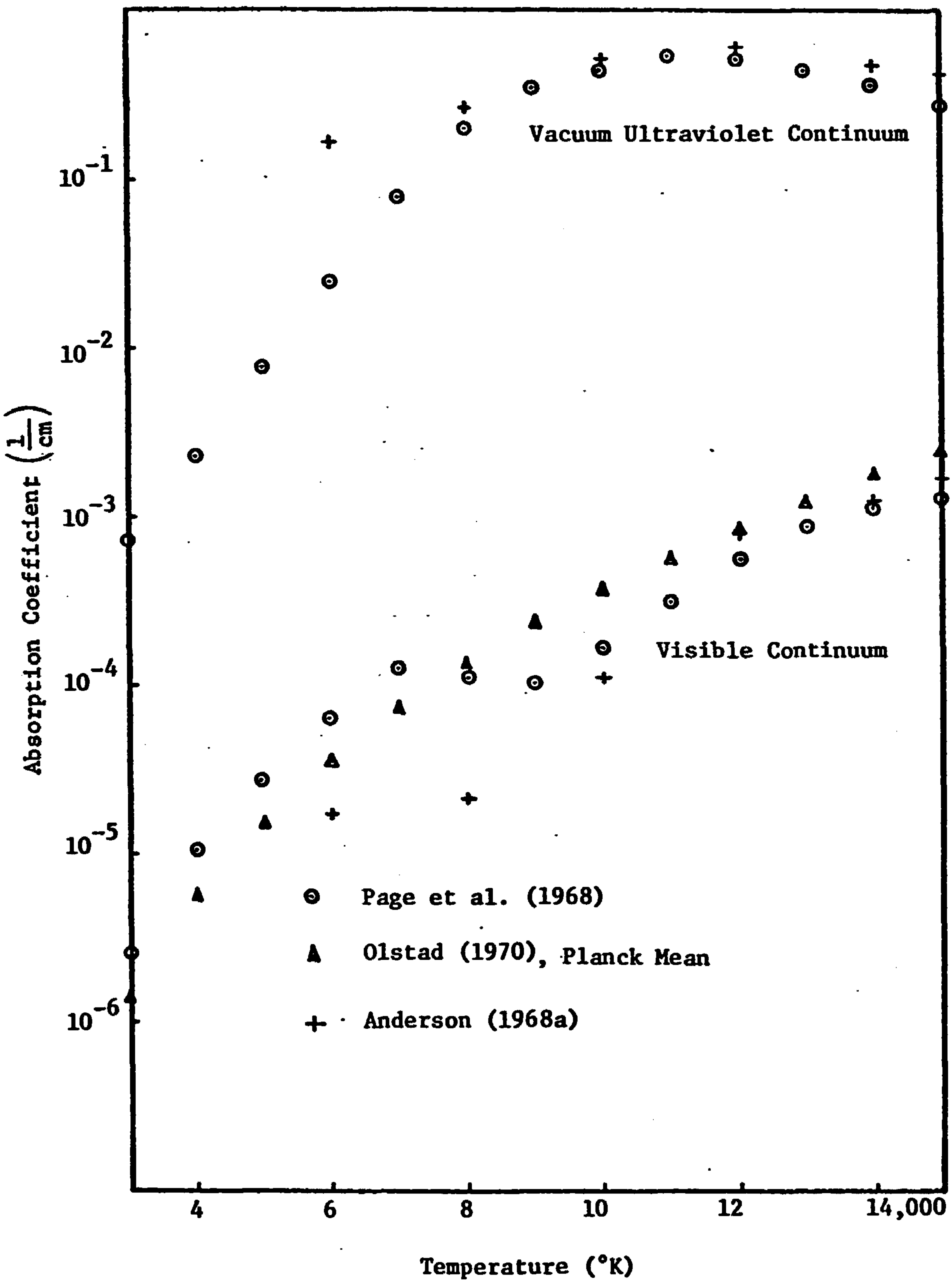

Figure B.7 Absorption Coefficient Comparisons coefficient is very similar to Olstad's Planck mean, and since for a shock temperature of 16,800°K the Planck function integral over the visible continuum makes-up over 94% of the total integral, the differences in the results of the grey and two step calculations are due almost entirely to the vacuum ultraviolet contribution.

Anderson (1968a), using his two step model as shown in Fig. B.7, made extensive comparisons of the total radiative and convective heat transfer to a nonablating wall with the results of Hoshizaki and Wilson (1967) obtained by use of their extremely spectrally detailed continuum absorption coefficient. Anderson found that the radiative flux was within 14% at a nose radius of .5 feet and 5% at a nose radius of two feet. The results for convective heat transfer compared almost identically. These excellent agreements add validity to the Page two step continuum model because of the close comparison of the Page and Anderson models as shown in Fig. B.7.

These arguments are not meant to imply that atomic line contributions are unimportant, but to show that the two continuum steps of Page's model as used in the current analysis is as good as a detailed continuum model. The importance of atomic lines is clearly shown by Anderson (1968b) where he compares the radiative heat transfer to a nonablating wall as computed using Hoshizaki and Wilson's detailed continuum model and Page's two step continuum plus the two steps that account for atomic lines model. This comparison shows that for 200,000 feet and 50,000 feet per second with a nose radius of one foot the Page model gives a 67% increase in wall radiative heat flux. This increase is fairly constant and at a nose radius of six feet reduces to 52%. Since, as argued above, the two step Page continuum model is close to the two step Hoshizaki and Wilson model, the increase in the wall radiative heat flux is due almost entirely to atomic lines.

APPENDIX C

RADIATIVE FLUX AND FLUX DIVERGENCE

In order to understand the physics of radiative gasdynamics it is extremely important to know, at any point in the flow field, each component of the heat flux. This is given by the components of Eq. 3.32 but even for the simplest case of a grey gas numerical techniques are necessary to determine the value of these components. For better visualization of the problem let us make the following definitions:

radiative flux from the gas in the positive direction (toward the body),

$$q_g^{r+} = \sum_{j=1}^{N} \int_{o}^{\tau_j} I_j E_2[N_{Bu}(\tau_j - \tau_j')] d\tau_j'; \qquad \text{C.1}$$

radiative flux from the gas in the negative direction (toward the shock),

$$q_g^{r-} = - \sum_{j=1}^{N} \int_{\tau_j}^{\tau_{j,\Delta}} I_j E_2[N_{Bu}(\tau_j' - \tau_j)] d\tau_j'; \qquad \text{C.2}$$

radiative flux from wall emission in the negative direction,

$$q_{we}^{r-} = -\sum_{j=1}^{N} E_3[N_{Bu}(\tau_{j,\Delta}-\tau_j)]\,\frac{\varepsilon_w}{N_{Bu}}\,I_j(T_w); \qquad \text{C.3}$$

radiative flux from wall reflection in the negative direction,

$$q_{wr}^{r-} = -2(1-\varepsilon_w)\sum_{j=1}^{N} E_3[N_{Bu}(\tau_{j,\Delta}-\tau_j)]\int_0^{\tau_{j,\Delta}} I_j E_2[N_{Bu}(\tau_{j,\Delta}-\tau_j')]d\tau_j'; \qquad \text{C.4}$$

and net conductive flux

$$q_{cond} = -\frac{N_{CR}}{N_{Bu}}\,k\,\frac{dT}{dz}\,. \qquad \text{C.5}$$

Consider now Eq. C.1 and note that the kernel, $E_2[N_{Bu}(\tau_j-\tau_j')]$, is nonseparable. This means that to integrate the equation in the present form would require a complete integration from zero to τ_j for each value of τ_j. That is, one would fix τ_j yielding the kernel only a function of the independent variable, τ_j', and then integrate using some standard technique. For illustrative purposes, we can use an integration scheme that only requires integrand evaluation once at each mesh point. The integration of Eq. C.1 in the present form would then require

$$M(1+M)/2$$

evaluations of the integrand where M is the number of mesh points. If one could separate the kernel by some approximation yielding

$$\int_0^x G(y)F(x,y)dy \simeq F_1(x)\int_0^x G(y)F_2(y)dy,$$

then for the same integration technique that was used on the nonseparable kernel, only M evaluations of the integrand are required. In the current work the step size was 10^{-3} and the shock to interface distance was normalized to one resulting in 1001 mesh points excluding the ablation layer. If we consider 1000 mesh points, the number of integrand evaluations for the nonseparable kernel is 500,500 while the separable kernel approximation reduces this to 1000. Although no direct comparisons of these specific operations were made on computer time requirements, two and a half orders of magnitude increase in the number of times a complicated function subprogram (this is the method used to evaluate $E_n(x)$) is evaluated and the results multiplied is prohibitive. This is especially true if the separable kernel approximation is within the error bounds of the rest of the calculation. An added incentive for using an approximation is that if a higher order accurate integration scheme is used the number of integrand evaluations goes up proportionally, by a factor of four for a fourth order Runge-Kutta. Equation C.2 requires the same solution technique thus doubling the evaluations.

With these considerations in mind, the standard exponential approximation to the exponential integral

$$E_2(x) = a/be^{-bx},$$

where a and b are constants to be picked on the basis of the range of x, was used. Consider an example where

$$x = y - z$$

and z is the dummy variable of integration. The integral could be expressed as

$$\int_o^y F(z)E_2(y-z)dz \simeq a/be^{-by}\int_o^y F(z)e^{bz}dz \ . \qquad \text{C.6}$$

The accuracy of this approximation integral is discussed in Appendix E for $0 \leq y \leq 100$. The accuracy and validity of this approximation are questionable for very large values of $y(y > 100)$. Consider the case where y is the order of 10^3 and b and F(z) are order 1. The integrand of Eq. C.6 ranges from one to e^{10^3} which is approximately 10^{435}. This is too large a number to carry on a CDC 6600 which is limited to the range 10^{-294} to 10^{322}. More important, however, as y gets large (but not exceeding computer capability) the product of the large integral and the very small multiplier, e^{-by}, gives a very inaccurate number of order 1. The same difficulty is encountered when this approximation is applied to Eq. C.2.

A third alternative and the one used in the current work utilizes the exponential approximation but always maintains the argument of the exponential as a difference. That is, the integral is always expressed as

$$\int_o^y F(z)E_2(y-z)dz \simeq a/b \int_o^y F(z)e^{-b(y-z)}dz \ . \qquad \text{C.7}$$

On first consideration this might seem to be no improvement over the earlier evaluations of the integrand, but as shown below a recursion relation can be obtained requiring only one pass through the mesh to evaluate Eq. C.7. Without the exponential approximation as shown in Appendix E, a recursion relation is not possible. With Eq. C.7, consider the case where y is of order 10^3 and b and F(z) are order 1. The integrand of Eq. C.7 only ranges from e^{-by} to 1, thus keeping the numbers in a tenable range.

Let us now define

$$A^j(z) = b/a \int_o^{\tau_j} I_j E_2[N_{Bu}(\tau_j - \tau_j')]d\tau_j'$$

and

$$B^j(z) = b/a \int_{\tau_j}^{\tau_{j,\Delta}} I_j E_2[N_{Bu}(\tau_j' - \tau_j)]d\tau_j' \ .$$

With the exponential approximation these relations become

$$A^j(z) = \int_o^{\tau_j} I_j e^{-bN_{Bu}(\tau_j - \tau_j')} d\tau_j' \qquad \text{C.8}$$

and

$$B^j(z) = \int_{\tau_j}^{\tau_{j,}} I_j e^{-bN_{Bu}(\tau_j' - \tau_j)} d\tau_j' \ .$$

If we now evaluate Eq. C.8 at each mesh point, the discretized relations become

$$A_1^j = 0$$

$$A_2^j = \int_o^{\tau_{j,2}} I_j e^{-bN_{Bu}(\tau_{j,2}-\tau_j')} d\tau_j'$$

$$A_3^j = \int_o^{\tau_{j,3}} I_j e^{-bN_{Bu}(\tau_{j,3}-\tau_j')} d\tau_j'$$

$$= \int_o^{\tau_{j,2}} I_j e^{-bN_{Bu}(\tau_{j,3}-\tau_j)} d\tau_j' + \int_{\tau_{j,2}}^{\tau_{j,3}} I_j e^{-bN_{Bu}(\tau_{j,3}-\tau_j')} d\tau_j' ,$$

and

$$A_4^j = \int_o^{\tau_{j,4}} I_j e^{-bN_{Bu}(\tau_{j,4}-\tau_j')} d\tau_j'$$

$$= \int_o^{\tau_{j,2}} I_j e^{-bN_{Bu}(\tau_{j,4}-\tau_j')} d\tau_j' + \int_{\tau_{j,2}}^{\tau_{j,3}} I_j e^{-bN_{Bu}(\tau_{j,4}-\tau_j')} d\tau_j'$$

$$+ \int_{\tau_{j,3}}^{\tau_{j,4}} I_j e^{-bN_{Bu}(\tau_{j,4}-\tau_j')} d\tau_j' .$$

These relations can be rewritten as

$$A_3^j = A_2^j e^{bN_{Bu}(\tau_{j,2}-\tau_{j,3})} + \int_{\tau_{j,2}}^{\tau_{j,3}} I_j e^{-bN_{Bu}(\tau_{j,3}-\tau_j')} d\tau_j'$$

and

$$A_4^j = A_3^j e^{-bN_{Bu}(\tau_{j,4}-\tau_{j,3})} + \int_{\tau_{j,3}}^{\tau_{j,4}} I_j e^{-bN_{Bu}(\tau_{j,4}-\tau_j')} d\tau_j'$$

or the general relation is

$$A_i^j = A_{i-1}^j e^{-bN_{Bu}(\tau_{j,i}-\tau_{j,i-1})} + \int_{\tau_{j,i-1}}^{\tau_{j,i}} I_j e^{-bN_{Bu}(\tau_{j,i}-\tau_j')} d\tau_j' \,.$$

If we now assume that across each mesh step ($\Delta z = 10^{-3}$) I_j is constant, the general relation can be integrated analytically yielding the recursion relation

$$A_i^j = A_{i-1}^j e^{-bN_{Bu}(\tau_{j,i}-\tau_{j,i-1})} + \frac{I_{j,i-1}}{bN_{Bu}}\left[1-e^{-bN_{Bu}(\tau_{j,i}-\tau_{j,i-1})}\right] \quad \text{C.10}$$

A similar relation for Eq. C.9 is

$$B_{M-\ell}^j = B_{M-\ell+1}^j e^{-bN_{Bu}(\tau_{j,M-\ell+1}-\tau_{j,M-\ell})}$$

$$+ \frac{I_{j,M-\ell}}{bN_{Bu}} \; 1-e^{-bN_{Bu}(\tau_{j,M-\ell+1}-\tau_{j,M-\ell})} \qquad \text{C.11}$$

where M is the total number of mesh points and $i = M-\ell$. The backward recursion relation is necessary because B^j is zero at the body rather than the shock. Once the B^j's are generated and stored, they are recalled just as the A^j's with the forward running subscript "i".

In order to simplify the calculations to come it is convenient to define the following auxiliary variables:

$$X_1^j = N_{Bu}(\tau_{j,\Delta} - \tau_j),$$

$$\frac{dX_1^j}{dz} = -\, N_{Bu}\alpha_j, \qquad \text{C.12}$$

and

$$X_1^j(\Delta) = 0$$

where α_j is the absorption coefficient for the jth frequency group;

$$X_2^j = bN_{Bu}\tau_j,$$

$$\frac{dX_2^j}{dz} = bN_{Bu}\alpha_j, \qquad \text{C.13}$$

and

$$X_2^j\ (0) = 0\ ;$$

and

$$X_3^j = \int_o^{\tau_j} I_j E_2[N_{Bu}(\tau_{j,\Delta} - \tau_j')]d\tau_j'$$

$$\frac{dX_3^j}{dz} = I_j E_2[N_{Bu}(\tau_{j,\Delta} - \tau_j)]$$

$$= I_j E_2(X_1^j)\ , \qquad \text{C.14}$$

and

$$X_3^j(0) = 0.$$

At the beginning of each iteration in the overall problem solution, these three variables are calculated at each mesh point using an

"Improved Euler Predictor-Corrector Integration Method", (McCalla, 1967) and the temperatures from the previous iteration.

By using Eqs. C.10-C.14 we can simplify Eqs. C.1-C.4 to

$$q^{r+}_{g,i} = a/b \sum_{j=1}^{N} A^j_i \; , \tag{C.15}$$

$$q^{r-}_{g,i} = - a/b \sum_{j=1}^{N} B^j_i \; , \tag{C.16}$$

$$q^{r-}_{we,i} = - \sum_{j=1}^{N} E_3(X^j_{1,i}) \frac{\varepsilon_w}{N_{Bu}} I_j(T_w) \; , \tag{C.17}$$

and

$$q^{r-}_{wr,i} = - 2(1-\varepsilon_w) \sum_{j=1}^{N} E_3(X^j_{1,i}) X^j_{3,M} \; . \tag{C.18}$$

A special case of Eq. 3.32 is when z is Δ and this yields Eq. 3.33. The radiative flux that reaches the wall can be computed either by Eq. C.15 evaluated at the wall which is

$$q^{r+}_{g,M} = a/b \sum_{j=1}^{N} A^j_M \tag{C.19}$$

or by

$$X^j_{3,M} = \int_0^{\tau_{j,\Delta}} I_j E_2[N_{Bu}(\tau_{j,\Delta} - \tau'_j)] d\tau'_j \; . \tag{C.20}$$

Since there are no approximations involved to get X^j_3 (this assumes the function subprogram for $E_n(x)$ to be exact), the only errors would arise from the integration routine and these are minimal. Therefore, Eq. C.20 was taken as "exact". It always gave a value lower than Eq. C.19, but the maximum error, which occurred for the most severe condition of maximum enhancement was less than 15%. The error isn't important in the radiative flux calculation because discrete mesh point fluxes are only used for trend information while the $X^j_{3,M}$ value is used to determine the wall mass flux, but the error is important for the radiative flux divergence since the A^j_i's and B^j_i's are also used in those calculations.

With these definitions noted, we can now proceed to the radiative flux divergence. It is this flux divergence as defined by Eq. 3.35 along with convective and conductive terms that describe the energy relations of the shock and ablative layers. Equation 3.35 can be separated into the following parts:

energy absorption due to gas between shock and point of interest,

$$\frac{dq_g^{r+}}{dz} = N_{Bu}\sum_{j=1}^{N}\alpha_j \int_0^{\tau_j} I_j E_1[N_{Bu}(\tau_j-\tau_j')]d\tau_j' \; ; \tag{C.21}$$

energy absorption due to gas between the point of interest and the wall

$$\frac{dq_g^{r-}}{dz} = N_{Bu}\sum_{j=1}^{N} \alpha_j \int_{\tau_j}^{\tau_{j,\Delta}} I_j E_1[N_{Bu}(\tau_j'-\tau_j)]d\tau_j' \; ; \tag{C.22}$$

energy absorption due to emission from the wall

$$\frac{dq_{we}^{r}}{dz} = \sum_{j=1}^{N}\alpha_j E_2[N_{Bu}(\tau_{j,\Delta}-\tau_j)]\varepsilon_w I_j(T_w) \; ; \tag{C.23}$$

energy absorption due to reflection from the wall,

$$\frac{dq^r_{wr}}{dz} = N_{Bu}\sum_{j=1}^{N}\alpha_j E_2[N_{Bu}(\tau_{j,\Delta}-\tau_j)]2(1-\epsilon_w\int_o^{\tau_{j,\Delta}} I_j E_2[N_{Bu}(\tau_{j,\Delta}-\tau_j')]d\tau_j' \; ; \tag{C.24}$$

and energy emission from point of interest,

$$\frac{dq^r_e}{dz} = 2\sum_{j=1}^{N}\alpha_j I_j \; . \tag{C.25}$$

With the exponential approximation, Eq. C.21 becomes

$$\frac{dq^{r+}_g}{dz} = aN_{Bu}\sum_{j=1}^{N}\alpha_j\int_o^{\tau_j} I_j e^{-bN_{Bu}(\tau_j-\tau_j')}d\tau_j'$$

and Eq. C.22 becomes

$$\frac{dq^{r-}_g}{dz} = aN_{Bu}\sum_{j=1}^{N}\alpha_j\int_{\tau_j}^{\tau_{j,\Delta}} I_j e^{-bN_{Bu}(\tau_j'-\tau_j)}d\tau_j' \; .$$

By utilizing Eqs. C.8 and C.9 we have

$$\frac{dq^{r+}_g}{dz} = aN_{Bu}\sum_{j=1}^{N}\alpha_j A^j \tag{C.26}$$

and

$$\frac{dq^{r-}_g}{dz} = aN_{Bu}\sum_{j=1}^{N}\alpha_j B^j \; . \tag{C.27}$$

With Eqs. C.12 and C.13, we can simplify Eqs. C.23 and C.24 to

$$\frac{dq^r_{we}}{dz} = \sum_{j=1}^{N} \alpha_j E_2(X_1^j)\varepsilon_w I_j(T_w) \tag{C.28}$$

and

$$\frac{dq^r_{wr}}{dz} = N_{Bu}\sum_{j=1}^{N} \alpha_j E_2(X_1^j)2(1-\varepsilon_w)X^j_{3,M} \; . \tag{C.29}$$

Now we can use Eqs. C.25-C.29 to completely define the radiative flux divergence of Eq. 4.8 as

$$\left(\frac{\partial q}{\partial z}\right)_i = \sum_{j=1}^{N} \alpha_{j,i}\Big[2I_{j,i} - aN_{Bu}(A_i^j + B_i^j) - E_2(X^j_{1,i})\varepsilon_w I_j(T_w) - N_{Bu}E_2(X^j_{1,i})2(1-\varepsilon_w)X^j_{3,M}\Big] \; . \tag{C.30}$$

In addition to making-up the terms of Eq. C.30 for temperature update through the energy equation, Eqs. C.25-C.29 are used to compute the individual components of the radiative flux divergence. These components are then used in further understanding the physics of the problem under consideration.

APPENDIX D

IMPLICIT SOLUTION TECHNIQUE

The energy equation, which is to be solved by the implicit technique, is given by Eq. 4.8 and for reference is repeated here as

$$\frac{T_i^{n+1} - T_i^n}{\Delta t} = \frac{1}{2N_{Pe}(\Delta z)^2}\left[\left(k_i^n + k_{i+1}^n\right)\left(T_{i+1}^{n+1} - T_i^{n+1}\right)\right.$$

$$\left. - \left(k_i^n + k_{i-1}^n\right)\left(T_i^{n+1} - T_{i-1}^n\right)\right] - \left(\frac{\partial h}{\partial T}\right)_i^n \frac{(\rho v)_i^n}{2(\Delta z)}\left(T_{i+1}^{n+1} - T_{i-1}^{n+1}\right) - \Gamma\left(\frac{\partial q}{\partial z}\right)_i^n . \tag{D.1}$$

By treating the gas properties, equation of state, and nonlinear term (radiative flux divergence) explicitly, Eq. D.1 can be rewritten as

$$A_i^n\, T_{i-1}^{n+1} + B_i^n\, T_i^{n+1} + C_i^n\, T_{i+1}^{n+1} = D_i^n \tag{D.2}$$

where

$$A_i^n = \frac{\Delta t}{2(\Delta z)}\left[\frac{\left(k_i^n + k_{i-1}^n\right)}{Pe(\Delta z)} + \left(\frac{\partial h}{\partial T}\right)_i^n (\rho v)_i^n\right],$$

$$B_i^n = -\left[1 + \frac{\Delta t(k_{i+1}^n + 2k_i^n + k_{i-1}^n}{2Pe(\Delta z)^2}\right], \tag{D.3}$$

$$C_i^n = \frac{\Delta t}{2(\Delta z)}\left[\frac{\left(k_i^n + k_{i+1}^n\right)}{Pe(\Delta z)} - \left(\frac{\partial h}{\partial T}\right)_i^n (\rho v)_i^n\right],$$

and

$$D_i^n = \Delta t\Gamma\left(\frac{\partial q}{\partial z}\right)_i^n - T_n \ .$$

We can now write Eq. D.2 for each interior mesh point yielding M-2 linear equations where M is the total number of mesh points. Since the end points are fixed (the temperature at the shock is known from the Rankine-Hugoniot relations and the temperature at the wall is fixed by the material sublimation temperature at the shock pressure), the M-2 equations are in terms of the M-2 unknowns $T_2^{n+1} \rightarrow T_{M-1}^{n+1}$. After expansion of Eq. D.2 we have

$$\begin{aligned}
&B_2T_2 + C_2T_3 && = D_2' - A_2T_1 \\
&A_3T_2 + B_3T_3 + C_3T_4 && = D_3 \\
&\cdots\cdots\cdots\cdots\cdots\cdots && \\
&A_iT_{i-1} + B_iT_i + C_iT_{i+1} && = D_i \qquad\qquad \text{D.4} \\
&\cdots\cdots\cdots\cdots\cdots\cdots &&
\end{aligned}$$

$$A_{M-2}T_{M-3} + B_{M-2}T_{M-2} + C_{M-2}T_{M-1} = D_{M-2}$$

$$A_{M-1}T_{M-2} + B_{M-1}T_{M-1} = D'_{M-1} - C_{M-1}T_M$$

where the time step superscripts n and n+1 have been dropped and the right-hand side of each equation is a known constant for each time step. The matrix of coefficients A,B, and C is known as a tridiagonal matrix and can be solved by a Gaussian elimination method (Carnahan, et al., 1969, pp 270-272). Note that we have modified the definition of D_2 and D_{m-1} as follows

$$D_2 = D'_2 - A_2T_1$$

and (D.5)

$$D_{M-1} = D'_{M-1} - C_{M-1}T_M \quad .$$

Let us now postulate a recursion relation in the form

$$T_i = \gamma_i - \frac{C_iT_{i+1}}{\beta_i} \qquad \text{D.6}$$

where the constants β_i and γ_i are to be determined (Carnahan, et al., 1969, p 441). Substitution of this expression into the first term of the ith equation of Eq. D.4 yields

$$A_i\left(\gamma_{i-1} - \frac{C_{i-1}}{B_{i-1}}T_i\right) + B_iT_i + C_iT_{i+1} = D_i .$$

Upon solving for T_i we have

$$T_i = \frac{\left(D_i - A_i\gamma_{i-1}\right) - C_iT_{i+1}}{B_i - \frac{A_iC_{i-1}}{\beta_{i-1}}}$$

which verifies the postulation of Eq. D.6 if

$$\beta_i = B_i - \frac{A_iC_{i-1}}{\beta_{i-1}}$$

and D.7

$$\gamma_i = \frac{D_i - A_i\gamma_{i-1}}{\beta_i} \; .$$

The end points must be treated individually and substitution into the first of Eq. D.4 shows

$$\beta_2 = B_2$$

and D.8

$$\gamma_2 = D_2/\beta_2$$

while substitution into the last of Eq. D.4 yields

$$T_{M-1} = \gamma_{M-1} \; . \qquad \text{D.9}$$

Now the solution proceeds by solving Eq. D.8 for β_2 and γ_2, then marching forward through the mesh with Eq. D.7 to determine the remaining β's and γ's. At the end of the mesh T_{M-1} is determined from Eq. D.9 and then the mesh is traversed backwards with Eq. D.6 yielding all updated temperatures.

A disadvantage of the Gaussian elimination method of solving the tridiagonal matrix is that round-off error may accumulate seriously. With this in mind Douglas (1959) has conducted an analysis of this scheme and concludes the round-off error will be small in comparison to the discretization error for typical choices of Δz and Δt. For some cases considered during the current analysis, many iterations (the order of 10^3) were required for a steady-state solution. To evaluate the existence of cumulative errors, converged solutions were used as inputs to restart a problem and in every case convergence was achieved at one or two iterations and this converged data was undistinguishable from the 10^3 iteration converged data. From this result one can conclude that cumulative errors are small and well within the overall analysis accuracy. For additional discussion of discretization error and comparative computer time requirements for implicit and explicit techniques see Carnahan, et al., (1969, pp 440-448) and Richtmyer and Morton (1967, pp 198-201).

APPENDIX E

EXPONENTIAL INTEGRAL APPROXIMATIONS

Consider the problem of determining

$$A(x) = \int_{o}^{x} B^{4}(y)E_{1}(x-y)dy \qquad \text{E.1}$$

where $0 \leq x \leq 100$,

$$E_{n}(z) = \int_{o}^{1} e^{-z/\mu}\mu^{n-2}du,$$

the exponential integral, and

$$E_{n-1}(z) = -\frac{dE_{n}(z)}{dz} \quad . \qquad \text{E.2}$$

Throughout this work, the "exact" exponential integral values are determined by a function subprogram based on algorithms given in Sections 5.1.14, 5.1.53 and 5.1.56 of *Handbook of Mathematical Functions with Formulas, Graphs, and Mathematical Tables*, U.S. Department of Commerce, National Bureau of Standards, Applied Mathematics Series No. 55, 1964. Equation E.1 was chosen because of its similarity to the divergence of the radiative flux due to gas between the shock and point of interest term in the energy equation. Consider, for purposes of discussion

$$B(y) = (1-y^2)^{\frac{1}{2}} \qquad \text{E.3}$$

which is a quarter circle and is the simplest approximation to the shape of the temperature profile between the shock and the interface. We will now solve Eq. E.1 with Eq. E.3 by three methods of approximation and compare the results.

The first method is considered the "exact" method and involves a sum of integrals over many small steps in x. The method would be truly exact in the limit $\Delta x \rightarrow 0$. Equation E.1 becomes

$$A(x_n) = \int_{x_1}^{x_2} B^4 E_1(x_n-y)dy + \int_{x_2}^{x_3} B^4 E_1(x_n-y)dy + \text{----} + \int_{x_{n-1}}^{x_n} B^4 E_1(x_n-y)dy.$$

If we now assume that the step size is small enough that over one step in x, B^4 is constant, we have

$$A(x_n) = B_1^4[E_2(x_n-x_2) - E_2(x_n-x_1)] + B_2^4[E_2(x_n-x_3)-E_2(x_n-x_2)]$$

$$+ \text{----} + B_{n-1}^4[E_2(0) - E_2(x_n-x_{n-1})]$$

$$= B_{n-1}^4 - B_1^4 E_2(x_n-x_1) + \sum_{k=2}^{n-1} E_2(x_n-x_k)(B_{k-1}^4-B_k^4) \quad . \qquad \text{E.4}$$

The important factor to note here is that there is no recursion relation possible from Eq. E.4; that is, the general term requires a summation from 2 to n-1 for each n and A_{n-1} can not be used to obtain A_n. Since A_1 is zero as can be seen from Eq. E.1, the solution of Eq. E.4 requires

$$M(M-1)/2$$

evaluations of the exponential integral where M is the total number of mesh points. For a few mesh points this would be no great problem and one could use the "exact" technique given by Eq. E.4, but in the current analysis where $M > 1000$ the computer time becomes prohibitive. In addition to each evaluation of the exponential integral, the source function, B, must be raised to the fourth power and multiplied the same number of times.

The second method involves the approximation

$$E_1(z) \simeq ae^{-bz} \qquad \text{E.5}$$

where the constants a and b are chosen through various considerations and the other E_n- functions are taken such that Eq. E.2 is satisfied. If one matches the area and first moment of the exact and approximate expressions for $E_2(z)$, the result is $a = 9/8$ and $b = 3/2$, but other methods lead to different values (Vincenti and Baldwin, 1962). Throughout the current analysis the values of $a = b = \sqrt{3}$ were used. These values give acceptable accuracy (Vincenti and Kruger, 1965, p 483) and with $a = b$ they conveniently cancel in many cases of interest. With

Eq. E.5 substituted into Eq. E.1 we have

$$A(x) = a\int_0^x B^4 e^{-b(x-y)} dy \qquad \text{E.6a}$$

$$= ae^{-bx}\int_0^x B^4 e^{by} dy \ . \qquad \text{E.6b}$$

Let us now define a new variable given by

$$C(x) = \int_0^x B^4 e^{by} dy$$

which can be determined by any standard technique. Now Eq. E.6b becomes

$$A(x) = as^{-bx}C(x)$$

or in discretised form

$$A(x_n) = ae^{-bx_n}C(x_n) \ . \qquad \text{E.7}$$

As pointed-out in Appendix C, the problem with this second method, in addition to the exponential approximation to the exponential integral, is that in computer calculations errors are introduced for large values of bx_n and when e^{-bx_n} goes below 10^{-294} the problem cannot be carried by a CDC 6600 computer.

The third method follows directly from Eq. E.6a if we integrate over each space step as follows

$$A(x_1) = 0$$

$$A(x_2) = a\int_{x_1}^{x_2} B^4 e^{-b(x_2-y)}\,dy$$

$$A(x_3) = a\int_{x_1}^{x_2} B^4 e^{-b(x_3-y)}\,dy + a\int_{x_2}^{x_3} B^4 e^{-b(x_3-y)}\,dy\ .$$

The recursion relation is seen to be

$$A(x_3) = A(x_2)e^{-b(x_3-x_2)} + a\int_{x_2}^{x_3} B^4 e^{-b(x_3-y)}\,dy$$

or in general

$$A(x_n) = A(x_{n-1})e^{-b(x_n-x_{n-1})} + a\int_{x_{n-1}}^{x_n} B^4 e^{-b(x_n-y)}\,dy\ . \qquad \text{E.8}$$

If we now as in the first method assume B^4 to be constant over one space step, we can perform the integration analytically yielding

$$A(x_n) - A(x_{n-1})e^{-b(x_n-x_{n-1})} + \frac{a}{b}\,B_{n-1}^4\left(1-e^{-b(x_n-x_{n-1})}\right). \qquad \text{E.9}$$

Although we have made the exponential approximation to the exponential integral in arriving at Eq. E.9, the major advantage of this method over the second method is that the exponents of exponentials are differences. This allows us to go to extremely large values of x_n and still remain within the numerical range of computer algorithms.

A comparison of methods one and three is given in Figs. E.1-E.3. Although the accuracy of method three, using method one as "exact", isn't very good for small values of the argument x, it was determined that in the complete problem the argument is sufficiently large, in regions where terms like Eq. E.1 are important, that the third method is sufficient. This judgment is also made in part by consideration of the prohibitive computer time required to incorporate method one into the complete problem. Also shown in Figs. E.1-E.3 are the results of method two calculations. Under the same assumptions used to arrive at Eq. E.9, method two would give the same results as method three, but the calculations were performed using a centered trapezoidal rule integration technique. At the smaller values of x the difference between methods two and three is due primarily to the rather inaccurate trapezoidal rule integration, but at large values of x the additional inaccuracy of multiplying very large numbers by very small numbers is coming into consideration.

A much better comparison of methods two and three is shown in Fig. E.4. This figure shows results of converged solutions to the complete grey-gas problem. In addition to deviating from the value of wall mass flux predicted by method three by 17%, at absorption enhancements greater than 9×10^6 method two generated numbers outside the range 10^{-294} to 10^{322} which is the limit of a CDC 6600.

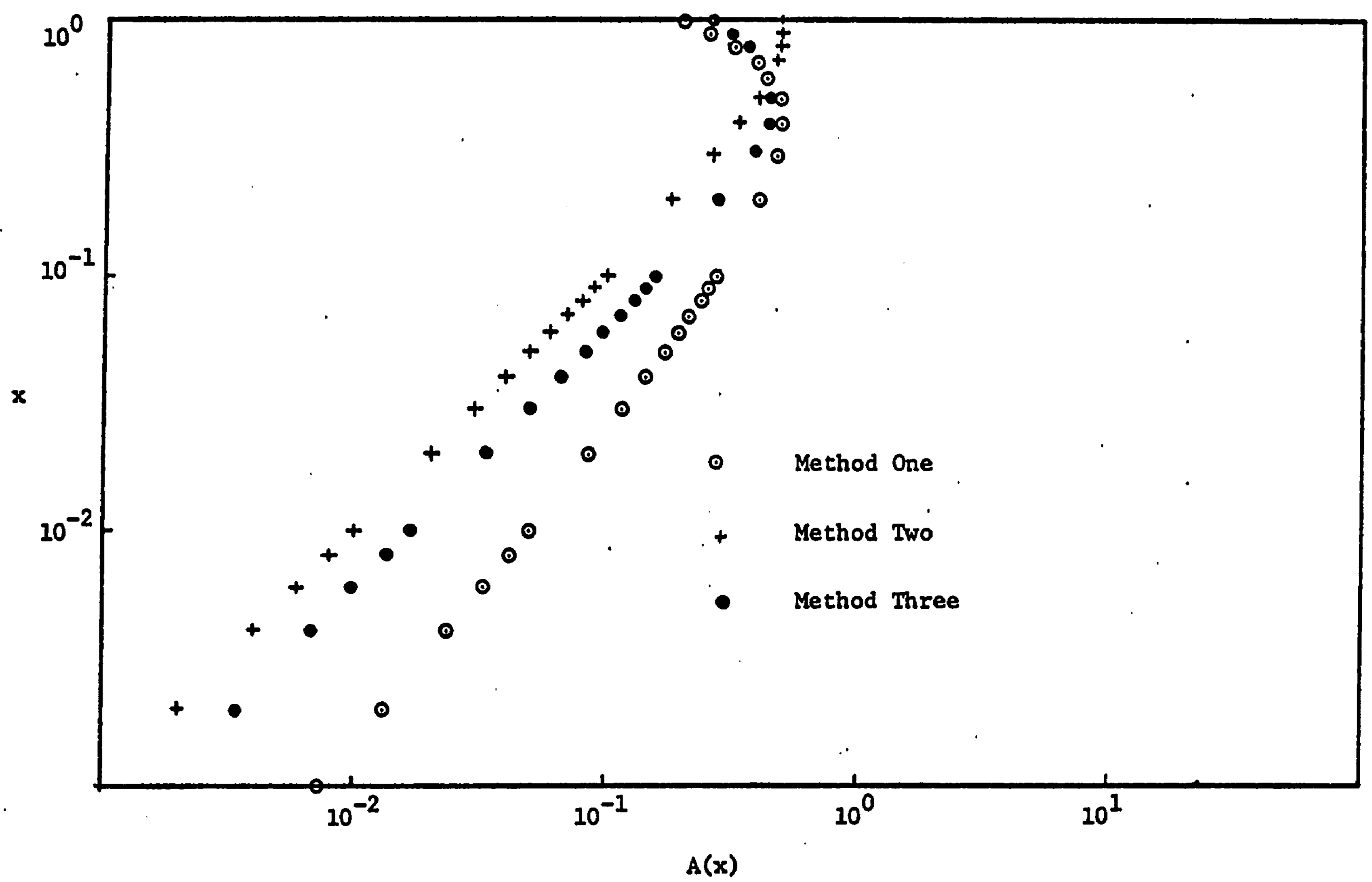

Figure E.1 Approximation Comparisons

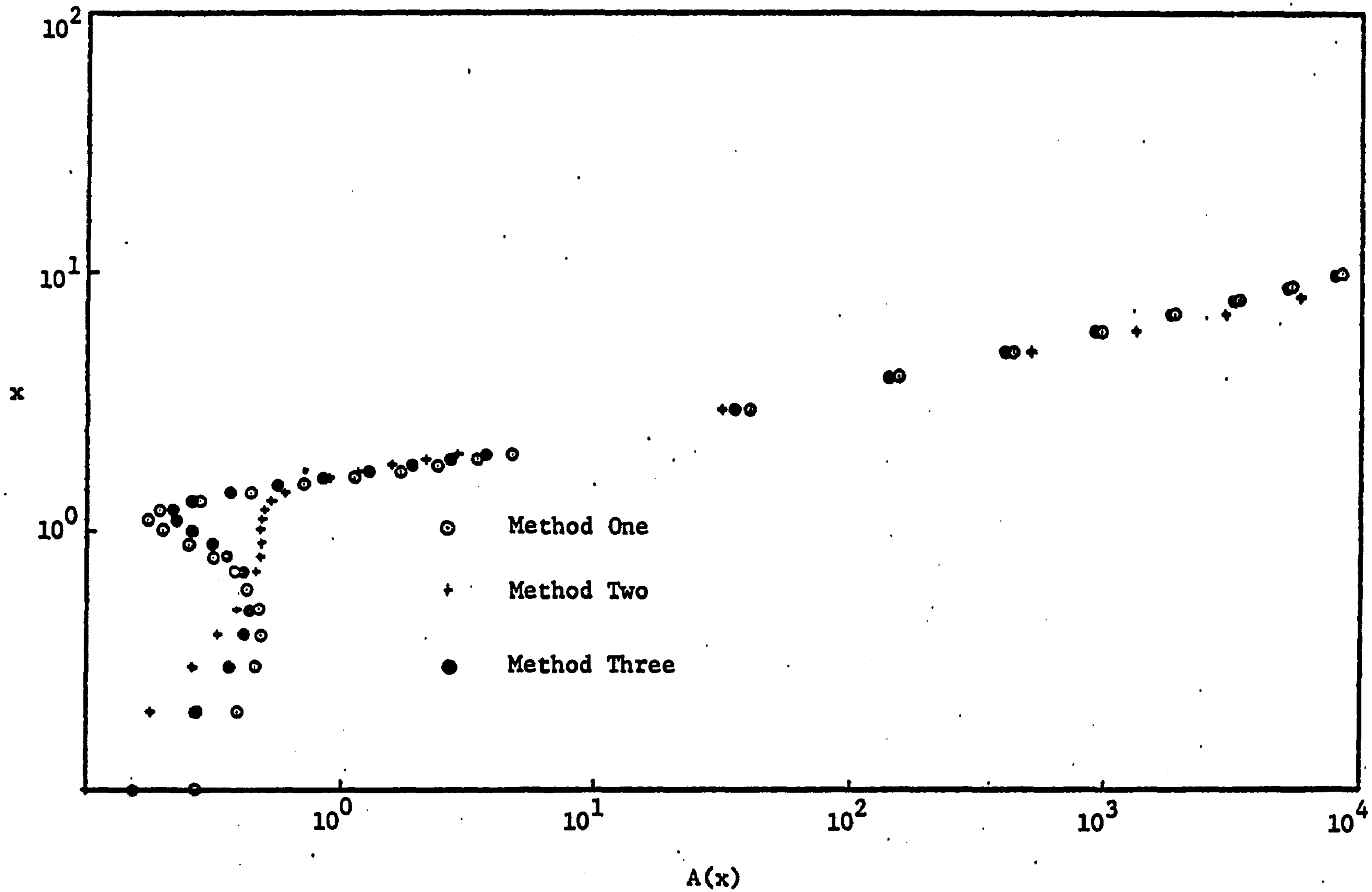

Figure E.2 Approximation Comparisons (continued)

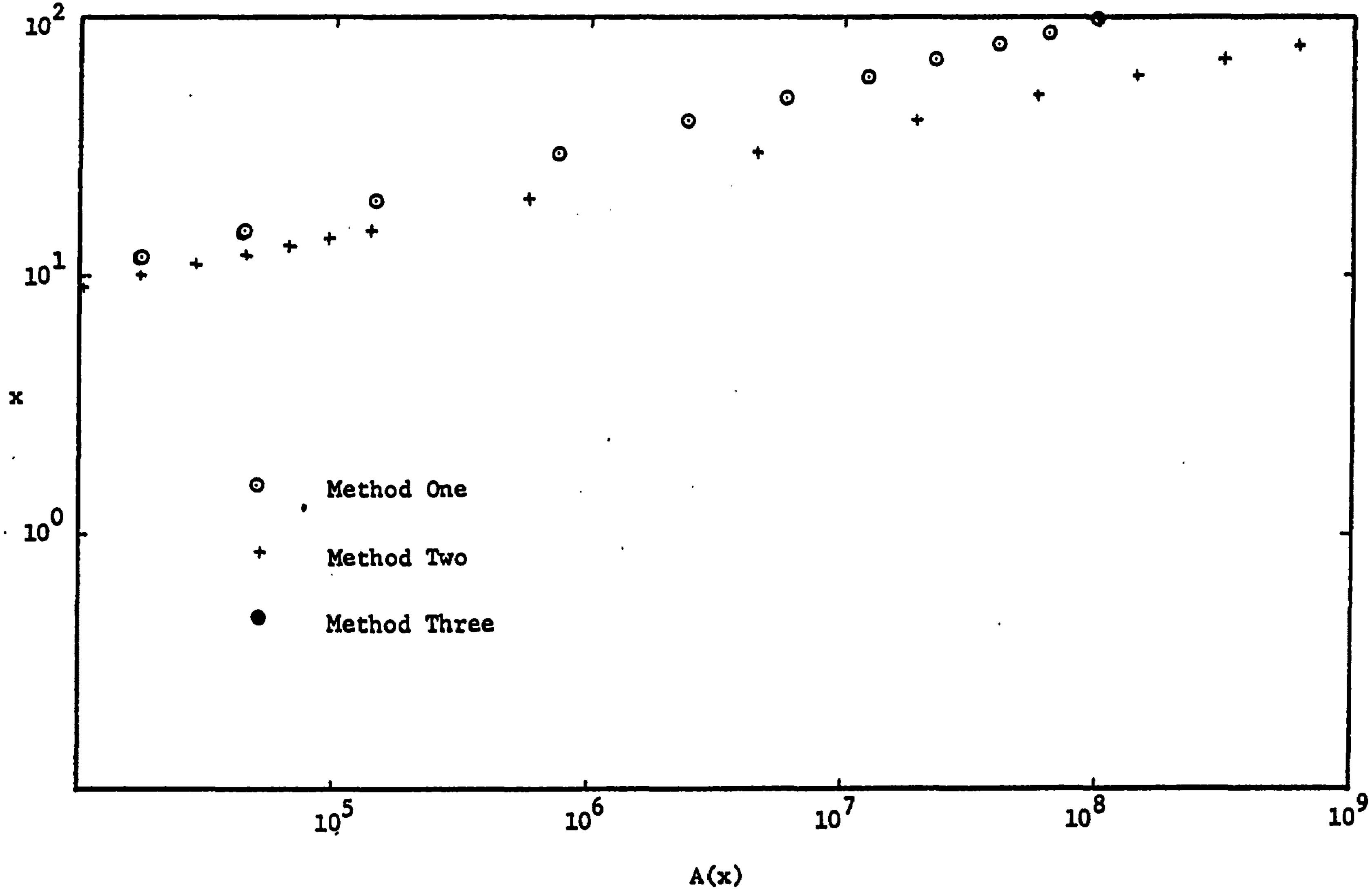

Figure E.3 Approximation Comparisons (continued)

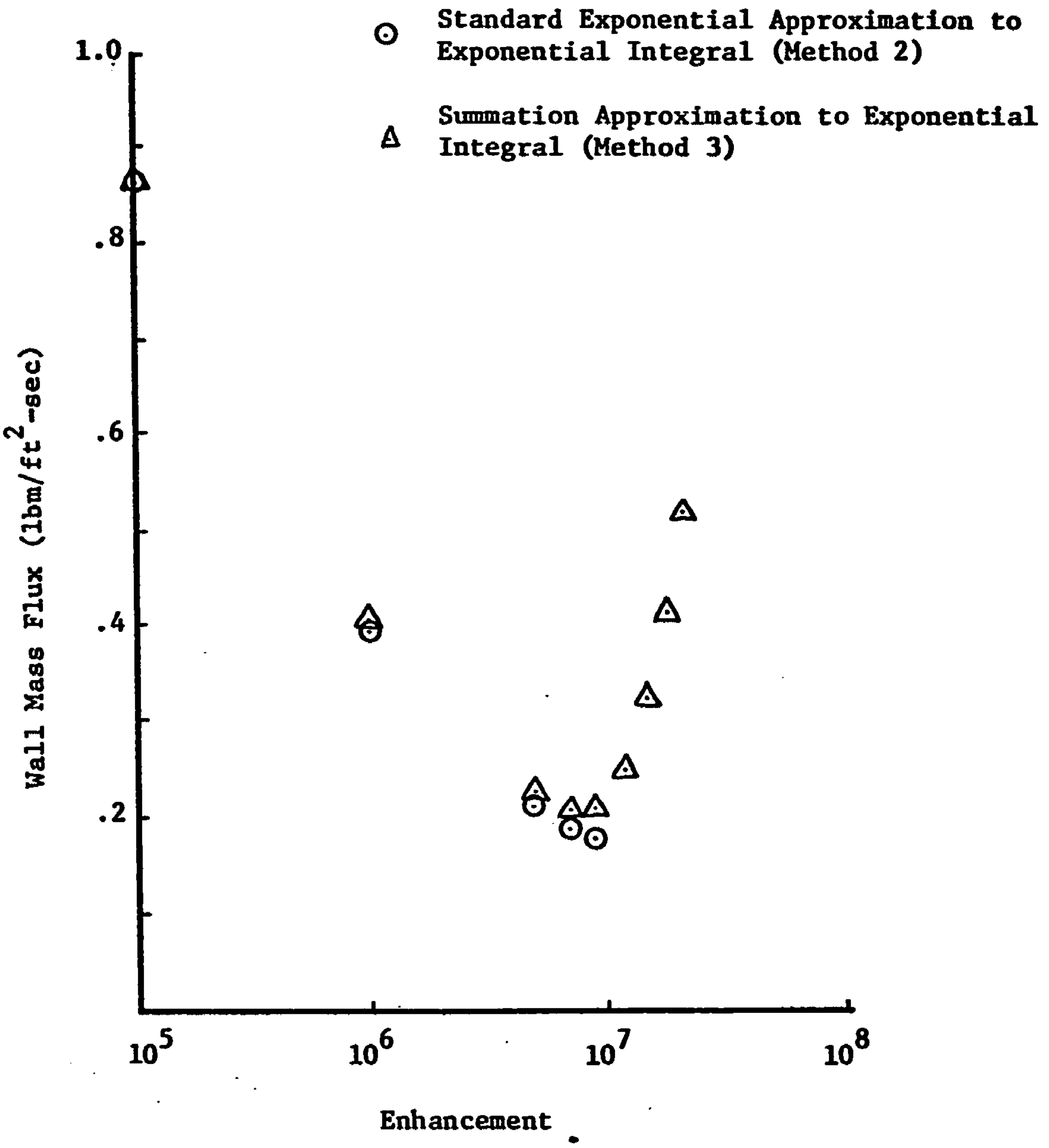

Figure E.4 Exponential Integral Approximation Comparisons

APPENDIX F

THE CODE

The computer program used in the calculations of this analysis is listed below. In order to start a calculation one simply specifies the flight and surface conditions, absorption coefficient model and cut-off frequencies, and an initial guess of temperature profile and mass loss rate. Additional options such as convergence criterion for the integration algorithm, convergence criterion for the iteration on the energy equation, degree of enhancement and selection of frequency range to enhance are available and were in general exercised.

```
      PROGRAM TIME(INPUT,OUTPUT,PUNCH,FILHPR,TAPE2=FILHPR)
      EXTERNAL FCT1,OUTP1,FCT2,OUTP2
      DIMENSION DIVQ(2000), A(2000), B(2000), C(2000), D(2000), DIVQP(20
     100)
      DIMENSION FN(2000), PRMT(5), X(11), DERX(11), QZ(2000)
      DIMENSION P(2000), QRPZ(2000), QRMZ(2000), QRRMZ(2000), QCONZ(2000
     1)
      DIMENSION DQCO(2000), DQCV(2000), DQRL(2000), DQRR(2000), FT(2000)
      DIMENSION DQRM(2000), DQRE(2000), DQS(2000)
      DIMENSION ASUM(2000), BSUM(2000)
      COMMON /AA/ XA(3,2000,2),T(2000)
      COMMON /BB/ IHLF,AN(10)
      COMMON /B/ DI,VI,DH,RN,DRS,DELS,DELT,DY,TW,ALPPS,PS
      COMMON /C/ HW
      COMMON /D/ THICK,JS,AC,BC,BU,TS
      COMMON /E/ NCOEF
      COMMON /F/ AN1,AN2,AN3,INF
C     SET FLIGHT CONDITIONS, VI IN FPS, ALT IN FT.
      DATA DIODSL,VI,ALT/.00035,5.5E04,1.9E05/
C     SET SURFACE CONDITIONS.  UNITS, FT, DR, BTU/LBM
      DATA RN,TW,HEFF/1.,5400.,2200./
C     SPECIFY CONSTANTS.  UNITS, LBM/FT3, BTU/FT2-SEC-DR4
      DATA DSL,SIG/.0804,4.761111E-13/
C     SPECIFY COEFFICIENTS FOR EXPO. APPROX. (E1(X)=A EXP(-B X))
      DATA AC,BC/1.732,1.732/
C
C     DEFINE FUNCTION STATEMENTS.  T IN DR,  P IN ATM.
C
C     ENTHALPY AT 1 ATM.
      HFA1(X)=33.85*(X/556.)**1.819
C     PRESSURE CORRECTION FOR HFA1
      PCORH(Y)=Y**(-.1635)
C     DENSITY RATIO TO SEA LEVEL AT 1 ATM.
      DODSL(X)=7.944*(X/556.)**(-1.819)
C     PRESSURE CORRECTION FOR DODSL
      PCORD(Y)=Y**1.1235
C     PLANCK MEAN ABSORPTION COEFFICIENTAT IN 1/FT
      ALPP(X,Y)=1.191334E-09*(X/556.0)**(4.631-.1896*ALOG(Y))*Y**(1.9685
     1-.174*ALOG(Y))
C      SET INITIAL CONDITIONS FOR SPECIFIED TEMPERATURE PROFILE
      READ 61, ICON,IHLFR,AMDJ,HEFF,DELT,DIODSL,VI,RN,THICK
C     SET FREQUENCY BAND LIMITS
      AN(1)=0.
      AN(2)=3./1.13*1.E+15
      AN(3)=1.E+20
C     SET COUNTERS
      ICON=1
      IREAD=1
      IREAD=0
      MFI=0
      MFI=1
      MFIX=MFI
      IPQ=0
      IPQ=1
      IPDQ=0
      IPDQ=1
      IURIKA=0
      MR=0
      MR=1
      IP=20
      IP=10
      IP=150
      IP=100
      IP=1
```

```
      IP=1
      IP=50
      IIP=IP
      NDIM=2000
      NIT=0
C     SET NUMBER OF STEPS IN ABS. COEF. MODEL AND WALL EMISSIVITY
      JS=2
      EPSW=1.
C     SET FREE STREAM DENSITY
      DI=DIODSL*DSL
C     SET REMAINING SHOCK AND WALL CONDITIONS
      TS=1.678E03*(DIODSL)**.09*(VI*1.E-03/3.28)**1.28
C     DR
      DRS=6.5E-02*DIODSL**.04*(VI*1.E-03/3.28)**.08
      PS=.147*(TS/556.)**1.815*((1./DRS)*DIODSL)**.99
C     ATM.
      DW=DODSL(TW)*PCORD(PS)*DSL
C     LBM/FT3
C     LBM/FT2-SEC, UNITS ON AMDU
      VW=AMDU/DW
C     FT/SEC
      HS=HFA1(TS)*PCORH(PS)
C     BTU/LBM
      ALPPS=ALPP(TS,PS)
C     1/FT
      DSVS=DIODSL*DSL*VI
C     LBM/FT2-SEC
C     SET COEF. IN THREE SUBPROGRAMS AND GET WALL THERMAL CONDUCTIVITY.
      NCOEF=0
      COEF1=DHDTH(1.,TW,1)
      AKW=TCON(1.,TW,TS)
      COEF3=ALP(1,1.,1.,TW,1.,1)
C     CALCULATE SHOCK STAND OFF DISTANCE,  IN FT.
      DELS=DRS*RN/(1.+(2.*DRS*(1.-DRS))**.5)
C
C     CALCULATE NONDIMENSIONAL NUMBERS
C
C     PECLET NUMBER
      PE=DELS*DSVS*HS/(AKW*TS)
C     RADIATION NUMBER
      GAMMA=2.*ALPPS*DELS*SIG*TS**4/(DSVS*HS)
C     BOLTZMANN NUMBER
      BO=DSVS*HS/(2.*SIG*TS**4)
C     BOUGUER NUMBER
      BU=ALPPS*DELS
C     CONDUCTION RADIATION NUMBER
      CR=BO/PE
      DY=.001
      AKST=TCON(1.,TW,TS)
      DT=1.
      DT=5.E-03
      DT=.1
      DT=1.E-02
      DT=1.E-03
      DT=5.E-04
      DT=1.E-05
      DELT=1.+RN/DELS*VW/VI*(DW/(2.*DI))**.5
      IHLF=DELT/DY+1
      IF (IHLF.LT.2001) GO TO 1
      PRINT 55, IHLF,DELT,NIT
      CALL EXIT
    1 ISTOP=IHLF-1
      Y=0.
    2 DO 3 I=1,IHLFR,10
      READ 54, (T(I-1+K),K=1,10)
    3 CONTINUE
```

```
      IHLF=IHLFR
C     NORMALIZED HEFF
      HEFFT=HEFF/(HS*GAMMA)
      QNORM=2.*BU*SIG*TS**4
4     IF (NIT.NE.0) GO TO 6
5     PMB=DH*VH**2/(DI*VI**2)
      BUH=ALPP(TH,PS)*(DELT-1.)*DELS*THICK
C     PRINT INITIAL CONDITIONS
      PRINT 48, TH,AKH,DI,VI,DH,DELS,ALT,DIODSL,RN,HEFF,VH,TS,DRS,PS,DH,
     1HS,ALPPS,DSVS,PE,GAMMA,BO,BU,CR,AKST,DY,DT,PMB,QNORM,BUH
      PRINT 57, JS,DELT,AMDU,EPSH,IHLF,THICK,IHLFR
      WRITE (2,48) TH,AKH,DI,VI,DH,DELS,ALT,DIODSL,RN,HEFF,VH,TS,DRS,PS,
     1DH,HS,ALPPS,DSVS,PE,GAMMA,BO,BU,CR,AKST,DY,DT,PMB,QNORM,BUH
      WRITE (2,57) JS,DELT,AMDU,EPSH,IHLF,THICK,IHLFR
      IF (IURIKA.EQ.1) GO TO 44
6     CONTINUE
      PRMT(1)=0.
      PRMT(2)=DELT
      PRMT(3)=DY
      PRMT(4)=1.E-03
      DO 7 J=1,JS
7     X(J)=0.
      N=1
      CALL EIPC (PRMT,X,DERX,JS,IHLF,FCT1,OUTP1,N)
      IF (PRMT(5)) 8,9,8
8     PRINT 50
      CALL EXIT
9     PRMT(1)=(IHLF-1)*DY
      PRMT(2)=0.
      PRMT(3)=-DY
      NE=2*JS
      DO 10 J=1,NE
10    X(J)=0.
      N=1
      CALL EIPC (PRMT,X,DERX,NE,IHLF,FCT2,OUTP2,N)
      IF (PRMT(5)) 11,12,11
11    PRINT 50
      CALL EXIT
12    CONTINUE
      BIG=0.
      IG=1
      ISTOP=IHLF-1
      P(1)=1.
      P(IHLF)=TH/TS
      QRH=0.
      DO 13 I=1,IHLF
      DQRL(I)=0.
      DQRR(I)=0.
      DQRH(I)=0.
      DQRE(I)=0.
      QRPZ(I)=0.
      QRMZ(I)=0.
13    QRRHZ(I)=0.
      INF=0
      DO 18 J=1,JS
      IF (J.EQ.JS) INF=1
      ASUM(1)=0.
      BSUM(IHLF)=0.
      DO 14 I=2,IHLF
      POH=XA(2,I-1,J)-XA(2,I,J)
      ASUM(I)=ASUM(I-1)*EXP(POH)+PLKI(T(I-1),TS,AN(J),AN(J+1),INF,0)*(1.
     1-EXP(POH))
      L=IHLF-I+1
      POH=XA(2,L,J)-XA(2,L+1,J)
14    BSUM(L)=BSUM(L+1)*EXP(POH)+PLKI(T(L),TS,AN(J),AN(J+1),INF,0)*(1.-E
     1XP(POH))
```

```
      Y=0.
      DO 15 I=1,IHLF
      PLKCKH=PLKI(T(IHLF),TS,AN(J),AN(J+1),INF,0)
      ASUM(I)=ASUM(I)*AC/BC
      BSUM(I)=BSUM(I)*AC/BC
      QRPZ(I)=QRPZ(I)+ASUM(I)/BC/BU
      QRMZ(I)=QRMZ(I)-BSUM(I)/BC/BU
      QRRHZ(I)=QRRHZ(I)-E(3,XA(1,I,J))*(EPSH/BU*PLKCKH+2.*(1.-EPSH)*XA(3
     1,1,J))
      ALPCK=ALP(J,Y,T(I),TS,THICK,JS)*GAMMA
      DQRL(I)=ALPCK*ASUM(I)+DQRL(I)
      DQRR(I)=ALPCK*BSUM(I)+DQRR(I)
      DQRH(I)=DQRH(I)+ALPCK*E(2,XA(1,I,J))*(EPSH*PLKCKH+2.*(1.-EPSH)*BU*
     1XA(3,1,J))
      DQRE(I)=DQRE(I)-ALPCK*2.*PLKI(T(I),TS,AN(J),AN(J+1),INF,0)
15    Y=Y+DY
      IF (IP.NE.IIP) GO TO 18
      WRITE (2,65) J,JS
      DO 16 I=1,IHLF,10
      L=I-1
      WRITE (2,58) I,(QRPZ(L+K),K=1,10)
      WRITE (2,59) (QRMZ(L+K),K=1,10)
      WRITE (2,59) (QRRHZ(L+K),K=1,10)
16    WRITE (2,67)
      WRITE (2,66)
      DO 17 I=1,IHLF,10
      L=I-1
      WRITE (2,58) I,(DQRL(L+K),K=1,10)
      WRITE (2,59) (DQRR(L+K),K=1,10)
      WRITE (2,59) (DQRH(L+K),K=1,10)
      WRITE (2,59) (DQRE(L+K),K=1,10)
17    WRITE (2,67)
18    QRH=QRH+EPSH*XA(3,1,J)
      Y=DY
      DO 19 I=2,ISTOP
      TCON1=TCON(T(I-1),TW,TS)
      TCON2=TCON(T(I),TW,TS)
      TCON3=TCON(T(I+1),TW,TS)
      PHPT=61.6/(HS*PS**.1635)*(TS/556.)**1.819*T(I)**.819
      DQCO(I)=1./(2.*PE*DY)*((TCON3+TCON2)*(T(I+1)-T(I))/DY-(TCON2+TCON1
     1)*(T(I)-T(I-1))/DY)
      DQCV(I)=-RHOV(Y,VW)*PHPT*(T(I+1)-T(I-1))/(2.*DY)
      DQS(I)=DQCO(I)+DQCV(I)+DQRL(I)+DQRR(I)+DQRH(I)+DQRE(I)
      DIVQP(I)=DQRL(I)+DQRR(I)+DQRH(I)+DQRE(I)
      IF (NITDQ.EQ.0.OR.NDQFIX.EQ.0) DIVQ(I)=DIVQP(I)
      DIFE=ABS(DIVQP(I)-DIVQ(I))
      IF (DIFE.GT.BIGDQE) IBDQE=I
      BIGDQE=AMAX1(BIGDQE,DIFE)
      A(I)=DT/(2.*DY)*((TCON2+TCON1)/(PE*DY)+RHOV(Y,VW)*PHPT)
      B(I)=-1.-DT/(2.*PE*DY**2)*(2.*TCON2+TCON3+TCON1)
      C(I)=DT/(2.*DY)*((TCON2+TCON3)/(PE*DY)-RHOV(Y,VW)*PHPT)
      D(I)=-DT*DIVQ(I)-T(I)
      QCONZ(I)=-CR/BU*TCON(T(I),TW,TS)*(T(I+1)-T(I-1))/(2.*DY)
      QZ(I)=QRPZ(I)+QRMZ(I)+QRRHZ(I)+QCONZ(I)
      IC=IC+1
      P(I)=T(I)
      IF (IC.NE.10) GO TO 19
      IC=0
      IL=I
19    Y=Y+DY
      D(2)=D(2)-A(2)*T(1)
      D(ISTOP)=D(ISTOP)-C(ISTOP)*T(IHLF)
      A(2)=B(2)
      B(2)=D(2)/A(2)
      DO 20 I=3,ISTOP
      IM1=I-1
```

```
      AS=A(I)
      A(I)=B(I)-A(I)*C(IM1)/A(IM1)
      B(I)=(D(I)-AS*B(IM1))/A(I)
20    CONTINUE
      T(IHLF)=TH/TS
      T(ISTOP)=B(ISTOP)
      K=IHLF-2
      DO 21 I=2,K
      J=IHLF-I
      T(J)=B(J)-C(J)*T(J+1)/A(J)
21    CONTINUE
      T(1)=1.
      DO 22 I=2,ISTOP
      FN(I)=(T(I)-P(I))/DT
      IF (ABS(FN(I)).GT.BIG) IBIG=I
      BIG=AMAX1(BIG,ABS(FN(I)))
22    CONTINUE
      SLOPE=(P(IHLF)-P(IHLF-1))/DY
      QCONZ(IHLF)=-CR/BU*SLOPE
      QZ(IHLF)=QRPZ(IHLF)+QRRHZ(IHLF)+QCONZ(IHLF)
      QA=QRH-EPSH/(2.*BU)*T(IHLF)**4-CR/BU*SLOPE
      IF (IP.NE.IIP) GO TO 28
      DO 23 I=1,IL,10
      WRITE (2,49) I,(P(I-1+K),K=1,10),DIVQ(I),QZ(I)
      WRITE (2,64) (XA(J,I,1),J=1,3),(XA(J,I,2),J=1,3)
23    PRINT 49, I,(P(I-1+K),K=1,10),DIVQ(I),XA(3,I,2)
      I=I+10
      PRINT 49, I,(P(IL+K),K=1,10),DIVQ(IL+1),XA(3,IL+1,1)
      PRINT 53, XA(1,1,1),XA(2,IHLF,1),XA(3,1,1),XA(1,1,2),XA(3,1,2),SLO
     1PE,DT,IHLF,DIVQ(IHLF),QRH
      WRITE (2,49) I,(P(IL+K),K=1,10),DIVQ(IL+1),QZ(IL+1)
      WRITE (2,53) XA(1,1,1),XA(2,IHLF,1),XA(3,1,1),XA(1,1,2),XA(3,1,2),
     1SLOPE,DT,IHLF,DIVQ(IHLF),QRH
      ILP=IL+1
      IF (IPQ.EQ.0) GO TO 25
      DO 24 I=1,ILP,10
      J=I-1
      KS=10
      IF (I.EQ.ILP) KS=IHLF-IL
      WRITE (2,58) I,(QRPZ(J+K),K=1,KS)
      WRITE (2,59) (QRMZ(J+K),K=1,KS)
      WRITE (2,59) (QRRHZ(J+K),K=1,KS)
      WRITE (2,59) (QCONZ(J+K),K=1,KS)
24    WRITE (2,60) (QZ(J+K),K=1,KS)
25    IF (IPDQ.EQ.0) GO TO 27
      DO 26 I=1,ILP,10
      J=I-1
      KS=10
      IF (I.EQ.ILP) KS=IHLF-IL
      WRITE (2,58) I,(DQCO(J+K),K=1,KS)
      WRITE (2,59) (DQCV(J+K),K=1,KS)
      WRITE (2,59) (DQRL(J+K),K=1,KS)
      WRITE (2,59) (DQRR(J+K),K=1,KS)
      WRITE (2,59) (DQRH(J+K),K=1,KS)
      WRITE (2,59) (DQRE(J+K),K=1,KS)
26    WRITE (2,60) (DQS(J+K),K=1,KS)
27    IF (IURIKA.EQ.1) GO TO 5
      IP=0
28    NIT=NIT+1
      NITDQ=1
      IP=IP+1
      AHOPP=QA/HEFFT*DSVS
      THE=.95
      THE=.98
      ID=IHLF-1
      IF (MFIX.NE.1) GO TO 29
```

```
      IF (BIG.GT.1.E-03) GO TO 37
      THE=0
      THE=.35
      THE=.5
      THE=.8
      THE=.98
      THE=.95
      THE=.9
      NITDQ=0
      ICHM=ICHM+1
      PRINT 63, ICHM
      WRITE (2,63) ICHM
   29 CONTINUE
      AMDP=THE*AMDU+(1.-THE)*AMDPP
      DELT=1.+(DELT-1.)*AMDP/AMDU
      VW=AMDP/DW
      IHLFP=DELT/DY+1
      IF (IHLFP.LT.2001) GO TO 30
      PRINT 55, IHLFP,DELT,NIT
      CALL EXIT
   30 IF (IHLFP-IHLF) 35,36,31
   31 IS=IHLFP-IHLF
      DO 32 K=1,IHLF
   32 FT(K)=T(K)
      DO 33 K=1,IS
   33 T(K)=1.
      KK=IS+1
      DO 34 K=KK,IHLFP
   34 T(K)=FT(K-IS)
      IHLF=IHLFP
      GO TO 36
   35 IHLF=IHLFP
      T(IHLF)=TW/TS
      T(IHLF-1)=T(IHLF)+(T(IHLF-3)-T(IHLF))*1./3.
      T(IHLF-2)=T(IHLF)+(T(IHLF-3)-T(IHLF))*2./3.
   36 CONTINUE
      HFIX=0
   37 IF (MOD(NIT,60).NE.0) GO TO 39
      ICON=0
      PUNCH 62
      PUNCH 61, ICON,IHLF,AMDU,HEFF,DELT,DIODSL,VI,RN,THICK
      DO 38 I=1,IHLF,10
   38 PUNCH 56, (T(I-1+K),K=1,10)
   39 IF (NIT-1500) 40,40,43
   40 PRINT 52, NIT,QA,AMDU,AMDPP,IHLF,QZ(IO),BIG,IBIG
      WRITE (2,52) NIT,QA,AMDU,AMDPP,IHLF,QZ(IO),BIG,IBIG
      COM2=-T(IHLF)**4/(2.*BU)
      COM3=-CR/BU*SLOPE
      PRINT 68, QRW,COM2,COM3
      WRITE (2,68) QRW,COM2,COM3
      CALL SSWTCH (1,ISIND)
      IF (ISIND.EQ.1) GO TO 41
      CALL TIMTGO (CLT1)
      CLT2=CLT1/60.
      IF (1.LT.CLT2) GO TO 42
   41 HR=0
      PUNCH 69, NIT
      PRINT 70
      WRITE (2,70)
      GO TO 44
   42 IF (QA.LT.0.) GO TO 47
      IF (HFIX.EQ.1) GO TO 6
      HFIX=HFI
      AMDC=AMDU
      AMDU=AMDP
      AMDER=ABS(AMDPP-AMDC)/AMDPP
```

```
      IF (AMDER.GT..0100) GO TO 4
      IF (BIG.GT.1.E-03) GO TO 4
      PRINT 51, AMDER
      WRITE (2,51) AMDER
      IF (IP.EQ.1) GO TO 43
      IP=IIP
      ICON=1
      IURIKA=1
      GO TO 6
43    IURIKA=1
      GO TO 5
44    IF (THICK.GT.3.00E7) MR=0
      PUNCH 62
      PUNCH 61, ICON,IHLF,AMDU,HEFF,DELT,DIODSL,VI,RN,THICK
      THICK=THICK+1.E3
      IP=20
      IP=10
      IP=150
      IP=100
      IP=50
      IIP=IP
      NIT=0
      MFI=0
      MFI=1
      MFIX=MFI
      ICHM=0
      IURIKA=0
      DO 45 I=1,IHLF,10
45    PUNCH 56, T(I),T(I+1),T(I+2),T(I+3),T(I+4),T(I+5),T(I+6),T(I+7),T(
     1I+8),T(I+9)
      IF (MR.EQ.0) GO TO 47
      IF (IREAD.EQ.1) GO TO 46
      IREAD=1
      IREAD=0
      GO TO 4
46    READ 61, ICON,IHLFR,AMDU,HEFF,DELT,DIODSL,VI,RN,THICK
      VH=AMDU/DH
      IREAD=0
      IREAD=1
      GO TO 2
47    CALL EXIT
C
48    FORMAT (2X,18HINITIAL CONDITIONS,//13X,6HTH(DR),10X,20HTCONH(BTU/F
     1T-SEC-DR),6X,4HRHOI,13X,7HVI(FPS),15X,4HRHOH,14X,8HDELS(FT),/2X,6E
     220.4//13X,7HALT(FT),14X,6HDI/DSL,14X,6HRN(FT),10X,13HHEFF(BTU/LBM)
     3,9X,10HVH(FT/SEC),11X,6HTS(DR),/2X,6E20.4//11X,3HDRS,18X,7HPS(ATM)
     4,11X,11HDH(LBM/FT3),9X,11HHS(BTU/LBM),9X,11HALPPS(1/FT),12X,4HDSVS
     5,/2X,6E20.4//14X,2HPE,17X,5HGAMMA,16X,2HBO,18X,2HBU,18X,2HCR,17X,4
     6HAKST,/2X,6E20.4//14X,2HDZ,18X,3HDT ,16X,11HDHVH2DDIVI2,10X,5HQNOR
     7M,15X,3HBUH,/2X,3E20.4)
49    FORMAT (2X,I4,2X,12E10.3/)
50    FORMAT (2X,46HFAILED TO CONVERGE AFTER 20 ITERATIONS IN EIPC)
51    FORMAT (2X,5HURIKA,12HMDOT ERROR =,E11.4,16HDIVQ MAX ERROR =,E11.4
     1//)
52    FORMAT (2X,5HNIT =,I4,1X,7HQWALL =,E11.4,1X,9HMDOTHU =,E11.4,1X,9H
     1MDOTHPP =,E11.4,1X,5HIHLF =,I4,1X,5HQZD =,E11.4,1X,5HBIG =,E11.4,1
     2X,6HIBIG =,I4/)
53    FORMAT (2X,7E11.4,11H =DT,IHLF =,I4,9H, DQZD = ,E11.4,1H,,E11.4/)
54    FORMAT (10F8.5)
55    FORMAT (2X,22HIHLF .GT. 2000, IHLF =,I4,8H  DELT =,E11.4,7H  NIT =
     1,I3)
56    FORMAT (10F8.5)
57    FORMAT (////2X,14HRESULTS FOR A ,I1,19H STEP MODEL, DELT =,E11.4,8
     1H MDOTU =,E11.4,7H EPSH =,E11.4,7H IHLF =,I4,8H THICK =,E11.4,8H I
     2HLFR =,I4////)
58    FORMAT (2X,I4,1X,10E11.4)
```

```
59    FORMAT (7X,10E11.4)
60    FORMAT (/7X,10E11.4//)
61    FORMAT (2I5,7E10.3)
62    FORMAT (55HC---FORMAT= ICON,IHLF,AMOU,HEFF,DELT,DIODSL,VI,RN,THICK
     1)
63    FORMAT (//2X,11HCHANGE MOOT,I6///)
64    FORMAT (8X,6E10.3/)
65    FORMAT (//,2X,23HSUMMATION THROUGH STEP ,I1,18H HEAT FLUXES OF A ,
     1I1,11H STEP MODEL,//)
66    FORMAT (//,2X,27HASSOCIATED FLUX DIVERGENCES,//)
67    FORMAT (1H )
68    FORMAT (2X,3E20.5)
69    FORMAT (1X,6HNIT = ,I5)
70    FORMAT (1X,13H TIME   LIMIT)
      END
      SUBROUTINE FCT1 (Y,X,DERX,N)
      DIMENSION X(1), DERX(1)
      COMMON /AA/ XA(3,2000,2),T(2000)
      COMMON /D/ THICK,JS,A,B,BU,TS
      DO 1 J=1,JS
      ALCK=ALP(J,Y,T(N),TS,THICK,JS)
1     DERX(J)=BU*ALCK*B
      RETURN
      END
      SUBROUTINE FCT2 (Y,X,DERX,N)
      DIMENSION X(1), DERX(1)
      COMMON /AA/ XA(3,2000,2),T(2000)
      COMMON /BB/ IHLF,AN(10)
      COMMON /D/ THICK,JS,A,B,BU,TS
      L=IHLF+1-N
      INF=0
      DO 1 J=1,JS
      IF (J.EQ.JS) INF=1
      ALCK=ALP(J,Y,T(L),TS,THICK,JS)
      DERX(J)=-ALCK*BU
1     DERX(JS+J)=-PLKI(T(L),TS,AN(J),AN(J+1),INF,0)*ALCK*E(2,X(J))
      RETURN
      END
      SUBROUTINE OUTP1 (Y,X,DERX,N,NDIM,PRMT,M,IHLF)
      DIMENSION X(1), DERX(1), PRMT(1)
      COMMON /AA/ XA(3,2000,2),T(2000)
      COMMON /D/ THICK,JS,A,B,BU,TS
      DO 1 J=1,JS
1     XA(2,N,J)=X(J)
      RETURN
      END
      SUBROUTINE OUTP2 (Y,X,DERX,N,NDIM,PRMT,M,IHLF)
      DIMENSION X(1), DERX(1), PRMT(1)
      COMMON /AA/ XA(3,2000,2),T(2000)
      COMMON /D/ THICK,JS,A,B,BU,TS
      L=IHLF+1-N
      DO 1 J=1,JS
      XA(1,L,J)=X(J)
1     XA(3,L,J)=X(J+JS)
      RETURN
      END
      SUBROUTINE EIPC (PRMT,X,DERX,NDIM,IHLF,FCT,OUTP,NA)
      DIMENSION PRMT(1), X(1), DERX(1), XP(11), XC(11), DERXP(11), DX(11
     1)
1     PRMT(5)=0.
      N=NA
      Y=PRMT(1)
2     M=0
      CALL FCT (Y,X,DERX,N)
      IF (N-1) 4,3,4
3     CALL OUTP (Y,X,DERX,N,NDIM,PRMT,M,IHLF)
```

```
4     N=N+1
      DO 5 I=1,NDIM
5     XP(I)=X(I)+PRMT(3)*DERX(I)
      Y=Y+PRMT(3)
6     CALL FCT (Y,XP,DERXP,N)
      DO 7 I=1,NDIM
7     XC(I)=X(I)+PRMT(3)/2.*(DERXP(I)+DERX(I))
      DO 8 I=1,NDIM
      DX(I)=ABS(XC(I)-XP(I))
      IF (DX(I)-PRMT(4)) 8,8,9
8     CONTINUE
      GO TO 13
9     IF (M-20) 11,11,10
10    PRMT(5)=1.
      N=IHLF
      GO TO 13
11    DO 12 I=1,NDIM
12    XP(I)=XC(I)
      M=M+1
      GO TO 6
13    CALL OUTP (Y,XC,DERXP,N.NDIM,PRMT,M,IHLF)
      IF (PRMT(5)) 16,14,16
14    DO 15 I=1,NDIM
15    X(I)=XC(I)
      IF (N-IHLF) 2,16,16
16    RETURN
      END
      FUNCTION E (N,X)
C
C     FUNCTION TO GIVE THE N-TH EXPONENTIAL INTEGRAL OF X, EN(X).
C
C     BASED ON ALGORITHMS GIVEN IN SECTIONS 5.1.14, 5.1.53, AND 5.1.56
C     IN *HANDBOOK OF MATHEMATICAL FUNCTIONS WITH FORMULAS, GRAPHS, AND
C     MATHEMATICAL TABLES*, U.S. DEPT. OF COMMERCE, NATIONAL BUREAU OF
C     STANDARDS, APPLIED MATHEMATICS SERIES NO. 55.  (1964).
C     ROUTINE BY HARRY H. MURPHY, JR., 26 DECEMBER 1968.
C             *****   AMERICAN STANDARD FORTRAN   *****
C
      REAL A0,A1,A2,A3,A4,A5,B0,B1,B2,B3,C0,C1,C2,C3
C
      DATA A0,A1,A2,A3,A4,A5/-0.57721566,0.99999193,-0.24991055,0.055199
     168,-0.00976004,0.00107857/
      DATA B0,B1,B2,B3/0.2677737343,8.6347608925,18.0590169730,8.5733287
     1401/
      DATA C0,C1,C2,C3/3.9584969228,21.0996530827,25.6329561486,9.573322
     13454/
C
C
1     M=N
      Z=X
      IF (Z) 2,3,5
2     Z=0.
      PRINT 16
C
3     IF (M-1) 15,15,4
4     E=1.0/FLOAT(M-1)
      RETURN
C
5     IF (M) 15,6,7
C
6     E=EXP(-Z)/Z
      RETURN
C
7     IF (Z-1.0) 8,9,10
C
8     E1=((((A5*Z+A4)*Z+A3)*Z+A2)*Z+A1)*Z+A0-ALOG(Z)
```

```
      GO TO 11
C
9     E1=0.219383934
      GO TO 11
C
10    E1=((((((Z+B3)*Z+B2)*Z+B1)*Z+B0)*EXP(-Z))/(((((Z+C3)*Z+C2)*Z+C1)*Z+
     1C0)*Z)
11    IF (M-1) 15,14,12
C
12    L=M-1
      EX=EXP(-Z)
      DO 13 I=1,L
13    E1=(EX-Z*E1)/FLOAT(I)
14    E=E1
      RETURN
C
15    E=1.7E38
      PAUSE 55555
      RETURN
C
16    FORMAT (2X,44HARGUMENT OF EXPOINT WAS NEGATIVE,SET TO ZERO)
      END
      FUNCTION PLKI (TT,TN,AN1,AN2,INF,NO)
      T=TT*TN/1.8
      HOK=6.62517/1.3804*1.E-11
      A=HOK*AN1/T
      B=HOK*AN2/T
      IF (INF.EQ.1) B=100.
      IF (B-A) 2,1,3
1     PLKI=0.
      RETURN
2     PRINT 4, A,B
      CALL EXIT
3     PLKI=TT**4*PLNKUT(A,B)
      RETURN
C
4     FORMAT (2X,/////,44H   RANGE OF PLANCK INTEGRATION INVERTED, A =,E
     111.4,5H  B =,E11.4)
      END
      FUNCTION PLNKUT (BETA1,BETA2)
C     ASSUME BETA2 MORE THAN BETA1
      DIMENSION TBL(120)
      DATA (TBL(I),I=1,120)/.7190,.7568,.7989,.8459,.8988,.9587,1.0271,1
     1.1062,1.1983,1.3073,1.4380,1.4673,1.4979,1.5298,1.5630,1.5978,1.63
     241,1.6721,1.7119,1.7537,1.7975,1.8436,1.8921,1.9432,1.9972,2.0543,
     32.1147,2.1788,2.2459,2.3194,2.3967,2.4793,2.5679,2.663,2.7654,2.87
     46,2.9958,3.1261,3.2582,3.4238,3.595,3.7842,3.9944,4.2294,4.4938,4.
     57933,5.1357,5.5353,5.9917,6.5364,7.19,7.3744,7.5684,7.773,7.9889,8
     6.2171,8.4588,8.7152,8.9875,9.2774,.9856,.9834,.9808,.9777,.9738,.9
     7690,.9629,.9551,.9451,.9319,.9143,.91,.9055,.9007,.8956,.8901,.884
     83,.878,.8713,.8641,.8564,.8481,.8392,.8297,.8194,.8083,.7963,.7834
     9,.7694,.7544,.7381,.7204,.7013,.6807,.6583,.6341,.6079,.5796,.5492
     $,.5164,.4813,.4433,.4040,.3621,.3185,.2736,.2282,.1834,.1405,.1011
     $,.0669,.05935,.05225,.04561,.03946,.03379,.02852,.02396,.01979,.01
     $51/
      I=0
      IF (BETA2-.719) 1,2,2
1     PLNKUT=.051329911*(BETA2**3*(1.-BETA2*(.375-BETA2*.05))-BETA1**3*(
     11.-BETA1*(.375-BETA1*.05)))
      RETURN
2     J=1
      BETA=BETA1
      IF (BETA-.719) 3,4,4
3     FCN=1.-.051329911*BETA**3*(1.-BETA*(.375-BETA*.05))
      I=1
      GO TO 9
```

```
4       I=I+1
        IF (I-60) 5,7,7
5       IF (BETA-TBL(I+1)) 5,6,4
6       FCN=TBL(I+60)+(BETA-TBL(I))*(TBL(I+61)-TBL(I+60))/(TBL(I+1)-TBL(I)
       1)
        GO TO 8
7       FCN=.153989733*EXP(-BETA)*(((BETA+3.)*BETA+6.)*BETA+6.)
8       GO TO (9,10), J
9       J=2
        OFCN=FCN
        BETA=BETA2
        I=I-1
        GO TO 4
10      PLNKUT=OFCN-FCN
        RETURN
        END
        FUNCTION TCON (TRT,TW,TS)
        COMMON /A/ C(6,6)
        COMMON /E/ NCOEF
        TR=TRT*TS/TW
        IF (NCOEF) 10,1,10
1       C(1,1)=8.4397
        C(1,2)=-1.9538E+01
        C(1,3)=3.9888E+01
        C(1,4)=-2.3504E+01
        C(1,5)=4.6892
        C(1,6)=0.
        C(2,1)=-1405.1
        C(2,2)=847.6
        C(2,3)=-120.4
        C(2,4)=0.
        C(2,5)=0.
        C(2,6)=0.
        C(3,1)=3.0839E+03
        C(3,2)=-1.6188E+03
        C(3,3)=2.6456E+02
        C(3,4)=-1.2268E+01
        C(3,5)=0.
        C(3,6)=0.
        C(4,1)=-1.7442E+04
        C(4,2)=6.4677E+03
        C(4,3)=-7.4937E+02
        C(4,4)=2.7093E+01
        C(4,5)=0.
        C(4,6)=0.
        C(5,1)=-3.56115435E+05
        C(5,2)=1.90637326E+06
        C(5,3)=-4.06277635E+05
        C(5,4)=4.30950763E+04
        C(5,5)=-2.275706E+03
        C(5,6)=4.7875E+01
        C(6,1)=-1.88930669E+06
        C(6,2)=7.20870759E+05
        C(6,3)=-1.0946071E+05
        C(6,4)=8.2603113E+03
        C(6,5)=-3.092268E+02
        C(6,6)=4.59125
        TWC=TW/1.8*1.E-03
        IF (TWC-3.0) 2,3,3
2       I=1
        GO TO 6
3       IF (TWC-4.0) 4,4,5
4       I=2
        GO TO 6
5       I=3
6       TCW=C(I,1)
```

```
      DO 7 J=2,6
7     TCH=TCH+C(I,J)*THC**(J-1)
      DO 8 I=1,6
8     C(I,1)=C(I,1)/TCH
      DO 9 I=1,6
      DO 9 J=2,6
9     C(I,J)=C(I,J)/TCH*THC**(J-1)
      TCON=TCH*1.E-06
      RETURN
10    TC=TR*TH/1.8*1.E-03
      IF (TC-3.0) 11,12,12
11    I=1
      GO TO 21
12    IF (TC-4.0) 13,13,14
13    I=2
      GO TO 21
14    IF (TC-6.0) 15,15,16
15    I=3
      GO TO 21
16    IF (TC-8.0) 17,18,18
17    I=4
      GO TO 21
18    IF (TC-11.0) 19,19,20
19    I=5
      GO TO 21
20    I=6
21    TCON=C(I,1)
      DO 22 J=2,6
22    TCON=TCON+C(I,J)*TR**(J-1)
      RETURN
      END
      FUNCTION RHOV (Y,VH)
      COMMON /B/ DI,VI,DH,RN,DRS,DELS,DELT,DY,TH,ALPPS,PS
      IF (1.-Y) 2,1,1
1     RHOV=(1.-2.*DELS/(DRS*RN)*Y+(1.-2.*DRS*(1.-DRS))*(DELS/(DRS*RN))**
     12*Y**2)
      RETURN
2     RHOV=DH*VH*((DELS/RN)**2.*(2.*DI*VI**2./(DH*VH**2.))*(DELT-Y)**2-1
     1.)/(DI*VI)
      RETURN
      END
      FUNCTION H (TH)
      DIMENSION C(15)
      C(1)=1.7668
      C(2)=14.5347
      C(3)=-43.4477
      C(4)=64.2735
      C(5)=-53.7980
      C(6)=27.7881
      C(7)=-9.3667
      C(8)=2.1397
      C(9)=-.3390
      C(10)=3.7648E-02
      C(11)=-2.9192E-03
      C(12)=1.548E-04
      C(13)=-5.3504E-06
      C(14)=1.0861E-07
      C(15)=-9.8213E-10
      TP=TH*1.E-03/1.8
      H=C(1)
      DO 1 I=2,15
1     H=H+C(I)*TP**(I-1)
      H=H*1716.6/(778.3*32.2)*TH
      RETURN
      END
      FUNCTION DHDTH (TR,TH,N)
```

```
      DIMENSION C(5,10)
      COMMON /E/ NCOEF
      IF (NCOEF) 2,1,2
1     C(1,1)=-28.11892
      C(1,2)=156.74822
      C(1,3)=-297.41723
      C(1,4)=287.6318
      C(1,5)=-154.29046
      C(1,6)=46.1647448
      C(1,7)=-7.1548861
      C(1,8)=.44522855
      C(1,9)=0.
      C(1,10)=0.
      C(2,1)=-1.06855572E+04
      C(2,2)=1.29895502E+04
      C(2,3)=-6.48881749E+03
      C(2,4)=1.71129321E+03
      C(2,5)=-2.51930012E+02
      C(2,6)=1.96635060E+01
      C(2,7)=-6.35908828E-01
      C(2,8)=0.
      C(2,9)=0.
      C(2,10)=0.
      C(3,1)=-2.96990088E+05
      C(3,2)=4.90068931E+05
      C(3,3)=-3.48664656E+05
      C(3,4)=1.41601365E+05
      C(3,5)=-3.58242712E+04
      C(3,6)=5.94232323E+03
      C(3,7)=-6.44503726E+02
      C(3,8)=4.41297964E+01
      C(3,9)=-1.73282597
      C(3,10)=2.97603206E-02
      C(4,1)=-7.96320668E+05
      C(4,2)=6.60834667E+05
      C(4,3)=-2.41649615E+05
      C(4,4)=5.11433986E+04
      C(4,5)=-6.90785786E+03
      C(4,6)=6.17778116E+02
      C(4,7)=-3.65941987E+01
      C(4,8)=1.38490007
      C(4,9)=-3.03921621E-02
      C(4,10)=2.94732708E-04
      C(5,1)=4.97863043E+06
      C(5,2)=-3.68612390E+06
      C(5,3)=1.20838419E+06
      C(5,4)=-2.30188836E+05
      C(5,5)=2.80786880E+04
      C(5,6)=-2.27430566E+03
      C(5,7)=1.22312740E+02
      C(5,8)=-4.21135032
      C(5,9)=8.42306435E-02
      C(5,10)=-7.45573464E-04
      SIG=4.761111E-13
      RETURN
2     TC=TR*TW/1.8*1.E-03
      IF (TC-4.0) 3,4,4
3     I=1
      GO TO 11
4     IF (TC-6.0) 5,5,6
5     I=2
      GO TO 11
6     IF (TC-8.0) 7,8,8
7     I=3
      GO TO 11
8     IF (TC-14.0) 9,10,10
```

```
9     I=4
      GO TO 11
10    I=5
11    IF (N-2) 12,14,14
12    DHDTH=C(I,1)
      DO 13 J=2,10
13    DHDTH=DHDTH+C(I,J)*TC**(J-1)
      DHDTH=DHDTH*1716.6/(778.3*32.2)/(SIG*TH**3.)
      RETURN
14    DHDTH=C(I,2)
      DO 15 J=3,10
15    DHDTH=DHDTH+(J-1)*C(I,J)*TC**(J-2)
      DHDTH=DHDTH*1716.6/(778.3*32.2)/(SIG*TH**2.*1.8)*1.E-03
      RETURN
      END
      FUNCTION ALP (I,Y,TR,TS,THICK,JS)
      DIMENSION C(2,10)
      COMMON /E/ NCOEF
      COMMON /B/ DI,VI,DH,RN,DRS,DELS,DELT,DY,TH,ALPPS,PS
      IF (NCOEF) 2,1,2
1     C(1,1)=-1.23143767E-01
      C(1,2)=9.92492977E-02
      C(1,3)=-3.56454105E-02
      C(1,4)=7.09652566E-03
      C(1,5)=-9.03755825E-04
      C(1,6)=7.46770314E-05
      C(1,7)=-3.98674796E-06
      C(1,8)=1.32320443E-07
      C(1,9)=-2.47722025E-09
      C(1,10)=1.99563377E-11
      C(2,1)=-1.06416989E+01
      C(2,2)=1.01965241E+01
      C(2,3)=-3.84165721
      C(2,4)=7.61949747E-01
      C(2,5)=-8.92455078E-02
      C(2,6)=6.54561710E-03
      C(2,7)=-3.06460092E-04
      C(2,8)=8.96055346E-06
      C(2,9)=-1.49939579E-07
      C(2,10)=1.10057950E-09
      NCOEF=1
      RETURN
2     T=TR*TS/1.8
      IF (JS-1) 3,3,6
3     IF (Y-1.) 4,5,5
4     ALP=1.191334E-09*(T/308.8)**(4.631-.1896*ALOG(PS))*PS**(1.9685-.17
     14*ALOG(PS))/ALPPS
      RETURN
5     ALP=1.191334E-09*(T/308.8)**(4.631-.1896*ALOG(PS))*PS**(1.9685-.17
     14*ALOG(PS))/ALPPS*THICK
      RETURN
6     T=T*1.E-03
      TH=1.
C     SET UP FOR SECOND BAND ENHANCEMENT ONLY
      IF (Y.GE.1..AND.I.EQ.2) TH=THICK
      IF (T-6.) 7,10,10
7     IF (I-1) 8,8,9
8     ALP=6.53E-05/3.538E-05*1.191E-09*(T*1.E3/308.8)**(4.631-.1896*ALOG
     1(PS))*PS**(1.9685-.174*ALOG(PS))/ALPPS*TH
      RETURN
9     ALP=2.43E-02*2.88E-02**((6.-T)/3.)*30.48/ALPPS*TH
      RETURN
10    ALP=C(I,1)
      DO 11 J=2,10
11    ALP=ALP+C(I,J)*T**(J-1)
      ALP=ALP*30.48/ALPPS*TH
```

```
      RETURN                                                              N  52
      END                                                                 N  53-

  09/07/72  SCOPE 3.2.0 - SCH  VER C73  6   05SEP72ECPA= 0754
 00.55.50.DIS.
 00.55.59.REQUEST,A.
 00.55.59. (07 ASSIGNED)
 00.56.05.COPYSBF(A)
 00.57.33.REWIND(X)
 00.57.33.CP   000.171 SEC.
 00.57.33.PP  164.290 SEC.
```